SCATTERING OF ELASTIC WAVES BY NEAR-SURFACE INHOMOGENEITIES

by

YUN FEN CHIN

A thesis
presented to the University of Manitoba
in partial fulfillment of the
requirements for the degree of
MASTER OF SCIENCE
in
CIVIL ENGINEERING DEPARTMENT

Winnipeg, Manitoba

SCATTERING OF ELASTIC WAVES BY NEAR-SURFACE INHOMOGENEITIES

BY

YUN FEN CHIN

A thesis submitted to the Faculty of Graduate Studies of
the University of Manitoba in partial fulfillment of the requirements
of the degree of

MASTER OF SCIENCE

I hereby declare that I am the sole author of this thesis.

I authorize the University of Manitoba to lend this thesis to other institutions or individuals for the purpose of scholarly research.

YUN FEN CHIN

I further authorize the University of Manitoba to reproduce this thesis by photocopying or by other means, in total or in part, at the request of other institutions or individuals for the purpose of scholarly research.

YUN FEN CHIN

ABSTRACT

Scattering of elastic waves by near-surface in homogeneities is investigated.Two independent sets of problems are considered.The first set consists of a pipeline embedded in a rectangular trench of backfill or,alternatively,two pipelines embedded in a single trench. The second set consists of three surface breaking cracks : a vertical crack,a 45 inclined crack and a branched (Y) crack.The examples considered are problems involving plane strain in semi-infinite medium. A hybrid numerical technique that combines the finite element method with eigenfunction expansions is used to obtain the results.All the problems are independently subjected to in-plane pressure(P),shear(SV) and Rayleigh waves.In the first set of problems,dynamic radial displacements and hoop stresses on the outer circumferences of the pipes are presented.In the second set of problems,stress intensity factors at the crack tips and scattered surface displacements are presented.The dynamic responses of the pipeline(s) and the surface breaking cracks are significantly dependent on the frequency,the angle of incidence and the nature of the incident waves.

ACKNOWLEDGEMENTS

The wishes to express his most sincere thanks to his advisor, Professor A.H. Shah,for his guidance and assistance in the preparation of this thesis.My sincere thanks also to Professor R.K.N.D. Rajapakse for his invaluable advise and guidance.Without them,this thesis never would have been possible.

Special thanks to Professor N. Popplewell and Mr. P. Trainor for their careful reviewing of the thesis and their invaluable suggestions.Assistance by Dr. K.C. Wong is greatly appreciated.

The author wishes to thank his fiancee',Sue,his sister,Ellen, and his parents for their encouragement,understanding and moral support.

Lastly,the author also wishes to thank Mrs. Wendy Severson for her excellent typing and his friends who have been of direct or indirect assistance in preparing this thesis.

TABLE OF CONTENTS

PAGE

LIST OF TABLES

LIST OF FIGURES

PAGE

PAGE

CHAPTER 1. INTRODUCTION

1.1 Engineering Applications of Wave Phenomena

The phenomenon of scattering and diffraction of elastic waves has found many practical applications in the fields of Earthquake Engineering, non-destructive testing, fracture mechanics, seismic exploration, Civil Engineering, Acoustics, and Electromagnetics. In order to stress the importance of the subject, a few of the above will be discussed briefly. However, it should be noted that there are many other applications of elastic wave phenomena.

In Earthquake Engineering, the scattering of seismic waves by any inhomogeneities or discontinuities under or on the ground surface causes local amplifications of the ground motion. Typical inhomogeneities are underground pipelines and tunnels, structures resting on or embedded in the ground, soil layering and irregular topography of the ground surface. The task is to find the resulting stress or displacement field at points of interest.

In the field of non-destructive testing, ultrasonics pulses are used to locate defects in a solid by measuring the reflection of pulse energy. The location, size, shape, and orientation of the defects or obstacles can be determined from the scattered fields. Thus, there is considerable interest in the scattering caused by the cracks, with a view towards obtaining the crack geometry from the scattered field. It is also possible to determine many fundamental properties of materials such as elastic constants and damping characteristics by studying the propagation, reflection and attenuation of ultrasonic pulses.

In fracture mechanics, the quantities of interest are the stress intensity factors, since they are a measure of the stress environment around a

crack tip. The crack will propagate when the stress intensity factors reach the critical values. Also, under dynamic loading, it is important to know the elastodynamic response of the crack because a local stress concentration could result at the crack tip.

In Civil Engineering, wave scattering studies are required to determine the effects of blast loading on buried structures and shocks caused by pile driving. Also, scattering of elastic waves has many engineering application in Acoustics and Electromagnetics.

All of the problems mentioned above have the same basic nature. When incident elastic waves interact with inhomogeneities or discontinuities such as cavities (e.g., tunnels and pipes), slits (e.g., cracks) and inclusions (e.g., flaws in materials) in a medium, scattering of elastic waves occur as a consequence of reflection phenomena.

The principal objective of this thesis is to study the scattering of elastic waves by near surface inhomogeneities. Two sets of problems are considered. The first set consists of a buried pipeline surrounded by a rectangular trench of backfill and, also, two pipelines lying parallel to each other in a similar backfilled trench (See Fig. 4.1 and Fig. 4.2). These problems are of interest in lifeline earthquake engineering. The second set is of interest in non-destructive testing and fracture mechanics, and consists of three surface breaking cracks: a vertical crack, a 45° inclined crack, and a Y crack (See Fig. 5.1 and Fig. 5.2). Both sets of problems are subjected to in-plane harmonic P, SV and Rayleigh waves. These waves will be discussed in the next section.

1.2 Wave Types

Three basic types of waves -- body waves, surface waves, and interface waves -- can propagate depending on the medium considered. Reference [1]

gives an extensive review of these three types of waves and their behaviours. A brief review will be given in the following paragraphs.

In an infinite medium or full space, only body waves can propagate. There are two types of body waves: dilatational or pressure (P) waves, and equivoluminal or shear (SV, SH) waves, each being characterized by a specific speed. Furthermore, these wave types can exist independently or uncoupled from each other. For a medium having λ and μ as Lame's constants and ρ as the mass density, the P wave propagates with speed $C_1 = [(\lambda + 2\mu)/\rho]^{\frac{1}{2}}$ and the direction of the particle motion is in the direction of the wave motion. The SV and SH waves propagate with shear speed $C_2 = (\mu/\rho)^{\frac{1}{2}}$ and the direction of the particle motion is perpendicular to the wave motion. Furthermore, SV and SH waves are independent of each other. When the in-plane problem is considered, only P and SV waves can exist. On the other hand, when the anti-plane problem is considered, only SH waves can exist.

In a semi-infinite medium or half-space, both body waves and surface waves can propagate. If the surface boundary is free, a pure reflection process will occur when incident waves encounter the boundary. Then the phenomenon known as mode conversion occurs; that is, an incident wave of one type, either pressure or shear, is converted into a combination of pressure and shear waves on reflection. Surface waves known as Rayleigh waves propagate with a speed which is less than the shear speed. Also, the speed is independent of frequency, and this indicates that a surface pulse propagates non-dispersively. The particle motion is elliptical in nature and retrograde with respect to the direction of wave motion. Also, the amplitude of the motion decreases exponentially with depth.

In a layered medium, body waves and interface waves can propagate. Mode conversion also occurs in a layered medium. In fact, the semi-infinite

medium is a layered medium with one medium usually taken as air. Unlike the semi-infinite medium, incident body waves are not only reflected but are also refracted at the boundary of the two media. The existence of interface waves known as Stonely waves [1] requires that the shear wave velocities of the two media have to be nearly the same. The Stonely wave is a generalized Rayleigh wave. The antiplane surface or interface wave in layered medium is also called a Love wave [1].

Since an in-plane (plane strain) problem in a semi-infinite medium is considered in this thesis, a combination of P, SV, and Rayleigh waves can exist.

1.3 Previous Work

In the last twenty years, the scattering of incident plane harmonic waves by inhomogeneities has received considerable attention by many researchers. However, much of the early work was concentrated on one- and two-dimensional scattering in an infinite medium, and one-dimensional scattering in a semi-infinite medium. A review of the later studies can be found in reference [2]. Only during recent years have two-dimensional in-plane scattering problems in a semi-infinite medium been studied. A thorough review of this recent work and the work on two-dimensional scattering in an infinite medium have been listed in reference [3]. Nevertheless, the recent work most relevant to this thesis is reviewed in the following paragraphs.

The dynamic response of buried pipelines and tunnels excited by elastic waves in an elastic medium is a subject of considerable interest in lifeline earthquake engineering. In reference [3], it was stated that many researchers have ignored the interaction between the pipeline and its surrounding ground, by simply modelling the pipeline as a beam on an elastic foundation. Others have modelled the pipe as a cylindrical shell, but have not taken into account the interaction of the shell with the surrounding ground. On the

other hand, Shah, Datta and Wong [4-7] have accounted for such an interaction in their extensive studies of the dynamic behaviour of buried pipelines and tunnels. For instance, in article [5], the pipeline is assumed to be surrounded locally by a coaxial annular region of homogeneous material which is different from the material of the homogeneous medium. This assumption was a first attempt to model the actual situation in which the embedded pipeline is usually surrounded by a trench of backfill. However, in this thesis, the actual geometry of the trench is modelled (see Fig. 4.1). In addition, two pipelines lying parallel to each other in a similar backfilled trench are considered.

The scattering of elastic waves by cracks has received considerable attention by many researchers. Such studies are important in the field of quantitative non-destructive evaluation and in the field of fracture mechanics where the stress intensity factors at the crack tips are of interest. References [8,9] reviewed previous methods of studying the scattering of antiplane and in-plane waves by sub-surface cracks. In this thesis, attention is focused on the scattering of elastic waves by surface breaking cracks. Achenbach et al. [10] and Mendelsohn et al. [11] have used an integral equation approach to study scattering by surface-breaking plane cracks. Alternatively, Hirao et al. [12] have used the finite-difference method to study the scattering of Rayleigh waves by surface-breaking cracks. Also, in a recent article [13], Visscher uses a boundary integral equation formulation to evaluate scattering by surface-breaking or subsurface planar cracks. The scattering of SH waves by surface breaking planar cracks was studied by Stone et al. [14], using an integral equation formulation, and by Datta [15], using a matched asymptotic expansion technique. Nevertheless, all the above studies of scattering by surface-breaking cracks are limited

either to a vertical straight crack or to scattering by SH waves.

Previous studies of the scattering of elastic waves by inhomogeneities have generally considered simplistic geometries and/or an isotropic, elastic and homogeneous medium surrounding the inhomogeneities. Also, the formulations could solve only one particular problem. Two methods, the separation of variables and the numerical solution of an integral equation, are extensively employed in the literature as reviewed in reference [16]. Both of these methods have the above limitations. On the other hand, numerical methods like the finite difference and the finite element technique cannot be used to discretize the entire semi-infinite domain. Artificial absorbing boundary conditions have to be imposed in the far field region. However, the discretized region is still large, and the techniques are too expensive computationally.

Recently, Shah, Datta, and Wong [3-9, 17, 18] have proposed a hybrid technique which uses a finite element representation in the near field and an eigenfunction expansion representation in the far field (acronym FEEET). The FEEET has the advantage that it can be used for any arbitrarily-shaped scatterer as well as for multiple scatterers. Also, the FEEET is more computationally efficient than the finite element method alone. At first, the FEEET was used to study the scattering of in-plane P, SV waves by arbitrarily-shaped inhomogeneities in an infinite medium [17]. Later, the technique was further employed to study the scattering of in-plane P, SV, and Rayleigh waves by arbitrarily-shaped inhomogeneities in a semi-infinite medium [3-9, 18]. However, in the above studies, the restriction that the inhomogeneities have to be embedded deep in the medium was imposed. In this thesis, the FEEET is generalized so that the restriction can be relaxed and inhomogeneities can be embedded near the surface of the half-space. Examples

of such inhomogeneities are pipeline(s) surrounded by a trench of backfill material and surface breaking cracks.

In the FEEET, inhomogeneities are enclosed by a contour or boundary B as shown in Fig. 2.1. The region inside B is represented by finite elements and the solution outside B is expressed in terms of eigenfunction expansions. The regions outside and inside of B are designated Region I and Region II, respectively. By using the eigenfunction expansion and imposing the continuity conditions for displacements and forces at a finite number of points on B, an impedance matrix is formed for exterior Region I. Combining this with the finite element impedance matrix of interior Region II, the unknown coefficients of the eigenfunction expansion can be determined. Knowing these coefficients, the displacement and stress fields can be determined anywhere in the semi-infinite plane or half-space.

In order to generalize the FEEET, the potentials used in the eigenfunction expansion are expressed in a general integral form instead of the expanded integral form used previously. In Chapter 2, these general expressions are given and the problem formulation is discussed. In Chapter 3, the numerical scheme of the integrals is discussed. Chapter 4 presents numerical results for the pipelines and Chapter 5 presents numerical results for the surface breaking planar and non-planar cracks.

CHAPTER 2. PROBLEM FORMULATION

2.1 Plane Strain Motion in Semi-Infinite Medium

Consider a homogeneous, isotropic, and linearly elastic medium which occupies the half plane $y \geq 0$ as shown in Fig. 2.1. Assume the displacement $u(x,y,t)$ at a point P to be a time-varying harmonic of the form $u(x,y)e^{-i\omega t}$, where ω is the circular frequency and i is $\sqrt{-1}$. The displacement equation of motion in vector notation can be written as

$$\mu\nabla^2\underset{\sim}{u} + (\lambda + \mu)\nabla\nabla.\underset{\sim}{u} = -\rho\omega^2\underset{\sim}{u} \tag{2.1}$$

Here, λ and μ are the Lame's constants and ρ is the mass density of the medium. Note that the time harmonic factor $e^{-i\omega t}$ which is common to the displacement and stress fields will be omitted in the sequel.

It can be shown that Eq. (2.1) is satisfied by a displacement vector field of the form

$$\underset{\sim}{u}(x,y) = \nabla\phi + \nabla\times\chi, \tag{2.2}$$

provided that the potentials, ϕ and χ are solutions to the wave equations

$$\nabla^2\phi + k_1{}^2\phi = 0$$

$$\nabla^2\chi + k_2{}^2\chi = 0 \tag{2.3}$$

where $k_1 = \omega/c_1$ and $k_2 = \omega/c_2$ are the pressure and shear wave numbers respectively and $c_1 = \sqrt{\rho/(\lambda+2\mu)}$ and $c_2 = \sqrt{\rho/\mu}$ are the pressure and shear wave speeds, respectively.

From Eq. (2.2), the horizontal and vertical displacements are

$$u_x = \frac{\partial\phi}{\partial x} + \frac{\partial\chi}{\partial y}$$

$$u_y = \frac{\partial\phi}{\partial y} - \frac{\partial\chi}{\partial x} \quad . \tag{2.4}$$

Also, from the strain-displacement and the stress-strain relationships, the three components of stress field can be written as:

$$\sigma_{xx} = (\lambda + 2\mu)\frac{\partial u_x}{\partial x} + \frac{\partial u_y}{\partial y}$$

$$\sigma_{yy} = (\lambda + 2\mu)\frac{\partial u_y}{\partial y} + \lambda\frac{\partial u_x}{\partial x}$$

$$\sigma_{xy} = \mu\left(\frac{\partial u_x}{\partial y} + \frac{\partial u_y}{\partial x}\right) . \qquad (2.5)$$

2.1.1 Scattered Field

The potentials ϕ and χ according to Gregory [19] can be expanded in the form

$$\phi = \sum_{n=-\infty}^{\infty} (a_n \phi_n^p + b_n \phi_n^s)$$

$$\chi = \sum_{n=-\infty}^{\infty} (a_n \chi_n^p + b_n \chi_n^s) \qquad (2.6)$$

where the expressions ϕ_n^p, ϕ_n^s, χ_n^p and χ_n^s are derived in Appendix A, and the coefficients a_n and b_n are unknown. The potentials ϕ and χ satisfy the free surface conditions, $\sigma_{xy} = \sigma_{yy} = 0$, and consist of outgoing waves at infinity. Note that ϕ and χ are valid for $y \geq 0$ and $r \leq a$ $(o < a < h)$ as shown in Fig. 2.2.

By substituting Eqs. (2.6) into Eqs. (2.4) and Eqs. (2.5), the displacement and stress components of plane strain scattered field can be determined and written as

$$u_x^{(s)} = \sum_{n=-\infty}^{\infty} [a_n(\phi_{n,x}^p + \chi_{n,y}^p) + b_n(\phi_{n,x}^s + \chi_{n,y}^s)]$$

$$u_y^{(s)} = \sum_{n=-\infty}^{\infty} [a_n(\phi_{n,y}^p - \chi_{n,y}^p) + b_n(\phi_{n,y}^s - \chi_{n,x}^s)] \qquad (2.7a)$$

$$\sigma_{xx}^{(s)} = (\lambda + 2\mu) \sum_{n=-\infty}^{\infty} \{a_n(\phi_{n,xx}^p + \chi_{n,yx}^p) + b_n(\phi_{n,xx}^s + \chi_{n,yx}^s)\}$$

$$+ \sum_{n=-\infty}^{\infty} \{a_n(\phi_{n,yy}^p - \chi_{n,xy}^p) + b_n(\phi_{n,yy}^s - \chi_{n,xy}^s)\}$$

$$\sigma_{yy}^{(s)} = (\lambda + 2\mu) \sum_{n=-\infty}^{\infty} \{a_n(\phi_{n,yy}^{p} - \chi_{n,xy}^{p}) + b_n(\phi_{n,yy}^{s} - \chi_{n,xy}^{s})\}$$

$$+ \lambda \sum_{n=-\infty}^{\infty} \{a_n(\phi_{n,xy}^{p} + \chi_{n,yx}^{p}) + b_n(\phi_{n,xx}^{s} + \chi_{n,yx}^{s})\}$$

$$\sigma_{xy}^{(s)} = \mu \sum_{n=-\infty}^{\infty} \{a_n(2\phi_{n,xy}^{p} + \chi_{n,yy}^{p} - \chi_{n,xx}^{p}) \qquad (2.7a)$$

$$+ b_n(2\phi_{n,xy}^{s} + \chi_{n,yy}^{s} - \chi_{n,xx}^{s})\} \quad .$$

Here, the notation is as follows:

- superscript (s) denotes the scattered field qualities
- subscripts ,x and ,xx denote, respectively, first and second derivatives with respect to x
- subscripts ,y and ,yy denote, respectively, first and second derivatives with respect to y
- subscripts ,xy or ,yx denote mixed derivatives taken in the order indicated. Note that the mixed derivatives are equal in respect to the order taken.

The first, second and mixed derivatives of the potentials can be determined from the expressions for the potentials given by Eq. (A-33) in Appendix A. The numerical method of evaluating the potentials and their derivatives is discussed in Chapter 3.

2.1.2 Incident and Reflected Field

The free displacements and stress fields are the sum of the incident and reflected fields which, in the absence of a scatterer, are

$$u_j^{(0)} = u_j^{(i)} + u_j^{(r)} \qquad (j = 1,2)$$

$$\sigma_{jk}^{(0)} = \sigma_{jk}^{(i)} + \sigma_{jk}^{(r)} \qquad (j,k = 1,2). \qquad (2.8a)$$

These displacement and stress fields can be expressed in terms of the potentials $\phi^{(i)}$, $\phi^{(r)}$, $\chi^{(i)}$, and $\chi^{(r)}$ from Eqs. (2.4) and (2.5). Note that superscripts (0), (i), and (r) denote free, incident, and reflected field

quantities, respectively. The free displacement and stress fields for incident P, SV, and R waves are summarized in Appendix B.

2.1.3 Total Field

The total displacement field is the sum of the scattered displacement field and the free displacement field so that

$$u_j = u_j^{(s)} + u_j^{(0)} \qquad (j = 1,2). \qquad (2.8b)$$

Similarly, the total stress field is the sum of the scattered stress field and the free stress field, so that

$$\sigma_{jk} = \sigma_{jk}^{(s)} + \sigma_{jk}^{(0)} \qquad (j,k = 1,2). \qquad (2.8c)$$

2.2 The Finite Element and Eigenfunction Expansion Technique (FEEET)

In the FEEET technique, the inhomogeneities in region II are enclosed by a contour or boundary B as shown in Fig. 2.3. Interior region II is subdivided into finite elements having N_I interior nodes and N_B boundary nodes. Region I outside contour B is represented by eigenfunction expansions. The material in region I is assumed to be linear, elastic, isotropic and homogeneous. By using the eigenfunction expansion and imposing the continuity conditions for displacements and forces at a finite number of points on B, an impedance matrix is formed for exterior Region I. Combining this with the finite element impedance matrix of interior Region II, the unknown coefficients of the eigenfunction expansion can be determined. Knowing these coefficients, the displacement and stress fields can be determined anywhere in the semi-infinite plane or half-space.

2.2.1 Representation of the field in Region I

The scattered displacements are given by Eqs. (2.7a). Evaluating Eqs. (2.7a) at each of the boundary nodes on contour B, the scattered nodal displacement vector, $\{q_B^{(s)}\}$, can be written as

$$\{q_B^{(s)}\} = [G]\{a\} \tag{2.9}$$

where [G] is a (2*NB) x (2*NB) matrix formulated in Appendix C and {a} are the unknown coefficients or generalized coordinates.

Similarly, from Eq. (2.7b), the scattered nodal stress vector can be written as

$$\{\sigma_B^{(s)}\} = [F]\{a\} \tag{2.10}$$

where [F] is also a (2*NB)x(2*NB) matrix formulated in Appendix C.

In terms of the nodal displacements, we have from Eqs. (2.10) and (2.9)

$$\{\sigma_B^{(s)}\} = [F][G]^{-1}\{q_B^{(s)}\} \ . \tag{2.11}$$

To avoid the inversion of the [G] matrix in Eq. (2.11), a variational formulation is performed with the generalized coordinates {a} in Eq. (2.10). To this end, the expression for the virtual work done on the boundary B can be written as

$$\delta\pi = \int_B \{\delta q^{*(1)}_B\}^T \{\sigma_B^{(1)}\} d\Gamma \tag{2.12}$$

where superscript (1) denotes the total field in region I, superscript * denotes complex conjugate and superscript T denotes the transpose.

Because of the continuities of displacements and traction forces at the boundary nodes,

$$q_B^{(1)} = q_B^{(2)} = q_B^{(0)} + q_B^{(s)} \tag{2.13}$$

$$\sigma_B^{(1)} = \sigma_B^{(2)} = \sigma_B^{(0)} + \sigma_B^{(s)} \tag{2.14}$$

where superscript (2) denotes the total field in region II.

Substituting Eqs. (2.9), (2.10), (2.13), and (2.14) into Eq. (2.12) and noting that $\delta q_B^{(1)} = \delta q_B^{(s)}$, we have from Eq. (2.12)

$$\delta\pi = \{\delta a^*\}^T \{P_B^{(1)}\} \tag{2.15}$$

where $P_B^{(1)}$ is the generalized interaction force between region I and region II, and it is given by

$$\{P_B^{(1)}\} = [\bar{R}]\{a\} + \{P_B^{(0)}\} \tag{2.16}$$

where
$$[\bar{R}] = \int_B [G^*]^T [F] d\Gamma \tag{2.17}$$

and
$$\{P_B^{(0)}\} = \int_B [G^*]^T \{\sigma_B^{(0)}\} d\Gamma \ . \tag{2.18}$$

Equations (2.17) and (2.18) are approximated by

$$[\bar{R}] = [G^*]^T [F] * R\Delta\theta \tag{2.19}$$

and
$$\{P_B^{(0)}\} = [G^*]^T \{\sigma_B^{(0)}\} * R\Delta\theta \tag{2.20}$$

where $R\Delta\theta$ is the arc length between two adjacent boundary nodes on contour B. Note that the first two rows and last two rows of Eq. (2.19) and Eq. (2.20) are multiplied by $R\frac{\Delta\theta}{2}$ instead of $R\Delta\theta$ because they correspond to the first and last boundary nodes, respectively.

2.2.2 Finite Element Representation in Region II

As shown in Fig. 2.3, Region II, which is bounded by contour B of radius R, contains all the scattering inhomogeneities and anisotropy. Region II is subdivided into finite elements having N_I number of interior nodes and N_B number of boundary nodes.

For the interior finite element representation in region II, the appropriate functional for minimization is

$$F = \frac{1}{2} \iint_{R_{II}} (\sigma \cdot \xi^* - \rho\omega^2 u \cdot u^*) dx dy - \frac{1}{2} \int_B (P_B \cdot u_B^* + P_B^* \cdot u_B) ds \tag{2.21}$$

where * indicated complex conjugate and σ, ξ are column vectors defined as

$$\sigma = \{\sigma\} = (\sigma_{xx}, \sigma_{yy}, \sigma_{xy})^T$$

$$\xi = \{\xi\} = (\xi_{xx}, \xi_{yy}, \xi_{xy})^T \ .$$

Superscript T denotes transponse. The P_B and u_B represent the traction force and displacement at contour B, respectively.

Assuming the displacement field within the j^{th} element is represented in terms of the shape functions $L_j(x,y)$ and elemental nodal displacements $\{q_j^e\}$ as

$$u^e = \sum_{j=1}^{Ne} [L_j]\{q_j^e\} \tag{2.22}$$

where each q_j^e has two components u_{xj} and u_{yj} along the x and y directions, respectively. The Ne represents the number of nodes in each element.

The σ_{ij}^e and ξ_{ij}^e are computed by substituting Eq. (2.22) into strain-displacement relations and these, in turn, into the stress-strain relations. Using these in Eq. (2.21), we get

$$F = \underset{\sim}{q}^{*T}_I S_{II} \underset{\sim}{q}_I + \underset{\sim}{q}^{*T}_I S_{IB} \underset{\sim}{q}_B + \underset{\sim}{q}^{*T}_B S_{BI} \underset{\sim}{q}_I \tag{2.23}$$
$$+ \underset{\sim}{q}^{*T}_B S_{BB} \underset{\sim}{q}_B - \underset{\sim}{q}^{*T}_B P_B^{(1)} - \underset{\sim}{P}^{*T(1)}_B \underset{\sim}{q}_B$$

in which $\underset{\sim}{q}_I = \underset{\sim}{q}_I^{(2)}$, $\underset{\sim}{q}_B = \underset{\sim}{q}_B^{(2)}$, $\underset{\sim}{P}_B^{(1)} = \underset{\sim}{P}_B^{(2)}$ and the elemental impedance matrices S_{ij} are defined as

$$[S^e] = \iint_{Re} ([B^e]^T[D][B^e] - \rho_e\omega^2[L]^T[L])\, dxdy \, . \tag{2.24}$$

In Eq. (2.24,)

$$[B^e] = \begin{bmatrix} \frac{\partial}{\partial x} & 0 \\ 0 & \frac{\partial}{\partial y} \\ \frac{\partial}{\partial y} & \frac{\partial}{\partial x} \end{bmatrix} \begin{bmatrix} L_1 & 0 & L_2 & .. \\ 0 & L_1 & 0 & .. \end{bmatrix} = [N][L] \, .$$

Note that [L] is a $2x2N_e$ matrix.

For an isotropic material [D] is given by

$$[D] = \begin{bmatrix} \lambda_e + 2\mu_e & \lambda_e & 0 \\ \lambda_e & \lambda_e + 2\mu_e & 0 \\ 0 & 0 & \mu_e \end{bmatrix}$$

where λ_e and μ_e are the Lame's constant.

Substituting Eq. (2.9) into Eq. (2.23) and taking the variation, we obtain a set of simultaneous equations which may be written in matrix form as

$$\begin{bmatrix} S_{II} & S_{IB}G_I \\ G^{*T}S_{IB}^T & G^{*T}S_{BB}G \end{bmatrix} \begin{bmatrix} \underset{\sim}{q}_I \\ \underset{\sim}{a} \end{bmatrix} = \begin{bmatrix} -S_{IB}\underset{\sim}{q}_B^{(0)} \\ -G^{*T}S_{BB}\underset{\sim}{q}_B^{(0)} + \underset{\sim}{P}_B^{(1)} \end{bmatrix}. \tag{2.25}$$

The first equation of Eq. (2.25) can be written as

$$\underset{\sim}{q}_I = -S_{II}^{-1}[S_{IB}G\underset{\sim}{a} + S_{IB}\underset{\sim}{q}_B^{(0)}] \ . \tag{2.26}$$

The second equation can be written as

$$G^{*T}S_{IB}^T \underset{\sim}{q}_I + G^{*T}S_{BB}G \underset{\sim}{a} = -G^{*T}S_{BB}\underset{\sim}{q}_B^{(0)} + \underset{\sim}{P}_B^{(1)} \ . \tag{2.27}$$

Substituting Eqs. (2.16) and (2.26) into Eq. (2.27), we obtain

$$[G^{*T}(S_{BB} - S_{IB}^T S_{II}^{-1} S_{IB})\, G^* - \bar{R}]\, \{\underset{\sim}{a}\} =$$

$$- G^{*T}(S_{BB} - S_{IB}^T S_{II}^{-1} S_{IB})\underset{\sim}{q}_B^{(0)} + \underset{\sim}{P}_B^{(0)} \tag{2.28}$$

In Eq. (2.28), the generalized coordinates {a} are the only unknowns. Therefore, {a} can be evaluated. Once {a} are known, the near and far displacement and stress fields can be determined.

CHAPTER 3. NUMERICAL SCHEME

The potentials ϕ_n^P, χ_n^P, ϕ_n^S, and χ_n^S are derived in Appendix A. However, their first, second and cross derivatives with respect to x and y must be evaluated numerically in order to formulate the matrixes [G] and [F] listed in Appendix C. In this chapter, such a numerical scheme is discussed. The same numerical scheme is used to evaluate both the potentials and their derivatives because they are of similar integral form. In the following paragraphs, only the potentials are mentioned.

3.1 Contour of Integration

The potentials ϕ_n^P, χ_n^P, ϕ_n^S, and χ_n^S can be integrated from 0 to ∞ and written as

$$\phi_n^P = H_n(k_1 r)e^{in\theta} + \frac{i}{\pi}\int_0^\infty \left[1 + \frac{8k^2\nu_1\nu_2}{F(k)}\right]\frac{e^{-\nu_1(h+y)}}{\nu_1} \left\{\left(\frac{k+\nu_1}{k_1}\right)^n e^{ikx} + \left(\frac{-k+\nu_1}{k_1}\right)^n e^{-ikx}\right\} dk \tag{3.1}$$

$$\chi_n^P = -\frac{4}{\pi}\int_0^\infty \frac{(2k-k_2^2)}{F(k)}e^{-\nu_1 h-\nu_2 y}\left\{k\left(\frac{k+\nu_1}{k}\right)^n e^{ikx} - k\left(\frac{-k+\nu_1}{k}\right)^n e^{-ikx}\right\} dk \tag{3.2}$$

$$\phi_n^S = \frac{4}{\pi}\int_0^\infty \frac{(2k-k_2^2)}{F(k)}e^{-\nu_2 h-\nu_1 y}\left\{k\left(\frac{k+\nu_2}{k_2}\right)^n e^{ikx} - k\left(\frac{-k+\nu_2}{k}\right)^n e^{-ikx}\right\} dk \tag{3.3}$$

$$\chi_n^S = H_n(k_2 r)e^{in\theta} + \frac{i}{\pi}\int_0^\infty \left(1 + \frac{8k^2\nu_1\nu_2}{F(k)}\right)\frac{e^{-\nu_2 h-\nu_2 y}}{\nu_2}\left\{\left(\frac{k+\nu_2}{k_2}\right)^n e^{ikx} + \left(\frac{-k+\nu_2}{k}\right)^n e^{ikx}\right\} dk \tag{3.4}$$

where H_n is the Hankel function of the first kind.

Equations (3.1) to (3.4) were used to evaluate the potentials corres-

ponding to successive terms ±n. Twenty such terms were found to be required in order for Eq. 2.6 to converge. For the numerical values presented in this thesis, twenty-four terms of n were taken from -11 to 12: that is $-(\frac{NB}{2} - 1)$ to $\frac{NB}{2}$. NB is taken as 24, where NB is the number of boundary nodes.

The choice of integration contours for the integrals in Eq. (3.1) to Eq. (3.4) is governed by the integral definition of the function. $H_n\ e^{in\theta}$ in Appendix A requiring the contour c_1 such that

$$\text{Re } \sinh(s) \leq 0 \text{ and Im } \sinh(s) > 0$$

but $$k_1 \sinh(s) = -\nu_1, \text{ and } k_2 \sinh(s) = -\nu_2 .$$

Therefore, $$\text{Re } (\nu_1) \geq 0 \text{ and Re } (\nu_2) \geq 0 \qquad (3.5)$$

and $$\text{Im } (\nu_1) < 0 \text{ and Im } (\nu_2) < 0 . \qquad (3.6)$$

The ν_1 and ν_2 are also defined as

$$\nu_1 = \sqrt{k^2 - k_1^2} \quad \text{and} \quad \nu_2 = \sqrt{k^2 - k_2^2} .$$

Here k_1 and k_2 are the pressure and shear wave numbers, respectively.

The integration contour in Fig. (3.1) is chosen to both satisfy Eq. (3.5) and Eq. (3.6) and to avoid the numerical complication associated with the pole at $k=k_R$, where k_R is the Rayleigh wave number.

To compute the integrals, the domain k is transformed to domain u as follows:

Path Γ_1

$$\text{let } k = -iu \quad \rightarrow \quad dk = -idu$$

$$\int_0^{-ih} Q\, dk = -\int_0^{h} Q\, idu$$

Path Γ_2

$$\text{let } k = u - ih \quad \rightarrow \quad dk = du$$

$$\int_{-ih}^{g-ih} Q\, dk = \int_0^{g} Q\, du$$

Path Γ_3

let $k = g - ih + iu \rightarrow dk = idu$

$$\int_{g-ih}^{g} Q\, dk = \int_{0}^{h} Q\, idu$$

Path Γ_4

let $k = u \rightarrow dk = du$

$$\int_{g}^{\infty} Q\, dk \cong \int_{g}^{\ell} Q\, du$$

where Q is the kernel of the integrals and ℓ in path Γ_4 is the last point of integration. The ℓ is determined by a convergence study.

A complication arises with the sign of $Im(\nu_1)$ and $Im(\nu_2)$ which do not satisfy Eq. (3.6) on path Γ_1. The ν_1 and ν_2 are evaluated by the Fortran statement CDSQRT. CDSQRT evaluates only one root of a complex number. The real part of the root is always taken as positive so that Eq. (3.5) is always satisfied. However, the sign of the imaginary part of the root depends on the quadrant in which the original complex number lies. To demonstrate this point, the root of a complex number x + iy is evaluated by the Fortran statement CDSQRT. The results are shown in Table 1. It can be seen that the imaginary part of the root is only negative when the complex number lies in the third and fourth quadrants. However, ν_1^2 and ν_2^2 on path Γ_1 always lie on the negative real axis. This is demonstrated straightforwardly as follows:

On path Γ_1, $k = -iu$ and $u > 0$

$$\nu_1^2 = k^2 - k_1^2 = (-iu)^2 - k_1^2$$

$$= -(u^2 + k_1^2)$$

$$\nu_1 = \pm i\sqrt{u^2 + k_1^2} \quad .$$

As $u \rightarrow h$, ν_1^2 always lies on the negative real axis. Hence, the statement CDSQRT (ν_1^2) evaluates the positive imaginary root. Therefore, Eq. (3.6) is not satisfied because it requires the imaginary root to be negative. In

order to satisfy Eq. (3.6), ν_1 is defined as $-\nu_1$ on this path. Similarly, ν_2 is defined as $-\nu_2$.

Such a problem does not occur on paths Γ_2, Γ_3, and Γ_4. On path Γ_2, it can be shown straightforwardly that ν_1^2 and ν_2^2 always lie in the third or fourth quadrant and on path Γ_3, ν_1^2 and ν_2^2 lie in the fourth quadrant. Therefore, CDSQRT calculates the imaginary parts of ν_1^2 and ν_2^2 as negative. On path Γ_4, ν_1^2 and ν_2^2 always lie on the positive real axis and consequently have real roots. Therefore, Eq. (3.6) is not required and there is no problem.

3.2 Accuracy of the Numerical Scheme

The integral representation of

$$H_n(k_1 r)e^{in\theta} = \frac{-i}{\pi}\int_0^\infty \frac{e^{-\nu_1 h+\nu_1 y}}{\nu_1}\left[\left(\frac{k+\nu_1}{k_1}\right)^n e^{ikx} + \left(\frac{-k+\nu_1}{k_1}\right)^n e^{-ikx}\right] dk \qquad (3.7)$$

can be evaluated by using the numerical scheme mentioned in Section 3.1. Alternatively, an exact evaluation of $H_n(k_1 r)$ is available from an IMSL subroutine. Therefore, the numerical scheme can be tested by evaluating the integral form of $H_n(k_1 r)e^{in\theta}$ and comparing it with the exact value of $H_n(k_1 r)$ multiplied by $e^{in\theta}$. Since the integral form of $H_n(k_1 r)e^{in\theta}$ is similar to Eq. (3.1) to Eq. (3.4) and their derivatives, this comparison gives a valid test of the accuracy of the numerical scheme.

The trapezoidal rule was employed in the numerical scheme and was found to be accurate provided that the size of each interval, Δ, is sufficiently small. As an example, the values of $H_n(k_1 r)e^{in\theta}$ at a point x = 3.0 and y = 0.0 were computed by the numerical scheme and compared with the values computed by the IMSL subroutine. The values from both methods, for a few selected n, are shown in Table 2. They compare well. The choice of Δ and the path limit parameters h, g, and ℓ as shown in Fig. 3.1 for the numerical scheme is discussed in the following paragraphs.

The choice of h was made on the basis of the convergence properties of the integrals on path Γ_1, Γ_2, and Γ_3. The range of values $0.1 \leq h \leq 0.5$ was found to give consistent convergence. An intermediate value $h = 0.25$ was chosen for convenience.

Path limit g is chosen to be greater than k_R to avoid the numerical difficulties associated with the pole at $k = k_R$. The Rayleigh wave number, k_R, can be approximated by $k_R = \frac{1 + \nu}{0.862 + 1.14\nu} k_2$ where ν is the Poisson's ratio and k_2 is the shear wave number. The ν is taken as 1/3. Path limit $g = 3.5$ is chosen because it is greater than k_R for the range of k_2 used in this thesis.

A convergence study was performed by using the path limits described above. The integral form of Eq. 3.7 was found to have converged at $\ell = 30$.

The kernels of the integrals are oscillating functions. Therefore, two difficulties can arise when choosing Δ to numerically evaluate the integrals. When $|n| \geq 7$, the magnitude of each point of integration is large and, therefore, a small Δ is needed to compute the integrals accurately. Also, when x is large, the wavelength of each oscillation of the kernel is short and a small Δ is needed to evaluate the magnitude of the integrals within each wavelength. On paths Γ_1, Γ_2, Γ_3, and Γ_4, the interval $\Delta = 0.01$ was found to be sufficiently small to evaluate the integrals for all values of n provided $x \leq 5.0$. On path Γ_4, the larger interval $\Delta = 0.05$ may be used unless $|n| \geq 7$ and $2.5 \leq x \leq 5.0$. The situation $x \geq 5.0$ would require a Δ smaller than 0.01 and hence more computer time will be required. In that case, the author would suggest the use of Filon's integration formula [20]. However, the situation $x > 5.0$ is not encountered in the present study. The author has also employed two other numerical schemes to compute Eq. (3.7). Both of these schemes employed integration along the real axis. In one scheme the variable k was used

directly as the variable of integration and, in another scheme, variable k was transformed to $k = k_1 \sin(u)$ if $k < k_1$ and $k = k_1 \cosh(u)$ if $k > k_1$. The transformation was used to avoid numerical singularities at $k = k_1$ and $k = k_2$. It was found that these two numerical schemes give the same results and required the same computing time as the contour integration. However, the contour integration scheme was chosen because it is the simplest and the easiest to program.

CHAPTER 4. DYNAMIC STRESSES AND DISPLACEMENTS IN BURIED PIPE

In this chapter, the proposed hybrid combined finite element and eigenfunction expansion technique (FEEET) is used to study the scattering of elastic waves, P, SV and Rayleigh, by pipelines in a semi-infinite elastic medium. The task is to find the resultant dynamic stresses and displacements at the outer circumference of the pipeline. Two problems are considered. The first problem is a pipeline embedded in a rectangular trench of backfill (Fig. 4.1) and the second problem is two pipelines lying parallel to each other in a similar backfilled trench (Fig. 4.2). The finite element meshes for the above two problems are shown in Fig. 4.3 and Fig. 4.4, respectively. The pipelines are assumed to be infinitely long, continuous, cylindrical shells of inner and outer radii, r = A and C, respectively, lying parallel to the free plane surface of semi-infinite medium. Since a plane strain problem is considered, the waves are propagating perpendicular to the axes of the pipelines.

The numerical results presented in sections 4.1 and 4.2 are for a concrete shell of thickness ratio T/A = (C-A)/A = 0.1 and depth ratio H/A = 5.0. Typical material properties are assumed as follows:

(a) for concrete:

ρ = mass density = $2.24 * 10^{3}$ kg/m^{3}

E = Young's modulus = $1.6 * 10^{10}$ N/m^{2}

ν = Poisson's ratio = 0.2

(b) for the backfill:

ρ = 2.685×10^{3} kg m^{3}

E = 6.9×10^{8} N/m^{2}

ν = 0.45

(c) for the surrounding soil:

$\rho = 2.665 \times 10^3$ kg/m^3

$E = 7.567 \times 10^9$ N/m^2

$\nu = 0.333$

The total radial displacements and the hoop stresses at the outer shell boundary, r = C, are computed as functions of the shear wave number, k_2, and the angle of incidence, γ. All figures will be plotted by using the polar coordinates, r and θ, defined in Fig. 4.1 and 4.2. The total radial displacement and the hoop stress are normalized with respect to the maximum free field radial displacement and hoop stress, respectively, at r = C. The normalized total radial displacement is denoted by UN and the normalized total hoop stress is denoted by STT. The normalization factors are denoted by NF. Also, the angles of incidence are denoted as GAMMA (γ). The k_2A is the dimensionless frequency. It is also the number of complete wavelengths contained in the radial distance A.

To justify the numerical results presented later in this chapter, the normalized total radial displacements, UN, and the hoop stresses, STT, at r = C of a concrete pipe obtained by using the FEEET program will be compared with those results obtained by the analytical method of reference [3]. The results are for the case of the pipe without backfill material. Results for incident P and SV waves at $\gamma = 0°$ are shown in the polar plot of Fig. 4.5(a) and 4.5 (b), respectively. In Fig. 4.5, results are symmetrical about the vertical axis as expected, because the waves are incident at $\gamma = 0°$. For convenience, the values of the normalized displacement, UN, are shown on the left side of the pipe and the values of the normalized stress, STT, on the left side. The scales for UN and STT are given on the left and right

horizontal axis, respectively. The scale for UN is drawn by the computer plotter for convenience. To understand the polar plot of Fig. 4.5 (a), the circular dotted line represents the outer circumference of the pipe. The displacement at location ρ is marked with an x and the magnitude of the displacement can be read from the left horizontal axis. In other figures, the circumference of the pipe is not drawn, but similar interpretation applies. The two solutions agree well. Results for incident Rayleigh waves have also been checked, and are not shown here. This comparison validates the use of the FEEET and the results for more complicated geometries will be considered in the next two sections. No analytical solution is possible for these more complex problems.

In section 4.1, the numerical results are presented for a single pipeline embedded by a rectangular trench of backfill. In section 4.2, numerical results are presented for two pipelines lying parallel to each other in a rectangular trench of backfill.

4.1 Single Pipeline Embedded in a Rectangular Trench of Backfill

A pipeline embedded in a rectangular trench of backfill is a common practical situation. The distribution of the normalized total radial displacements, UN, and hoop stresses, STT, at the outer boundary of the concrete pipe can be observed in Figs. 4.6 to 4.11, inclusive. The incident disturbances are P, SV and Rayleigh waves. In all cases, the total radial displacements and hoop stresses increase with increasing frequency. In general, larger stresses are found to occur for incident SV waves than for P and Rayleigh waves. Also, the angle of incidence has a significant effect on the radial displacements and hoop stresses for SV waves. This is not true for P waves. In general, for all incident waves at low frequencies, $k_2A \leq 0.12$, results are symmetrical about the diameter of the pipe which is aligned with

the incident wave. However, at higher frequencies, $k_2A \geq 0.3$, results are asymmetrical except for 0° incident waves. Further detailed observations are listed in section 4.1.1, 4.1.2 and 4.1.3. The observations are classified according to whether the incident waves are P, SV or Rayleigh.

It should be noted that in the following sections, any position on the pipe's circumference is indicated by the angle θ as shown in Fig. 4.1. The angle is measured clockwise from the upward vertical. Therefore, the crown of the pipe is at $\theta = 0°$, and the base of the pipe is at $\theta = \pm 180°$.

4.1.1 P Wave

Figure 4.6(a) shows the normalized radial displacements, UN, and hoop stresses, STT, at 0° angle of incidence for four different dimensionless frequencies. All results are symmetrical about the vertical axis as expected. For convenience, the values of STT are shown in the right side of the pipe, and the values of UN on the left side. At the three lower frequencies, the maximum values of UN occur at the crown of the pipe. On the other hand, at the highest frequency considered, UN is maximum at the base of the pipe. In the same figure, the maximum values of STT occur at $\theta = \pm 60°$, except for the highest frequency considered. Then, the maximum occurs at the crown of the pipe ($\theta = 0°$).

For P waves at 45° incidence as shown in Fig. 4.7, the distributions of UN corresponding to low frequencies are different from those at higher frequencies. At low frequencies, UN is symmetrical about the diameter of the pipe which is aligned with the incident wave. Maximum values occur on the upper right side of the pipe at $\theta = 45°$. At the two higher frequencies, there is no symmetry and maximum values for $k_2A = 0.30$ and $k_2A = 0.60$ occur at $\theta = 15°$ and $\theta = -135°$, respectively. The distribution of STT is symmetrical about both the vertical and horizontal diameter at the lowest frequency,

and maximum occurs at the crown of the pipe. However, STT distribution becomes less symmetrical at the two intermediate frequencies and the maximum value is largest on the upper left side of the pipe at $\theta = -45°$. In contrast, at the highest frequency, the maximum occurs at the base of the pipe at $\theta = 180°$.

Figure 4.8 elaborates the variation of UN and STT with the angle of incidence γ, for a particular value of $k_2A = 0.12$. The distribution of UN is symmetrical about the pipe diameter aligned with the wave propagation. Maximum values of UN occur on the upper right side of the pipe at angles θ equal γ and are approximately equal in magnitude regardless of the incident angle. The distributions of STT are almost symmetrical about the diameter aligned with the incident wave. The magnitude of the maximum STT is fairly constant and occurs at $\theta = \gamma \pm 90°$.

4.1.2 SV Wave

Figure 4.6 (b) shows the distribution of normalized radial displacements and hoop stresses scattered by SV waves at 0° angle of incidence. Results are symmetrical about the vertical diameter of the pipe as expected. Therefore, only one half of the results are shown. The distributions of UN vary significantly with frequency. Nevertheless, maximum values of UN occur invariably on the lower half of the shell at $\theta = \pm 135°$. In the same figure, the lowest three frequencies produce maximum values of STT at $\theta = \pm 135°$. The distribution of STT at the highest frequency is distinctively different and the maximum value occurs at $\theta = \pm 60°$.

At a 45° angle of incidence as shown in Fig. 4.9, the distribution of UN is symmetrical about the vertical diameter at the two lowest frequencies. At higher frequencies, UN becomes progressively asymmetric. Maximum UN occurs on the crown or the upper left part of the shell, depending on the frequency

considered. The distribution of STT is symmetrical about both the vertical and horizontal diameters at the two lowest frequencies. At higher frequencies, STT is asymmetric, and the maximum values are significantly larger. They occur at $\theta = -60°$.

Figure 4.10 elaborates on the variation of UN and STT with the angle of incidence, γ, for $k_2A = 0.12$. Each distribution of UN is symmetrical and "figure-eight" shaped. However, there is no apparent relation between the orientations of these shapes and the angles of incidence. It can be illustrated that by using the normalization factor, absolute radial displacement is largest at the critical angle* at $\gamma = 30°$. The angle of incident of SV waves has a significant effect on the hoop stresses. Like the radial displacement, hoop stress is largest at the critical angle. On the other hand, incidence angle greater than the critical angle has little scattering effect.

4.1.3 Rayleigh Wave

Fig. 4.11 shows the distributions of UN and STT for four different frequencies. The distribution of UN is symmetric about the vertical pipe diameter at low frequencies. As frequency increases, UN becomes progressively asymmetric. At the three lower frequencies, the maximum occurs at the crown of the pipe, whereas at the highest frequency, it occurs at $\theta = -30°$. The distribution of STT is symmetrical about the vertical diameter at the two lower frequencies, and the maximum occurs at $\theta = 0°$. As frequency increases, STT becomes progressively asymmetric, and the maximum occurs at the upper right side of the pipe at $\theta = 45°$ for $k_2A = 0.3$ and at $\theta = 75°$ for $k_2A = 0.60$.

---

* It can be shown by Snell's law that the critical angle for free incident SV waves is 30°, since the Poisson's ratio of the host material is taken as 1/3. The critical angle is the incident angle such that the reflected P wave will be tangential to the free surface.

4.2 Two Pipes Lying Parallel to Each Other in a Rectangular Backfilled Trench

In a practical situation, two or more pipes lying in the same rectangular trench are common. Therefore, the second scattering problem studied in this chapter is the dynamic response of one pipe in the presence of another as shown in Fig. 4.2. The normalized total radial displacements and hoop stresses of the left pipe are presented in Figs. 4.12 to 4.16. The overall trends are similar to those observed for a single pipe, that is, the total radial displacements and hoop stresses increase with increasing frequency and larger stresses are created by incident SV waves than by P and Rayleigh waves. Nevertheless, the presence of one pipe has a significant effect on the other pipe. For the P wave, the distribution of STT was significantly affected by the second pipe, but not the distribution of UN. Compared to the results of the singular pipe, the magnitudes of both UN and STT are fairly similar at the three lower frequencies, but the results are amplified at the highest frequency. For the SV wave, UN at the two lower frequencies are not affected by the second pipe, but at the two higher frequencies, the results are amplified. Also, STT was amplified at the three lower frequencies, but reduced at the highest frequency. For Rayleigh wave, both the distribution of UN and STT are significantly affected by the presence of the second pipe, and both magnitudes are reduced. Further detailed observations are listed in sections 4.2.1, 4.2.2, and 4.2.3. The observations are classified according to whether the incident waves are P, SV or Rayleigh.

4.2.1 P Wave

Figure 4.12 shows the distribution of the normalized radial displacements, UN, and hoop stresses, STT, at 0° angle of incidence for four different dimensionless frequencies. The distribution of UN is symmetrical about

the vertical axis at the three lower frequencies. Maximum values occur at the crown of the shell at $\theta = 0°$. At the highest frequency, UN is asymmetrical, and the maximum occurs at the case of the shell at $\theta = 180°$. This is also true for the case of the single pipe in section 4.1.1. The effect of the second pipe has little effect on UN at low frequencies. The distribution of STT is symmetrical about the vertical and horizontal axes and the maximum occurs at $\theta = 90°$ for all frequencies. This is not true for a single pipe.

Figure 4.13 shows the distribution of UN and STT at different angles of incidence for $k_2A = 0.12$. The distribution of UN is similar to that for the single pipe. The distribution of STT varies significantly with the angle of incidence. The location of the maximum depends upon the angle of incidence, although the maximum magnitude is almost constant.

4.2.2 SV Wave

Fig. 4.14 shows the distribution of the normalized radial displacements, UN, and hoop stresses, STT, at 0° angle of incidence for different dimensionless frequencies. UN is nearly symmetrical about the vertical axis at all frequencies. At $k_2A = 0.3$, the distribution of UN is distinctively different from the other frequencies. Maximum UN occurs at the upper part of the shell and the location depends on the frequency considered. At the three lower frequencies, the distribution of STT is symmetrical about the horizontal axis and the maximum occurs at $\theta = 45°$. At the highest frequency, the distribution is completely different and the maximum occurs at $\theta = -45°$. As compared to the stresses of the single pipe, the magnitude are significantly amplified at the three lower frequencies and reduced at the highest frequency.

Figure 4.15 shows the distribution of UN and STT with the angle of incidence for $k_2A = 0.12$. The distribution and magnitude of UN are almost identical to that of the single pipe. The distribution and magnitude of STT

are affected by the second pipe at different angles of incidence. The magnitude at 0° incidence is significantly amplified.

4.2.3 Rayleigh Wave

Figure 4.15 shows the distribution of the normalized radial displacements, UN, and hoop stresses, STT, for different dimensionless frequencies. The distribution of UN is symmetrical about the vertical axis for low frequencies. As frequency increases, UN becomes more asymmetrical. Maximum values occur at the crown of the shell at $\theta = 0°$ for all frequencies. The distributions of STT are asymmetrical at all frequencies and are different from each other. The location of the maximum depends upon the frequency considered. The distribution of UN and STT are significantly affected by the presence of the second pipe, and both magnitudes are reduced at all frequencies.

4.3 Conclusions

Variations of the normalized radial displacements and hoop stresses at the outer circumference of the pipeline(s) are presented. The dynamic responses of the pipeline(s) are significantly dependent on the frequency, the angle of incidence, and the nature of the incident waves.

In the case of the single pipe, the total radial displacements and hoop stresses increase with increasing frequency. Larger hoop stresses are found to occur for incident SV waves than for P and Rayleigh waves. Also, the angle of incidence has a significant effect on the radial displacements and hoop stresses for SV waves but not for P waves.

In the case of two pipes, the overall trenches of the normalized total radial displacement and hoop stress of the left pipe are similar to those observed for a single pipe. That is, the total radial displacements and hoop stresses increase with increasing frequency and larger stresses are created

by SV waves than by P and Rayleigh waves. Nevertheless, the presence of one pipe has a significant effect on the other pipe.

For design purposes, it is recommended that an SV wave incident at a critical angle should be used to determine the hoop stresses, and more detailed parametric study is needed to provide design guidelines. In the case of two or more pipes, the effect of the other pipe(s) has to be taken into account.

CHAPTER 5. SCATTERING OF ELASTIC WAVES BY SURFACE BREAKING CRACKS

The proposed FEEET is further employed to study the scattering of elastic waves by surface breaking cracks. This chapter presents the stress intensity factors and surface displacements due to the scattering of P, SV and Rayleigh waves by three types of surface breaking cracks: a vertical crack (Fig. 5.1 with $\alpha = 90°$), a 45° inclined crack (Fig. 5.1 with $\alpha = 45°$), and a vertical branched (Y) crack (Fig. 5.2). Figure 5.3 shows the crack tip elements and Fig. 5.4 to Fig. 5.6 show the finite element meshes of the three cracks.

5.1 Stress Intensity Factors

The stress intensity factors are K_I and K_{II} which correspond to the opening mode I and the shearing mode II, respectively. They are calculated from the crack opening displacement (COD) near a crack tip by the relations:

$$\begin{bmatrix} K_I \\ \\ K_{II} \end{bmatrix} = \frac{\mu}{2(1-\nu)} \begin{bmatrix} \bar{K}_I \\ \\ \bar{K}_{II} \end{bmatrix} \tag{5.1}$$

where

$$\begin{bmatrix} \bar{K}_I \\ \\ \bar{K}_{II} \end{bmatrix} = \tfrac{1}{2}\,(1/L)^{\frac{1}{2}} \begin{bmatrix} \Delta_1 \\ \\ \Delta_2 \end{bmatrix} \tag{5.2}$$

and $\Delta_1 = 4(U_6 - U_4) - (U_3 - U_2)$

$\Delta_2 = 4(V_6 - V_4) - (V_3 - V_2)$

In the above equations, U_i and V_i represent the displacement components u_x and u_y respectively at the ith node. The nodes 2, 3, 4, and 6 and the length of the crack tip element, L, are defined in Fig. D4 in Appendix D. Appendix D is reproduced from Appendix 3.3 of reference [3].

To justify the numerical results presented later in this chapter, the

COD and the stress intensity factors obtained using the FEEET program will be compared with the results in reference [10]. In this case, the scatterer is a surface breaking vertical crack and the incident field is a Rayleigh wave. However, the crack-face loading of the present study and reference [10] are different. In order to make a comparison the FEEET results must be normalized as explained below.

In reference [10], the general form of crack-face loading which corresponds to the traction in the x-direction induced by an arbitrary surface disturbance in a semi-infinite medium is

$$\frac{\sigma_x}{\mu} = 2Ak_R Di \left\{ \frac{2k_R^2 - 2k_1^2 + k_2^2}{2k_R^2 - k_2^2} e^{-\bar{\alpha}y} - e^{-\bar{\beta}y} \right\} \tag{5.4}$$

and in our present study,

$$\frac{\sigma_x}{\mu} = 2Bk_R \beta i \left\{ \frac{2k_R^2 - 2k_1^2 + k_2^2}{2k_R^2 - k_2^2} e^{-\bar{\alpha}y} - e^{-\bar{\beta}y} \right\} \tag{5.5}$$

where $\bar{\alpha} = \sqrt{k_R^2 - k_1^2}$, $\bar{\beta} = \sqrt{k_R^2 - k_2^2}$, and D is the crack length. Comparing Eq. (5.4) and Eq. (5.5) and letting B = 1, we get $|A| = \bar{\beta}/D$.

Substituting $|A| = \bar{\beta}/D$ and after manipulating, the normalization factor for the COD is $1/\bar{\beta}$ and for the stress intensity factor is $D^{\frac{1}{2}}/\bar{\beta}$. Hence, $\Delta\bar{U}$ and $\Delta\bar{V}$ in Fig. 5.7 are defined as $\Delta_1/\bar{\beta}$ and $\Delta_2/\bar{\beta}$ respectively, and K_I° and K_{II}° in Fig. 5.8 are defined as $\bar{K}_I D^{\frac{1}{2}}/\bar{\beta}$ and $\bar{K}_{II} D^{\frac{1}{2}}/\bar{\beta}$ respectively, where Δ_1 and Δ_2 are the COD defined in Eq. (5.3), and $\bar{K}_I$ and $\bar{K}_{II}$ are the normalized stress intensity factors defined in Eq. (5.2). Thus

$$\Delta\bar{u} = \Delta_1/\bar{\beta} \quad ; \quad \Delta\bar{v} = \Delta_2/\bar{\beta}$$

$$k_I^0 = \bar{k}_I D^{\frac{1}{2}}/\bar{\beta} \quad ; \quad k_{II}^0 = \bar{k}_{II} D^{\frac{1}{2}}/\bar{\beta}$$

and $$\bar{\beta} = \sqrt{k_R^2 - k_2^2} \, . \tag{5.6}$$

After normalization, the FEEET results compare well with the results in reference [10] as shown in Fig. 5.7 and 5.8. Therefore, the FEEET and the present program are justified.

Next, the normalized stress intensity factors $\bar{K}_I$ and $\bar{K}_{II}$ at the crack tips of the three types of crack due to incident P and SV waves at 0°, 45° and 75° angle of incidence and Rayleigh waves are plotted against the dimensionless frequency, k_2D, in Figs. 5.9 to 5.15, inclusive. Note that the present normalization factor is $\mu/2(1-\nu)$ as shown in Eq. (5.1). Comparison of the results show considerably different responses at the tips of the three different types of crack. Nevertheless, the mode I ($\bar{K}_I$) normalized stress intensity factors are invariably larger than the mode II ($\bar{K}_{II}$) normalized stress intensity factors. Also, it should be noted that the Y-crack has two tips, A and B. However, in the case of scattering of P and SV waves at 0° incidence, the intensities are equal at tips A and B because of symmetry.

Further detailed trends which can be observed from Figs. 5.9 to 5.15 are listed in Sections 5.1.1., 5.1.2, and 5.1.3. The observations are classified according to whether the incident waves are P, SV or Rayleigh.

5.1.1 P Wave

Figures 5.9 to 5.11 show the mode I ($\bar{K}_I$) and mode II ($\bar{K}_{II}$) normalized stress intensity factors of the three cracks due 0°, 45°, and 75° incidence P waves.

At 0° incidence, the 45° inclined crack shows different trend of $\bar{K}_I$ from the other two cracks. $\bar{K}_I$ for the 45° inclined crack increases with frequency, whereas for the vertical and Y crack, $\bar{K}_I$ increases and then decreases with frequency. Note that $\bar{K}_{II}$ is zero for the vertical crack. This is also true for a sub-surface vertical crack [3]. All three cracks show a different trend of $\bar{K}_{II}$.

At 45° incidence, all three cracks show a similar trend of $\bar{K}_I$ increasing with frequency except at tip A of Y crack at high frequencies. $\bar{K}_{II}$ for all three cracks also increases with frequency, but at a different rate. It is

interesting to know that $\bar{K}_I$ and $\bar{K}_{II}$ at both tips of Y crack are generally equal, but diverge at high frequencies.

At 75° incidence, all three cracks show similar trend of $\bar{K}_I$ increasing with frequency. The 45° inclined crack shows different trend of $\bar{K}_{II}$ from the other two cracks. There is a distinct peak at intermediate frequency.

5.1.2 SV Wave

Figures 5.12 to 5.14 show mode I ($\bar{K}_I$) and mode II ($\bar{K}_{II}$) normalized stress intensity factors of the three cracks due to 0°, 45°, and 75° incidence SV waves. Since $\nu = 1/3$, the critical angle is 30°. $\bar{K}_I$ and $\bar{K}_{II}$ are generally larger, due to SV waves than those due to P and Rayleigh waves (see Fig. 5.15).

At 0° incidence, $\bar{K}_I$ for the vertical crack is zero. This is also true for a sub-surface vertical crack [3]. All three cracks show a different trend of $\bar{K}_I$. In contrast to $\bar{K}_I$, the vertical crack has the largest intensity for $\bar{K}_{II}$.

At 45° incidence, all three cracks show similar trend of $\bar{K}_I$ increasing with frequency at low frequencies, but at high frequencies, values of $\bar{K}_I$ diverge. All three cracks show different trend of $\bar{K}_{II}$. Note that $\bar{K}_{II}$ for the vertical crack is zero, and for the Y crack, $\bar{K}_{II}$ at both tips are equal. The 45° inclined crack has the highest intensity of $\bar{K}_{II}$.

At 75° incidence, all three cracks again show similar trend of $\bar{K}_I$ at low frequencies, but at high frequencies, values of $\bar{K}_I$ diverge. Note that tip A and tip B of Y crack show considerably different results at high frequencies. All three cracks show similar trend of $\bar{K}_{II}$ increasing with frequency.

5.1.3 Rayleigh Wave

Figure 5.15 shows the normalized mode I ($\bar{K}_I$) and mode II ($\bar{K}_{II}$) stress intensity factors due to incident Rayleigh wave.

The responses due to Rayleigh waves are different from the responses due to P and SV waves. Both $\bar{K}_I$ and $\bar{K}_{II}$ fluctuate significantly with frequency producing distinct peaks and troughs. The peak magnitudes are lower than those generated by P and SV waves.

5.2 Surface Displacements

The surface displacements at any point on y = 0 can be calculated from Eq. (2.7), where the generalized coordinates {a} were determined from Eq. (2.28). In the following, we present results for the normalized values of the scattered displacement $u_y^{(s)}$.

The scattered surface displacements are normalized with respect to the amplitude of the free field $u^{(0)}$ at y = 0. The accuracy of the FEEET has already been tested in section 5.1 by comparing the stress-intensity factors and crack opening displacements with those results in Ref. [10]. We now test the accuracy of the FEEET to determine the surface displacements by comparison with analytical results obtained by the analytical method of Ref. [3] for the case where the scatterer is simply an embedded circular cavity. As shown in Fig. 5.16, results for P and SV agree well. Further confirmation of the accuracy of the FEEET is that the surface displacements calculated from Eq. (2.7) on the first and last boundary nodes are equal to those obtained from the finite element calculations.

In Figures 5.17 to 5.25, three different surface breaking cracks are considered: a vertical, a 45° inclined, and a vertical branched (Y) crack. For each type of crack, the normalized vertical scattered displacement at y = 0 is plotted versus the dimensionless distance x/D where D is the crack length. Five cases of incident wave are considered: P wave at 0° and 45° incidence, SV wave at 0° and 45° incidence, and Rayleigh wave. Four dimensionless frequencies, k_2D = 0.225, 0.9, 2.25, and 4.5 are considered. The

quantity NF is the normalization factor.

It can be seen that the surface displacements due to elastic waves scattered by the vertical crack are generally very similar to those scattered by the Y-crack. Therefore, detailed observation on the scattering effect of both of these cracks are made in section 5.2.1. On the other hand, the surface displacements scattered by the 45° inclined crack are completely different and observation on the scattering effect of this crack are made in section 5.2.2.

5.2.1 Surface Displacement Scattered by Vertical and Y Crack

Figures 5.17 to 5.19 and Figs. 5.20 to 5.22 show the normalized vertical surface displacements scattered by vertical and Y crack, respectively. For all incident fields, it can be seen that both cracks have a similar scattering effect.

For P wave at 0° incidence, the results are symmetrical about x = 0. The location of the maximum displacement depends on the frequency. Maximum displacement occurs at the vicinity of the crack mouth at low frequencies, and away from the crack mouth at higher frequencies. At 45° incidence, there is no symmetry of results, except at the very low frequency. There is generally a discontinuity in displacements across the crack mouth. Results at the illuminated side are generally larger.

For SV wave at 0° incidence, the results are symmetrical about x = 0 for all frequencies. Pronounced maximum displacement occurs at the vicinity of the crack mouth. It is noted that the highest frequency did not produce the largest displacement. At 45° incidence, results are symmetrical and maximum displacement occurs at the vicinity of the crack mouth at low frequencies. At high frequencies, distinct minima or maxima occur away from the crack mouth.

For Rayleigh wave, results are also symmetrical about x = 0 at the very low frequency, but not at higher frequencies. There is a discontinuity in displacements across the crack mouth. Maximum displacement occurs at the left (0^-) or right (0^+) side of the crack mouth depending on the frequency. Note that at $k_2D = 4.5$, a distinct minimum occurs at the illuminated side.

5.2.2 Surface Displacement Scattered by 45° Inclined Crack

Figures 5.23 to 5.25 show the normalized surface displacement scattered by a 45° inclined surface breaking crack. In all the figures, the displacements on the shadow side of the crack are much larger than that on the illuminated side. Hence, the 45° inclined crack has little scattering effect on the illuminated side of the crack.

For P wave at 0° incidence, maximum displacement occurs at 0^+ of the crack mouth and decreases as x/D decreases for all frequencies except at $k_2D = 4.5$ where local minima and maxima occur at $x/D > 0$. At 45° incidence, the scattering effect is almost similar to 0° incidence, but with different magnitudes.

For SV wave at 0° incidence, maximum displacements also occur at 0^+ of the crack mouth and decreases as x/D increases for all frequencies. At 45° incidence, maximum displacement also occurs at 0^+ of the crack mouth and decreases when x/D increases for all frequencies, except at $k_2D = 4.5$ where maximum displacement occurs at $x/D > 0$.

For Rayleigh wave, maximum displacement occurs at 0^+ of the crack mouth and decreases as x/D increases for all frequencies. It is noted that the largest displacement is not due to the highest frequency.

5.3 Conclusions

The mode I and mode II normalized stress intensity factors at the crack tips of three surface breaking cracks are presented. The variations of the

stress intensity factors depend on the frequency, the angle of incidence, and the nature of the incident waves. Nevertheless, the mode I normalized stress intensity factors are invariably larger than the mode II normalized stress intensity factors.

Under dynamic loading, it is important to know the elastodynamic response of the crack because a local stress concentration could result at the crack tip. The crack will propagate when the stresses reach a critical value. The stress intensity factors presented are a measure of the stress environment around the crack tips. The results provide the stress field around the crack tips to design against crack propagation.

The scattered surface displacement due to the vertical straight crack and the vertical Y crack are similar. On the other hand, the scattered surface displacement due to the 34° inclined crack is different from the vertical and Y crack in a distinct manner. Therefore, the orientation of the crack rather than the type of crack produces distinct results. The variation of the scattered surface displacements also depend on the frequency, the angle of incidence, and the nature of the incident waves.

In the field of quantitative non-destructive evaluation, the scattered surface displacements, it is hoped, provide data for solving the inverse problem of obtaining the crack geometry. The results presented are necessary prerequisites to the inverse problem.

REFERENCES

1. Graff, K.F., "Wave Motion in Elastic Solids", Oxford University Press. 1975.

2. Wong, K.C., "Diffraction of Plane Horizontally Polarized Shear (SH) Wave in Half Space", M.Sc. thesis, University of Manitoba, May, 1982.

3. Wong, K.C., "Elastic Wave Scattering by Arbitrarily-Shaped Inhomogeneities", Ph.D. Thesis, University of Manitoba, Feb., 1985.

4. Datta, S.K. and Shah, A.H., "Dynamic Response of Buried Pipelines and Tunnels", Earthquake Ground Motion and Its Effects on Structures, ASME, Vol. 53, S.K. Datta (ed.), 1982, pp. 181-197.

5. Datta, S.K. Wong, K.C. and Shah, A.H., "Dynamic Amplification of Stresses and Displacements Induced in a Buried Pipe in a Semi-Infinite Medium", Journal of Engineering Mechanics, ASCE, Vol. 110, No. 10, pp. 198-

6. Wong, K.C., Shah, A.H., and Datta, S.K., "Dynamic Amplification of Stresses and Displacements Induced in a Buried Tunnel", Journal of Engineering Mechanics, ASCE, Vol. 110, No. 2, Feb., 1985, pp. 218-234.

7. Wong, K.C., Shah, A.H., Datta, S.K. and O'Leary, P.M., "Dynamic Amplification of Displacements and Stresses Around Buried Pipelines and Tunnels", ASME, Vol. 60, New York, S.K. Datta (ed), 1984, pp. 147-162.

8. Shah, A.H., Wong, K.C., and Datta, S.K., "Dynamic Stress Intensity Factors for Buried Planar and Non-Planar Cracks", to appear in International Journal of Solids and Structures.

9. Shah, A.H., Wong, K.C., and Datta, S.K., "Surface Displacements due to Elastic Wave Scattering by Buried Planar and Non-Planar Cracks", Wave Motion, Vol. 7, No. 4, July, 1985, pp. 319-333.

10. Achenbach, J.D., Keer, L.M., and Mendelsohn, D.A., "Elastodynamic Analysis of an Edge Crack", Journal of Appl. Mech. 47, 1980, pp. 551-556.

11. Mendelsohn, D.A., Achenbach, J.D., and Keer, L.M., "Scattering of Elastic Waves by a Surface-Breaking Crack", Wave Motion, No. 2, 1980, pp. 277-292.

12. Hirao, M. and Fukuoka, H., "Scattering of Rayleigh Surface Wave by Edge Cracks: Numerical Simulation and Experiment", J. Acoust. Soc. Am., No. 2, Aug. 1982, pp. 602-606.

13. Visscher, W.M., "Elastic Wave Scattering by a Surface-Breaking or Subsurface Planar Crack", submitted to Wave Motion.

14. Stone, S.F., Ghosh, M.L., and Mal, A.K., "Diffraction of Antiplane Shear Waves by an Edge Crack", J. Appl. Mech., No. 47, 1980, pp. 359-362.

15. Datta, S.K., "Diffraction of SH Waves by an Edge Crack", J. Appl. Mech. No. 46, 1979, pp. 101-106.

16. Datta, S.K., "Scattering of Elastic Waves", Mechanics Today, 4, Pergamon Press, S. Nerrat-Nasser (ed.), 1978, pp. 149-204.

17. Shah, A.H., Wong, K.C., and Datta, S.K., "Single and Multiple Scattering of Elastic Waves in Two Dimensions", Journal of Acoustical Society of America, Vol. 74, No. 3, Sept., 1983, pp. 1037-1043.

18. Wong, K.C., Shah, A.H., and Datta, S.K., "Diffraction of Elastic Waves in a Half Space. II. Analytical and Numerical Solutions", Bulletin of Seismological Society of America, Vol. 75, No. 1, Feb. 1982, pp. 69-92.

19. Gregory, R.D., "An Expansion Theorem Applicable to Problems of Wave Propagation in an Elastic Half-Space Containing a Cavity", Proc. Camb. Phil. Soc. 63, 1967, pp. 1341-1367.

20. Abramowitz, M. and Stegun, I.A., "Handbook of Mathematical Functions", Dover Publications, Inc., New York, 1972, pp. 890-891.

21. Barsoum, R.S., "Triangular Quarter-Point Elements as Elastic and Perfectly-Plastic Crack Tip Elements", International Journal for Numerical Methods in Engineering, Vol. 11, pp. 85-98, 1977.

22. Lynn, P.P. and Ingraffea, A.R., "Transition Elements to be Used with Quarter Point Crack Tip Elements", Short Communications.

APPENDIX A

Derivation of the Potentials ϕ_n^p, ϕ_n^s, χ_n^p, and χ_n^s

Solutions to Eq. (2.3) for outgoing waves in an infinite medium are

$$\phi_n(r,\theta) = a_n H_n^{(1)}(k_1 r)e^{in\theta}$$
$$\chi_n(r,\theta) = b_n H_n^{(1)}(k_2 r)e^{in\theta} \qquad \text{(A-1)}$$

where $H_n^{(1)}$ is Hankel function of the first kind, r and θ are defined as shown in Fig. A1.

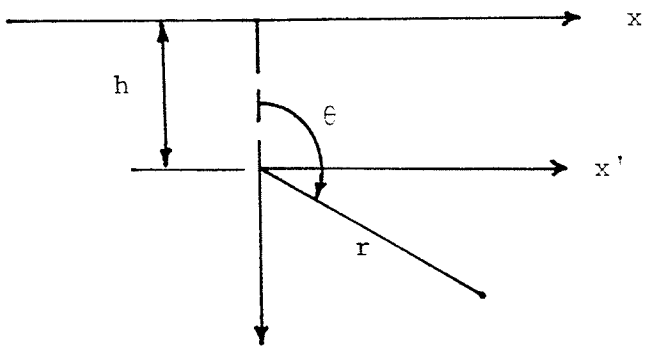

Fig. A1. Coordinate System

Note:

$$H_n^{(1)}(k_1 r)e^{in\theta} = \frac{i}{\pi}\int_{c_1} e^{k_1(h-y)\sinh s - ns + ik_1 x\cosh s}\, ds$$

Also, contour c_1 is such that (see Fig. A2)

$$\text{Re(real) } \sinh(s) \leq 0$$

$$\text{Im (imaginary) } \sinh(s) > 0$$

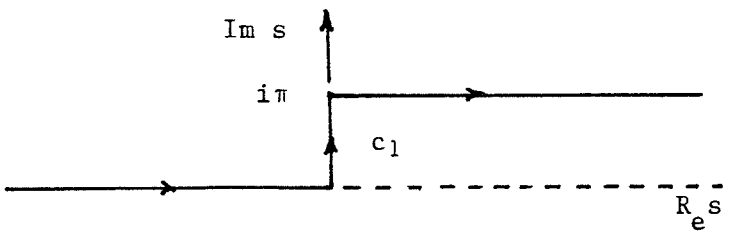

Fig. A2. Contour for s

Now, change $k_1\cosh s = k$ and $k_s \sinh s = -\sqrt{k^2 - k_1^2}$

then $dk = k_1 \sinh s\, ds$

$$ds = \frac{dk}{-\sqrt{k^2 - k_1^2}}$$

Also, $$e^{-ns} = (e^{-s})^n = (\cosh s - \sinh s)^n$$

$$= \left(\frac{k + \sqrt{k^2 - k_1^2}}{k_1}\right)^n$$

$$H_n^{(1)}(k,r)e^{in\theta} = -\frac{i}{\pi}\int_{-\infty}^{\infty} \frac{dk}{\sqrt{k^2 - k_1^2}}\, e^{ik\chi - \sqrt{k^2-k_1^2}\,(h-y)}\left(\frac{k + \sqrt{k^2-k_1^2}}{\alpha}\right)^n \tag{A-3}$$

but, $\phi_n = H_n^{(1)}(k_1 r)e^{in\theta}$

then

$$\phi_n = -\frac{i}{\pi}\left[\int_0^{\infty} \frac{dk}{\sqrt{k^2 - k_1^2}}\, e^{ikx - \sqrt{k^2-k_1^2}\,(h-y)}\left(\frac{k + \sqrt{k^2-k_1^2}}{k_1}\right)^n \right. \tag{A-4}$$

$$\left. + \int_0^{\infty} \frac{dk}{\sqrt{k^2 - k_1^2}}\, e^{ikx - \sqrt{k^2-k_1^2}\,(h-y)}\left(-\frac{k + \sqrt{k^2-k_1^2}}{k_1}\right)^n \right].$$

In order to find the reflection coefficients, it will be convenient to separate the two integrals of ϕ_n. Thus, we shall only consider the first term of ϕ_n, that is

$$\phi_n = -\frac{i}{\pi}\int_0^{\infty} \frac{dk}{\sqrt{k^2 - k_1^2}}\, e^{ikx - \sqrt{k^2-k_1^2}\,(h-y)}\left(\frac{k + \sqrt{k^2-k_1^2}}{k_1}\right)^n \tag{A-5}$$

Defining $\nu_1 = \sqrt{k^2 - k_1^2}$, $\nu_2 = \sqrt{k^2 - k_2^2}$

and $E(\nu_1,h,n) = e^{-\nu_1 h}\,\frac{1}{\nu_1}\left(\frac{k + \nu_1}{k_1}\right)^n$, we have

$$\phi_n = -\frac{i}{\pi}\int_0^{\infty} E\; e^{ikx + \nu_1 y}\, dk \tag{A-6}$$

The P wave will be reflected as P and SV wave. Thus,

$$\phi_n^P = \phi^{(i)} + \phi^{(r)} \tag{A-7}$$

$$\phi_n^P = -\frac{i}{\pi}\int_0^{\infty} E\, e^{ikx + \nu_1 y}\, dk - \frac{i}{\pi}\int_0^{\infty} EA\, e^{ikx - \nu_1 y}\, dk \tag{A-8}$$

$$\chi_n^p = \chi^{(r)} = -\frac{i}{\pi}\int_0^\infty EB\, e^{ikx - \nu_2 y}\, dk \qquad \text{(A-9)}$$

where A and B are constants to be evaluated from boundary conditions:

$$\sigma_{yy}\Big|_{y=0} = 0 \qquad \sigma_{xy}\Big|_{y=0} = 0\ . \qquad \text{(A-10)}$$

In the sequel, we will suppress $-\frac{i}{\pi}$, $\int$, and E, and write

$$\begin{aligned}\phi^{(i)} &= e^{ikx + \nu_1 k}\\ \phi^{(r)} &= A\, e^{ikx - \nu_1 k}\\ \chi^{(r)} &= B\, e^{ikx - \nu_2 y}\ .\end{aligned} \qquad \text{(A-11)}$$

To evaluate A and B

$$\begin{aligned}u_x &= \frac{\partial\phi}{\partial x}^{(i)} + \frac{\partial\phi}{\partial x}^{(r)} + \frac{\partial\chi}{\partial y}^{(r)}\\ &= ike^{ikx + \nu_1 y} + ikAe^{ikx - \nu_1 y} - \nu_2 Be^{ikx - \nu_2 y}\end{aligned} \qquad \text{(A-12)}$$

$$\begin{aligned}u_y &= \frac{\partial\phi}{\partial y}^{(i)} + \frac{\partial\phi}{\partial y}^{(r)} + \frac{\partial\chi}{\partial x}^{(r)}\\ &= \nu_1 e^{ikx + \nu_1 y} + \nu_1 Ae^{ikx - \nu_1 y} - ikBe^{ikx - \nu_2 y}\end{aligned}$$

$$\begin{aligned}\frac{\sigma_{yy}}{\mu} &= \left(\frac{\lambda + 2\mu}{\mu}\right)\frac{\partial u_y}{\partial y} + \frac{\lambda}{\mu}\frac{\partial u_x}{\partial x}\\ &= \{2[\nu_1^2 e^{\nu_1 y} + \nu_1^2 Ae^{-\nu_1 y} + ik\nu_2 Be^{-\nu_2 y}]\\ &\quad + (k_2^2 - 2k_1^2)\,[-(e^{\nu_1 y} + Ae^{-\nu_1 y})]\}e^{ikx}\end{aligned}$$

$$\frac{\sigma_{yy}}{\mu}\Big|_{y=0} = 0 \rightarrow (2k^2 - k_2^2)A + (2ik\nu_2)B + (2k^2 - k_2^2) = 0 \qquad \text{(A-13)}$$

$$\begin{aligned}\frac{\sigma_{xy}}{\mu} &= \frac{\partial u_x}{\partial y} + \frac{\partial u_y}{\partial x}\\ &= [ik\nu_1 e^{\nu_1 y} - ik\nu_1 Ae^{-\nu_1 y} + \nu_2^2 Be^{-\nu_2 y}\\ &\quad + ik\nu_1 e^{\nu_1 y} - ik\nu_1 Ae^{-\nu_1 y} + k^2 Be^{-\nu_2 y}]e^{ikx}\end{aligned}$$

$$\frac{\sigma_{xy}}{\mu}\Big|_{y=0} = 0 \rightarrow -2ik\nu_1 A + (2k^2 - k_2^2)B + 2ik\nu_1 = 0 \qquad \text{(A-14)}$$

solving Eqs. (A-13) and (A-14), we get

$$A = -\frac{1}{F(k)}\left[F(k) + 8k^2\nu_1\nu_2\right] \tag{A-15}$$

and $$B = \frac{1}{F(k)}\left[-4ik\nu_1(2k^2 - k_2{}^2)\right] \tag{A-16}$$

where $$F(k) = (2k^2 - k_2{}^2) - 4k^2\nu_1\nu_2 \ . \tag{A-17}$$

Thus,

$$\phi_n{}^p = -\frac{i}{\pi}\left\{\int_0^\infty \frac{e^{-\nu_1 h}}{\nu_1}\left(\frac{k + \sqrt{k^2-k_1{}^2}}{k_1}\right)^n e^{ikx + \nu_1 y}\, dk\right.$$

$$\left. - \int_0^\infty \left[1 + \frac{8k^2\nu_1\nu_2}{F(k)}\right] \frac{e^{-\nu_1 h}}{\nu_1}\left(\frac{k + \sqrt{k^2-k_1{}^2}}{k_1}\right)^n e^{ikx-\nu_1 y}\, dk\right\} \tag{A-18}$$

$$\chi_n{}^p = -\frac{4}{\pi}\int_0^\infty \frac{k(2k^2-k_2{}^2)}{F(k)}\, e^{-\nu_1 h}\left(\frac{k + \sqrt{k^2-k_1{}^2}}{k_1}\right)^n e^{ikx-\nu_2 y}\, dk \tag{A19}$$

Similarly,

$$\chi_n = b_n H_n{}^{(1)}(k_2 r)e^{in\theta} \tag{A-20}$$

suppressing b_n,

$$\chi_n = -\frac{i}{\pi}\int_0^\infty \frac{dk}{\sqrt{k^2-k_2{}^2}}\, e^{ikx+\nu_2 y}\, e^{-\nu_2 h}\left(\frac{k+\sqrt{k^2-k_2{}^2}}{k_2}\right)^n \tag{A-21}$$

Define

$$G(\nu_2,h,n) = \frac{e^{-\nu_2 h}}{\nu_2}\left(\frac{k+\nu_2}{k_2}\right)^n, \text{ then}$$

$$\chi_n = -\frac{i}{\pi}\int_0^\infty G\, e^{ikx+\nu_2 y}\, dk \ . \tag{A-22}$$

The SV-wave will be reflected as P and SV wave. Thus,

$$\phi_n{}^s = \phi^{(r)} = -\frac{i}{\pi}\int_0^\infty G\, e^{ikx+\nu_1 y}\, dk \tag{A-23}$$

$$\chi_n^s = \chi^{(i)} + \chi^{(r)} = -\frac{i}{\pi}\int_0^\infty G\, e^{ikx+\nu_2 y}\, dk - \frac{i}{\pi}\int_0^\infty GD\, e^{ikx-\nu_2 y}\, dk \qquad (A\text{-}24)$$

where C and D are constants to be evaluated from boundary conditions.

$$\sigma_{yy}\Big|_{y=0} = 0 \qquad \sigma_{xy}\Big|_{y=0} = 0 \ . \qquad (A\text{-}10)$$

In the sequel, we will suppress $-\frac{i}{\pi}$, $\int$ and F and write

$$\phi^{(r)} = Ce^{ikx-\nu_1 y}$$

$$\chi^{(i)} = e^{ikx-\nu_2 y} \qquad (A\text{-}25)$$

$$\chi^{(r)} = De^{ikx-\nu_2 y} \ .$$

To Evaluate C and D

$$u_x = \frac{\partial\phi^{(r)}}{\partial x} + \frac{\partial\chi^{(i)}}{\partial y} + \frac{\partial\chi^{(r)}}{\partial y}$$

$$= \{(ik)Ce^{-\nu_1 y} + \nu_2 e^{\nu_2 y} - \nu_2 De^{-\nu_2 y}\}\, e^{ikx} \qquad (A\text{-}26)$$

$$u_y = \frac{\partial\phi^{(r)}}{\partial y} - \frac{\partial\chi^{(i)}}{\partial x} - \frac{\partial\chi^{(r)}}{\partial x}$$

$$= \{-\nu_1 Ce^{-\nu_1 y} - ike^{\nu_2 y} - ikDe^{-\nu_2 y}\}\, e^{ikx}$$

$$\frac{\sigma_{yy}}{\mu} = \left(\frac{\lambda+2\mu}{\mu}\right)\frac{\partial u_y}{\partial y} + \frac{\lambda}{\mu}\frac{\partial u_x}{\partial x}$$

$$= \{(2k^2-k_2^2)\, Ce^{-\nu_1 y} + (2ik\nu_2)De^{-\nu_2 y} - 2ik\nu_2 e^{\nu_2 y}\}\, e^{ikx}$$

$$\frac{\sigma_{yy}}{\mu}\Big|_{y=0} = 0 \ \rightarrow \ (2k^2 - k_2^2)\, C + (2ik\nu_2)\, D - 2ik\nu_2 = 0 \qquad (A\text{-}27)$$

$$\frac{\sigma_{xy}}{\mu} = \frac{\partial u_x}{\partial y} + \frac{\partial u_y}{\partial y}$$

$$= \{(-2ik\nu_1)\, Ce^{-\nu_1 y} + (2k^2 - k_2^2)\, De^{-\nu_2 y} + (2k^2-k_2^2)e^{\nu_2 y}\}e^{ikx}$$

$$\frac{\sigma_{xy}}{\mu}\Big|_{y=0} = 0 \ \rightarrow \ (-2ik\nu_1)C + (2k^2-k_2^2)D + (2k^2 - k_2^2) = 0 \ . \qquad (A\text{-}28)$$

Solving Eqs. (A-27) and (A-28), we get

$$C = \frac{1}{F(k)} [4ik\nu_2(2k^2 - k_2^2)] \tag{A-29}$$

$$D = \frac{-1}{F(k)} [F(k) + 8 k^2\nu_1\nu_2] \tag{A-30}$$

where $F(k) = (2k^2 - k_2^2)^2 - 4k^2\nu_1\nu_2$

Thus,

$$\phi_n^s = \frac{4}{\pi} \int_0^\infty e^{-\nu_2 h} \left(\frac{k + \nu_2}{k_2}\right)^n k \frac{(2k^2 - k_2^2)}{F(k)} \quad e^{ikx-\nu_1 y} \, dk \tag{A-31}$$

$$\chi_n^s = \frac{-i}{\pi} \{ \int_0^\infty \frac{e^{-\nu_2 h}}{\nu_2} \left(\frac{k + \nu_2}{k_2}\right)^n e^{ikx + \nu_2 y} \, dk$$

$$- \int_0^\infty \frac{e^{-\nu_2 h}}{\nu_2} \left(\frac{k + \nu_2}{k_2}\right)^n [1 + \frac{8k^2\nu_1\nu_2}{F(k)}] \, e^{ikx-\nu_2 y} \, dk \} . \tag{A-32}$$

These integrands will be from $\int_{-\infty}^{\infty}$ when we take the other term.

Rewriting Eqs. (A-18), (A-19), (A-31), and (A-32), we have:

$$\phi_n^p = H_n^{(1)}(k_1 r) e^{in\theta}$$

$$+ \frac{i}{\pi} \int_{-\infty}^{\infty} [1 + \frac{8k^2\nu_1\nu_2}{F(k)}] \frac{e^{-\nu_1 h}}{\nu_1} \left(\frac{k + \nu_1}{k_1}\right)^n e^{ikx-\nu_1 y} \, dk$$

$$\chi_n^p = - \frac{4}{\pi} \int_{-\infty}^{\infty} \frac{k(2k^2-k_2^2)}{F(k)} e^{-\nu_1 h} \left(\frac{k + \nu_1}{k_1}\right)^n e^{ikx-\nu_2 y} \, dk \tag{A-33}$$

$$\phi_n^s = \frac{4}{\pi} \int_{-\infty}^{\infty} e^{-\nu_2 h} \frac{k(2k^2-k_2^2)}{F(k)} \left(\frac{k + \nu_2}{k_2}\right)^n e^{ikx-\nu_1 y} \, dk \tag{A-34}$$

$$\chi_n^s = H_n^{(1)}(k_2 r) e^{in\theta}$$

$$+ \frac{i}{\pi} \int_{-\infty}^{\infty} [1 + \frac{8k^2\nu_1\nu_2}{F(k)}] \frac{e^{-\nu_2 h}}{\nu_2} \left(\frac{k + \nu_2}{k_2}\right)^n e^{ikx} \qquad dk$$

where $k_1 = \sqrt{\omega^2/c_1^2}$ and $k_2 = \sqrt{\omega^2/c_1^2}$

$c_1 = \sqrt{(\lambda + 2\mu)/\rho}$ and $c_2 = \sqrt{\mu/\rho}$.

k_1 and k_2 are the shear and pressure wave numbers. c_1 and c_2 are the shear and pressure wave speeds. μ and λ are Lamb's constants, and ρ is the mass density.

$$\nu_1 = \sqrt{k^2 - k_1^2} \text{ and } \nu_2 = \sqrt{k^2 - k_2^2}$$

$\bar{F}(k) = (2k^2 - k_2^2)^2 - 4k^2\nu_1\nu_2$ is the Rayleigh wave frequency equation.

APPENDIX B

Incident and Reflected Field

Incident P Wave

Consider a plane P wave moving in a direction making an angle γ with the y-axis as shown in Fig. B1.

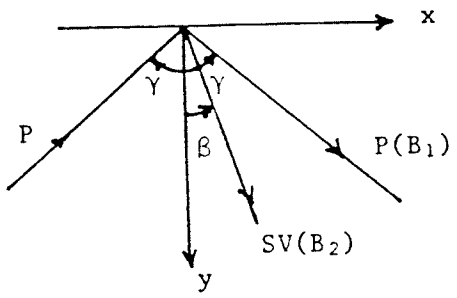

Fig. B1. Incident P wave.

Then $u^{(i)} = \nabla\phi^{(i)}$ (B-1)

where $\phi^{(i)} = \phi_0 e^{ik_1(x \sin\gamma - y \cos\gamma)}$

This field will be reflected into a P and SV wave such that

$$u^{(r)} = \nabla\phi^{(r)} + \nabla\times\chi^{(r)} \quad \text{(B-2)}$$

where $\phi^{(r)} = B_1 e^{ik_1(x \sin\gamma + y \cos\gamma)}$ (B-3)

$$\chi^{(r)} = B_2 e^{ik_2(x \sin\beta + y \cos\beta)} \quad \text{(B-4)}$$

and $$B_1 = \phi_0 \frac{\sin 2\gamma \sin 2\beta - \tau^2 \cos^2\beta}{\sin 2\gamma \sin 2\beta + \tau^2 \cos^2 2\beta} \quad \text{(B-6)}$$

$$B_2 = \phi_0 \frac{2 \sin 2\gamma \sin 2\beta}{\sin 2\gamma \sin 2\beta + \tau^2 \cos^2 2\beta}$$

We have $\sin\beta = \frac{1}{\tau} \sin\gamma$

and $\tau = \frac{k_2}{k_1}$

where k_1 and k_2 are the pressure and shear wave number, respectively. ϕ_0 is taken as 1.

With $u_j^{(0)} = u_j^{(i)} + u_j^{(r)}$ $(j = 1,2)$

$$u_x^{(0)} = ik_1 \sin\gamma\ (E_1 + B_2E_2) + B_2\, ik_2 \cos\beta\ E_3 \qquad \text{(B-7)}$$

$$u_y^{(0)} = ik_1\gamma\ (-E_1 + B_1E_2) - B_2ik_2 \sin\beta\ E_3 \ .$$

By employing the strain-displacement and stress-strain relationship, the three components of stresses can be written as,

$$\frac{\sigma_{xx}^{(0)}}{\mu} = k_1^2[2\cos^2\gamma - \tau^2]\ (E_1 + B_1E_2) - B_2k_2^2\sin2\beta\ E_3 \qquad \text{(B-8)}$$

$$\frac{\sigma_{yy}^{(0)}}{\mu} = k_1^2[2\sin^2\gamma - \tau^2]\ (E_1 + B_1E_2) - B_2k_2^2\sin2\beta\ E_3$$

$$\frac{\sigma_{xy}^{(0)}}{\mu} = k_1^2\ \sin2\gamma\ (E_1 - B_1E_2) - B_2k_2^2\cos2\beta\ E_3$$

where $E_1 = e^{ik_1(x\sin\gamma - y\cos\gamma)}$

$E_2 = e^{ik_1(x\sin\gamma + y\cos\gamma)}$

$E_3 = e^{ik_2(x\sin\beta + y\cos\gamma)}$.

Incident SV Wave

For a plane SV wave moving in a direction making an angle β with the y-axis as shown in Fig. B2.

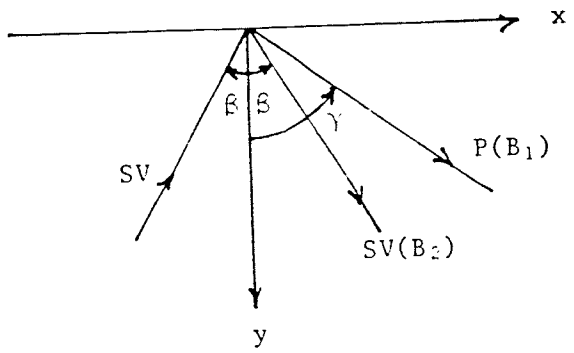

Fig. B2. Incident SV wave

Then $u^{(i)} = \Delta\times\chi^{(i)}$ (B-9)

where $\chi^{(i)} = \chi_0 e^{ik_2(x\sin\beta - y\cos\beta)}$.

The reflected field is given by Eq. (B-2) as

$$u^{(r)} = \nabla\phi^{(r)} + \nabla\times\chi^{(r)} \qquad \text{(B-10)}$$

where $\phi^{(r)} = B_1 e^{ik_1(x\sin\gamma + y\cos\gamma)}$ (B-11)

and $\chi^{(r)} = B_2 e^{ik_2(x\sin\beta + y\cos\beta)}$ (B-12)

If $\beta < \beta_{cr}$ where $\beta_{cr} = \sin^{-1}(1/\tau)$

$$B_1 = \chi_0 \frac{-2\tau^2\sin2\beta\cos2\beta}{\sin2\gamma\sin2\beta + \tau^2\cos^2 2\beta} \quad \text{(B-13)}$$

$$B_2 = \chi_0 \frac{\sin2\beta\sin2\gamma - \tau^2\cos^2 2\beta}{\sin2\alpha\sin2\beta + \tau^2\cos^2 2\beta} .$$

If $\beta > \beta_{cr}$, then

$$\phi^{(r)} = \bar{B}_1 e^{ik_2 x\sin\beta - \bar{\alpha}y} \quad \text{(B-14)}$$

$$\chi^{(r)} = \bar{B}_2 e^{ik_2(x\sin\beta + y\cos\beta)}$$

where $\bar{B}_1 = \chi_0 \frac{-2\sin2\beta\cos2\beta}{2i\bar{\beta}\sin\beta\sin2\beta + \cos^2 2\beta}$ (B-15)

$$\bar{B}_2 = \chi_0 \frac{-2i\bar{\beta}\sin2\beta\sin\beta - \cos^2 2\beta}{2i\bar{\beta}\sin\beta\sin2\beta + \cos^2 2\beta} .$$

$\bar{\beta} = \sqrt{\sin^2\beta - 1/\tau^2}$ and $\bar{\alpha} = k_2\bar{\beta}$. χ_0 is taken as unity.

For $\beta < \beta_{cr}$, the free displacement and stress fields can be written as:

$$u_x^{(0)} = ik_2\cos\beta(-E_4 + B_2E_3) + B_1ik_1\cos\gamma E_2 \quad \text{(B-16)}$$

$$u_y^{(0)} = -ik_2\sin\beta(E_4 + B_2E_3) + B_1ik_1\cos\gamma E_2$$

$$\frac{\sigma_x^{(0)}}{\mu} = k_2^2\sin2\beta(E_4 - B_2E_3) + B_1k_1^2(2\cos^2\gamma - \tau^2)E_2$$

$$\frac{\sigma_y^{(0)}}{\mu} = k_2^2\sin2\beta(-E_4 + B_2E_3) + B_1k_1^2(2\sin^2\gamma - \tau^2)E_2 \quad \text{(B-17)}$$

$$\frac{\sigma_{xy}^{(0)}}{\mu} = -k_2^2\cos2\beta(E_4 + B_2E_3) - B_1k_1^2\sin2\gamma\, E_2$$

where $E_4 = e^{ik_2(x\sin\beta - y\cos\beta)}$ and E_1, E_2 and E_3 are defined earlier.

For $\beta > \beta_{cr}$

$$u_x^{(0)} = ik_2\cos\beta(-E_4 + B_2E_3) + B_1ik_2\sin\beta E_5 \quad \text{(B-18)}$$

$$u_y^{(0)} = -ik_2\sin\beta(E_4 + B_2E_3) - B_1\bar{\alpha}E_5$$

$$\frac{\sigma_x^{(0)}}{\mu} = k_2^2\sin2\beta(E_4 - B_2E_3) + B_1(-k_2^2 - 2\bar{\alpha}^2)E_5$$

$$\frac{\sigma_y^{(0)}}{\mu} = k_2^2\sin2\beta(-E_4 + B_2E_3) - B_1k_2^2\cos2\beta\, E_5 \quad \text{(B-19)}$$

$$\frac{\sigma_{xy}^{(0)}}{\mu} = -k_2^2 \cos 2\beta (E_4 + B_2 E_3) - B_1 2i\alpha \bar{k}_2 \sin\beta \, E_5$$

where $E_5 = e^{ik_2 x \sin\beta - \bar{\alpha} y}$.

Incident Rayleigh Wave

For a Rayleigh wave moving in the positive x direction, we can show that

$$u_x^{(0)} = u_x^{(i)} = B_1 ik_R E_6 - B_2 \bar{\beta}_1 E_7 \qquad \text{(B-20)}$$

$$u_y^{(0)} = u_y^{(i)} = -B_1 \bar{\alpha}_1 E_6 - B_2 ik_R E_7$$

$$\frac{\sigma_x^{(0)}}{\mu} = \frac{\sigma_x^{(i)}}{\mu} = B_1(\bar{\beta}_1^2 - k_R^2 - 2\bar{\alpha}_1^2)E_6 - B_2 2ik_R \bar{\beta}_1 E_7$$

$$\frac{\sigma_y^{(0)}}{\mu} = \frac{\sigma_y^{(i)}}{\mu} = B_1(\bar{\beta}_1^2 + k_R^2)E_6 + B_2 2ik_R \bar{\beta}_1 E_7 \qquad \text{(B-21)}$$

$$\frac{\sigma_{xy}^{(0)}}{\mu} = \frac{\sigma_{xy}^{(i)}}{\mu} = -B_1 2ik_R \bar{\alpha}_1 E_6 + B_2(\bar{\beta}_1^2 + k_R^2)E_7$$

where $E_6 = e^{ik_R x - \bar{\alpha}_1 y}$

$E_7 = e^{ik_R x - \bar{\beta}_1 y}$

and $\bar{\alpha}_1 = \sqrt{k_R^2 - k_1^2}$

$\bar{\beta}_1 = \sqrt{k_R^2 - k_2^2}$

where $k_R = \frac{\omega}{C_R}$, C_R is the Rayleigh wave speed, and ω is the circular frequency

and $$\frac{B_1}{B_2} = \frac{\bar{\beta}_1^2 + k_R^2}{2ik_R \bar{\alpha}_1} = \frac{2k_R^2 - k_2^2}{2ik_R \sqrt{k_R^2 - k_1^2}}$$

APPENDIX C

Formulation of Matrixes [G] and [F]

As mentioned in chapter 2, the scattered nodal displacement vector, $\{q_B^{(s)}\}$, was formed by evaluating $u_x^{(s)}$; and $u_y^{(s)}$ in Eqn. (2.7a) at NB number of points on contour B. Thus, we have in Eqn. (2.9):

$$\{q_B^{(s)}\} = [G]\ \{a\} \tag{C-1}$$

where,

$$\{q_B^{(s)}\} = \{u_{xB_1}, \ldots, u_{xB_{NB}}; u_{yB_1}, \ldots, u_{yB_{NB}}\}^T \tag{C-2}$$

$$\{a\} = \{a_1, \ldots, a_{NB}; b_1, \ldots, b_{NB}\}^T \tag{C-3}$$

If [G] is partitioned as,

$$\begin{bmatrix} GXA & GXB \\ GYA & GYB \end{bmatrix}_{2NBx2NB} \tag{C-4}$$

then each of the NBxNB submatrix can be evaluated from Eqn. (2.7) at (x_i, y_i) on B as

$$\begin{aligned} (GXA)_{in} &= (\phi^P_{n,x} + \chi^P_{n,y}) \\ (GXB)_{in} &= (\phi^S_{n,x} + \chi^S_{n,y}) \\ (GYA)_{in} &= (\phi^P_{n,y} - \chi^P_{n,x}) \\ (GYB)_{in} &= (\phi^S_{n,y} - \chi^S_{n,x}) \quad , i = 1 \text{ to } NB \end{aligned} \tag{C-5}$$

The parameter n in the summation series of Eqn. (2.7) is taken from (-NB/2 - 1) to NB/2 for numerical purposes. Hence, n in the first column to the last column of each submatrix corresponds to (-NB/2 - 1) to NB/2, respectively.

To formulate the matrix [F], consider the stress components, σ_{xx}, σ_{yy}, and σ_{xy} at any point of a body represented by an infinitesimal element as shown in Fig. C1.

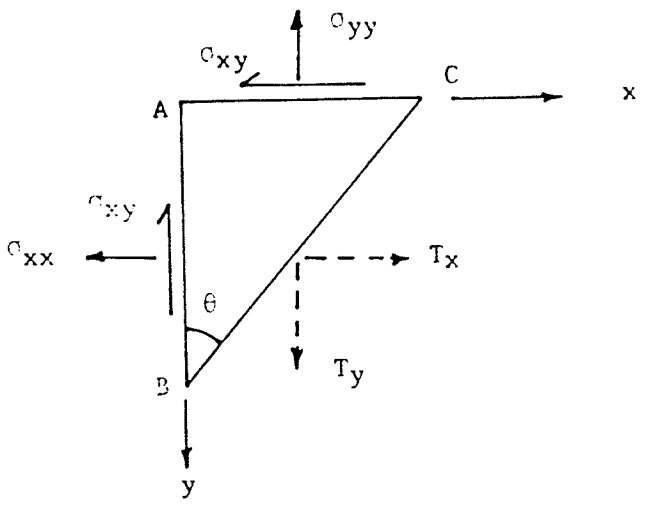

Fig. C1. Stress components σ_{xx}, σ_{yy}, and σ_{xy} in an infinitesimal element.

Sides AB and AC have an area of $\cos\theta$ and $\sin\theta$, respectively when the area of side BC is taken as unity. Equilibrium of forces in the x and y directions require that

$$T_x = \sigma_{xx}\cos\theta + \sigma_{xy}\sin\theta \qquad (C\text{-}6)$$

$$T_y = \sigma_{xy}\cos\theta + \sigma_{yy}\sin\theta$$

where T_x and T_y are the components of stress resultant acting on BC in the x and y directions, respectively.

Evaluating $\sigma_{xx}^{(s)}$, $\sigma_{yy}^{(s)}$, and $\sigma_{xy}^{(s)}$ from Eqn. (2.7b) at NB number of points on contour B and substituting in Eqn. (C-6), we have the scattered nodal stress vector, $\{\sigma_B^{(s)}\}$, as in Eqn. (2-10),

$$\{\sigma_B^{(s)}\} = [F]\{a\} \qquad (C\text{-}7)$$

where

$$\{\sigma_B^{(s)}\} = \{T_{xB_1}, \ldots, T_{yB_{NB}}; T_{yB_1}, \ldots, T_{yB_{NB}}\} \qquad (C\text{-}8)$$

and $\{a\}$ is defined in Eqn. (C-3)

[F] is partioned as

$$\begin{bmatrix} FXA & FXB \\ FYA & FYB \end{bmatrix}_{2NBx2NB}$$

Each of the NBxNB submatrix can be evaluated from Eqn. (2.8) and Eqn. (C-6) at (x_i, y_i) on B as,

$$(FXA)_{in} = [(\lambda + 2\mu)(\phi^P_{n,xx} + \chi^P_{n,xy}) + \lambda(\phi^P_{n,yy} - \chi^P_{n,xy})] \cos\theta + \mu(2\phi^P_{n,xy} + \chi^P_{n,yy} - \chi^P_{n,xx}) \sin\theta$$

$$(FXB)_{in} = [(\lambda + 2\mu)(\phi^S_{n,xx} + \chi^S_{n,xy}) + \lambda(\phi^S_{n,yy} - \chi^S_{n,xy})] \cos\theta + \mu(2\phi^S_{n,xy} + \chi^S_{n,yy} - \chi^S_{n,xx}) \sin\theta$$

$$(FYA)_{in} = \mu(2\phi^P_{n,xy} + \chi^P_{n,yy} - \chi^P_{n,xx}) \cos\theta + [(\lambda + 2\mu)(\phi^P_{n,yy} - \chi^P_{n,xy}) + \lambda(\phi^P_{n,xx} + \chi^P_{n,xy})]\sin\theta$$

$$(FYB)_{in} = \mu(2\phi^S_{n,xy} + \chi^S_{n,yy} - \chi^S_{n,xx}) \cos\theta + [(\lambda + 2\mu)(\phi^S_{n,yy} - \chi^S_{n,xy}) + \lambda(\phi^S_{n,xx} + \chi^S_{n,xy})]\sin\theta$$

Parameter n ranges from -(NB/2 - 1) to NB/2 as discussed before, and i = 1 to NB.

APPENDIX D STRESS INTENSITY FACTORS

Classical solution for the stress and displacement field around a crack tip are well known. There is a singularity in the stress field and the stresses along any radial line from the tip of the crack are all proportional to $Kr^{-1/2}$ where K is known as the stress intensity factor. There is a value of K corresponding to each of the characteristic loading modes.

K_I - crack opening mode

K_{II} - shearing mode

K_{III} - twisting mode

It is of considerable importance in many engineering situations to know the numerical value of the stress intensity factors since there are critical values of K which determine whether or not the crack will propagate.

In this thesis, the stress intensity factors K_I and K_{II} are calculated from the crack opening displacement (C.O.D.) near a crack tip by the relations.

$$\begin{bmatrix} K_I \\ K_{II} \end{bmatrix} = \frac{\mu}{2(1-\nu)} \begin{bmatrix} \bar{K}_I \\ \bar{K}_{II} \end{bmatrix}$$

where

$$\begin{bmatrix} \bar{K}_I \\ \bar{K}_{II} \end{bmatrix} = \tfrac{1}{2} (1/L)^{\frac{1}{2}} \begin{bmatrix} \Delta_1 \\ \Delta_2 \end{bmatrix}$$

$$\Delta_1 = 4(U_6 - U_4) - (U_3 - U_2)$$

and

$$\Delta_2 = 4(V_6 - V_4) - (V_3 - V_2)$$

In the above equation Vi and Ui represent the displacement components Uy and Ux, respectively, at the i-th node. The nodes 2,3 4 and 6 along with L are defined in the following figure.

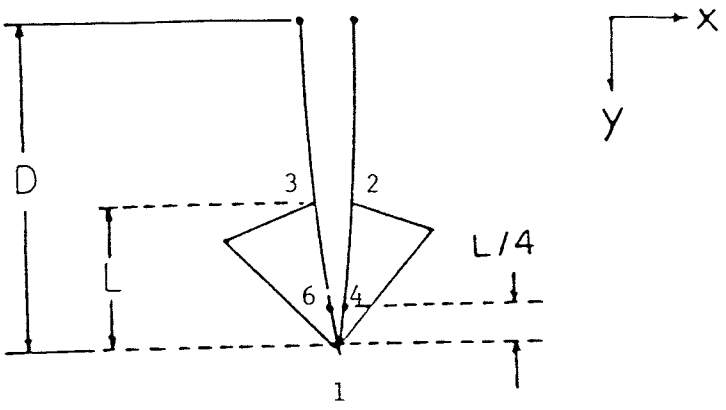

Fig. D1. Crack tip.

CRACK TIP ELEMENT AND TRANSITION ELEMENT

In [21], the use of quadratic isoparamatric elements has been shown to provide an excellent crack tip element when the mid-side node closest to the crack are put at the quarter point. The element has been shown to contain $1/r^{1/2}$ order of singularity, thus providing a stress field which agrees with the theoretical stress singularity of linear fracture mechanics. It has also been shown that the element

contains rigid body motion and constant strain modes, thus satisfying the necessary conditions for convergence. In addition, they satisfy the patch test.

A six-noded triangle with mid-side nodes at the quarter points is generated by collapsing the 1-4 of the quadrilateral in the following figure.

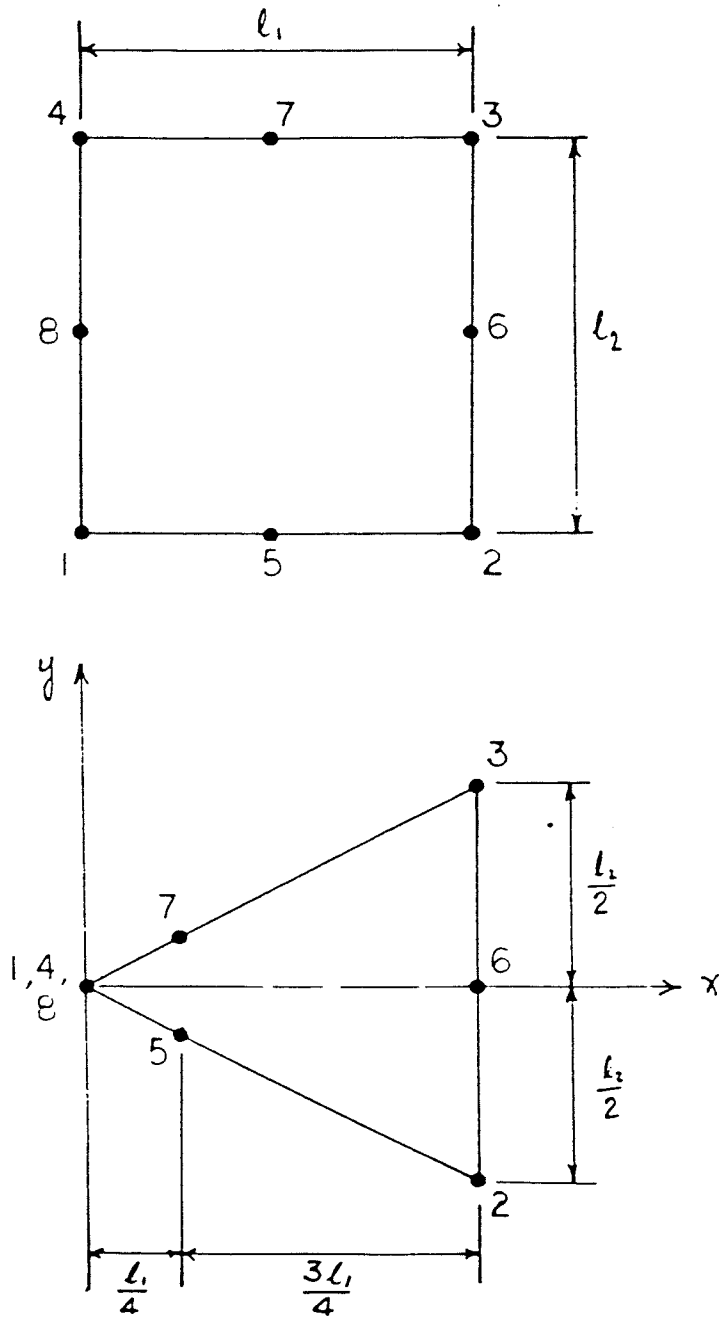

For the six-node and seven node elements the shape functions are expressed in terms of the local (ξ,η) coordinates as follows.

6-node singular element:

$L_1 = 0.5\ \xi(\xi-1)$

$L_2 = 0.25\ (1+\xi)\ (1-\xi)\ (\xi-\eta-1)$

$L_3 = 0.25\ (1+\xi)\ (1+\eta)\ (\xi+\eta-1)$

$L_4 = 0.5\ (1-\xi^2)\ (1-\eta)$

$L_5 = 0.5\ (1+\xi)\ (1-\eta^2)$

$L_6 = 0.5\ (1-\xi^2)\ (1+\eta)$

7-node transition element:

$L_1 = -0.25\ \xi\ (1-\xi)\ (1-\eta)$

$L_2 = 0.25\ (1+\xi)\ (1-\xi)\ (\xi-\eta-1)$

$L_3 = 0.25\ (1+\xi)\ (1+\eta)\ (\xi+\eta-1)$

$L_4 = -0.25\ \xi\ (1-\xi)\ (1+\eta)$

$L_5 = 0.5\ (1-\xi^2)\ (1-\eta)$

$L_6 = 0.5\ (1+\xi)\ (1-\eta^2)$

$L_7 = 0.5\ (1-\xi^2)\ (1+\eta)$

Furthermore, it is shown in [22] that by using eight noded quadrilateral isoparametric elements with appropriately placed side-nodes as transition elements between the quarter-point crack tip triangular and remaining non-singular elements, stress intensity factors are computed with higher accuracy.

SHAPE FUNCTIONS FOR SPECIAL ELEMENTS

The shape functions corresponding to the 6-node crack-tip singular elements and 7-node transition elements are given here for easy reference. The geometries of the elements are shown below.

6-NODE CRACK-TIP SINGULAR ELEMENT

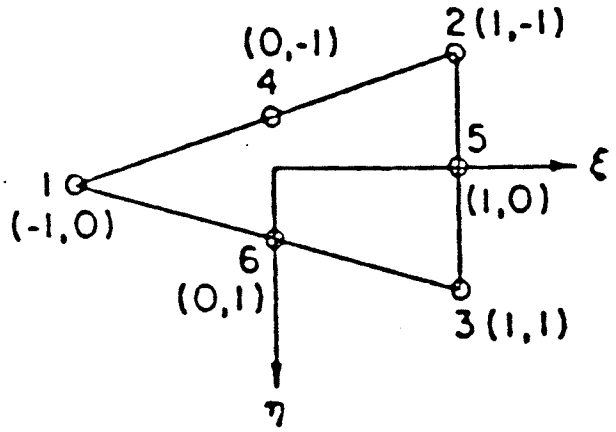

7-NODE TRANSITION ELEMENT

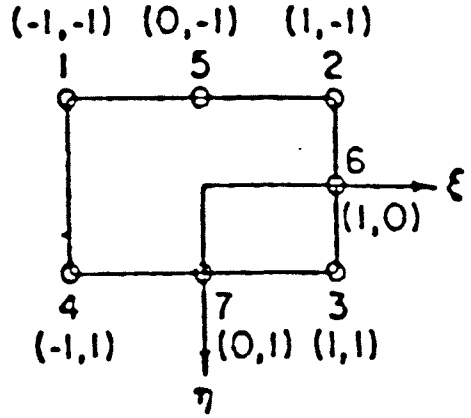

Table 1. The root of a complex number evaluated by the Fortran statement CDSQRT.

	x + iy	CDSQRT (x + iy)
+ve real	4.0 + i 0.0	2.0 + i 0.0
1st quad.	4.0 + i 3.0	2.121 + i 0.707
+ve imag.	0.0 + i 3.0	1.225 + i 1.22
2nd quad.	-4.0 + i 3.0	0.707 + i 2.121
-ve real	-4.0 + i 0.0	0.0 + i 2.0
3rd quad.	-4.0 - i 3.0	0.707 - i 2.121
-ve imag.	0.0 - i 3.0	1.225 - i 1.225
4th quad.	4.0 - i 3.0	2.121 - i 0.707

Table 2. Comparison of $Hn\ (k_1 r)\ e^{in\theta}$

n	IMSL Subroutine	Numerical Scheme
-11	$-0.33032 \times 10^2 + i\ 0.80879 \times 10^2$	$-0.33173 \times 10^2 + i\ 0.80960 \times 10^2$
-8	$-0.14795 \times 10^1 + i\ 0.22849 \times 10^1$	$-0.1478 \times 10^1 + i\ 0.2283 \times 10^1$
-4	$-0.65505 \times 10^{-1} + 0.42824$	$-0.65494 \times 10^{-1} + 0.42824$
0	$-0.16734 - i\ 0.31296$	$-0.16733 - i\ 0.31297$
4	$-0.28546 - i\ 0.32588$	$-0.28546 - i\ 0.32589$
8	$0.14472 \times 10^1 + i\ 0.23055 \times 10^1$	$0.144716 \times 10^1 + i\ 0.23051 \times 10^1$
12	$0.23601 \times 10^3 - i\ 0.26942 \times 10^3$	$0.23606 \times 10^3 - i\ 0.26976 \times 10^3$

NOTE: $k_1 = 1.5$

$r = \sqrt{x^2 + y^2} = \sqrt{3^2 + 0^2} = 9$

$\theta = 1.107$ rad.

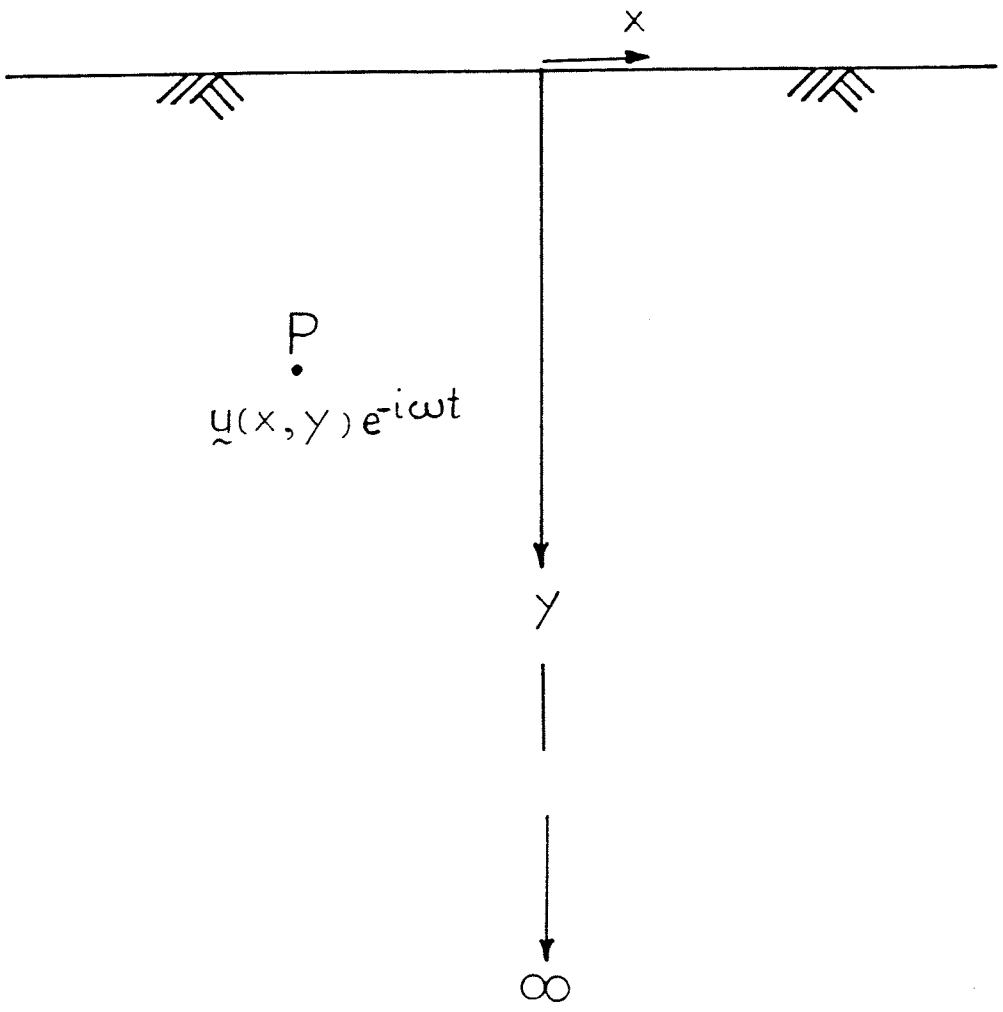

Fig.2.1 - Semi-Infinite Medium

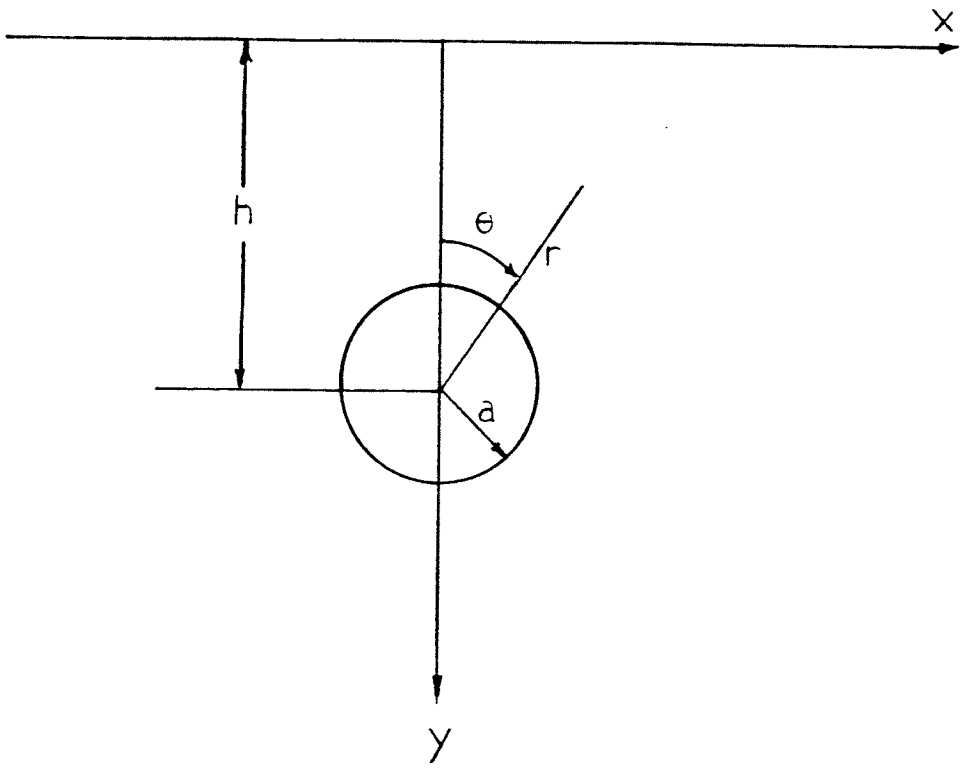

Fig.2.2 - Circular Cavity In a Semi-Infinite Medium

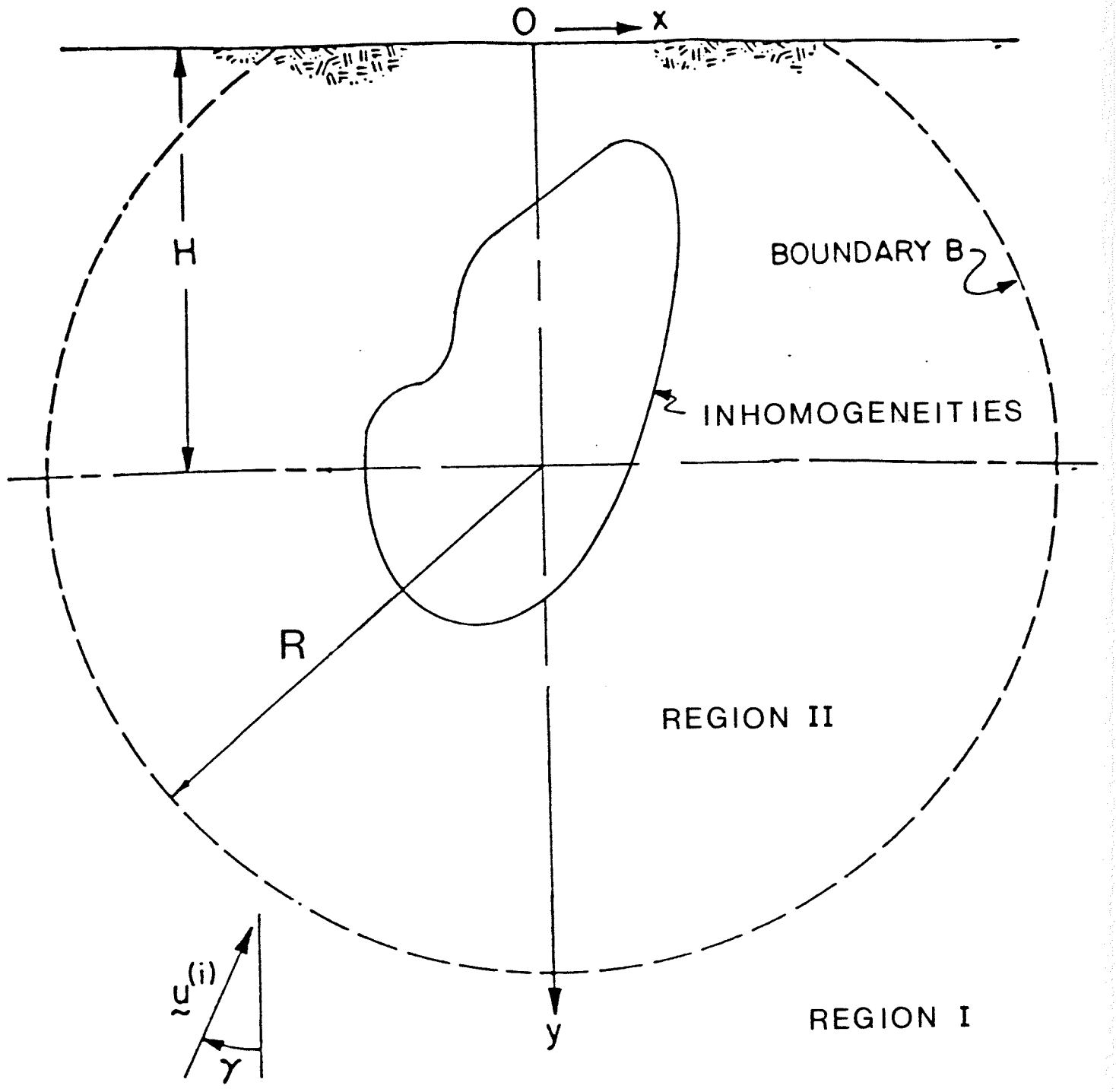

Fig.2.3 _ Plane Strain Motion of Inhomogeneities Embedded In a Semi-Infinite Medium

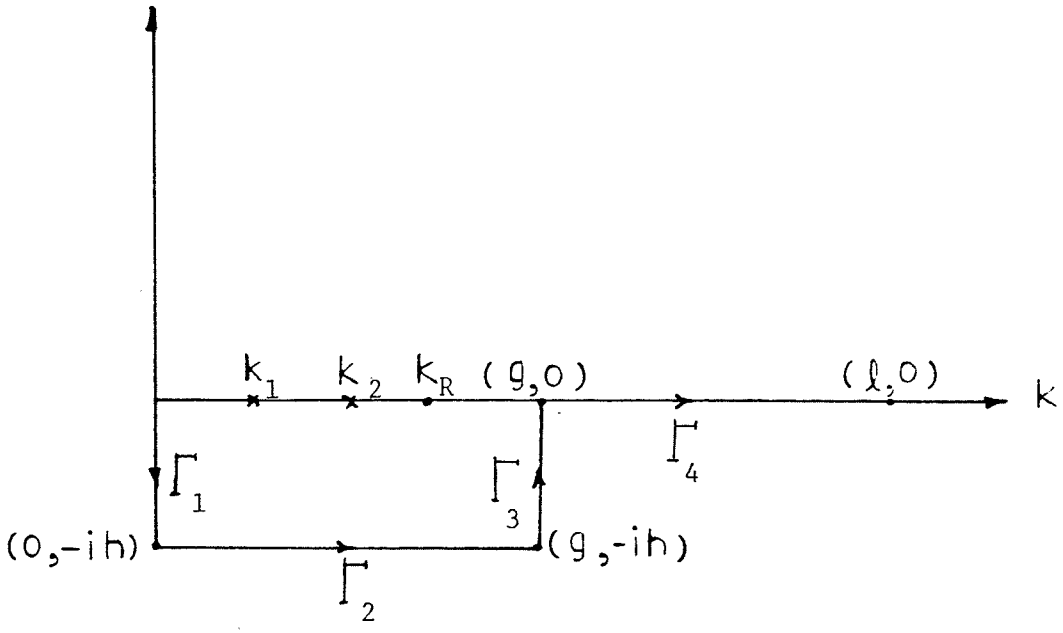

Fig.3.1 - Integration Contour

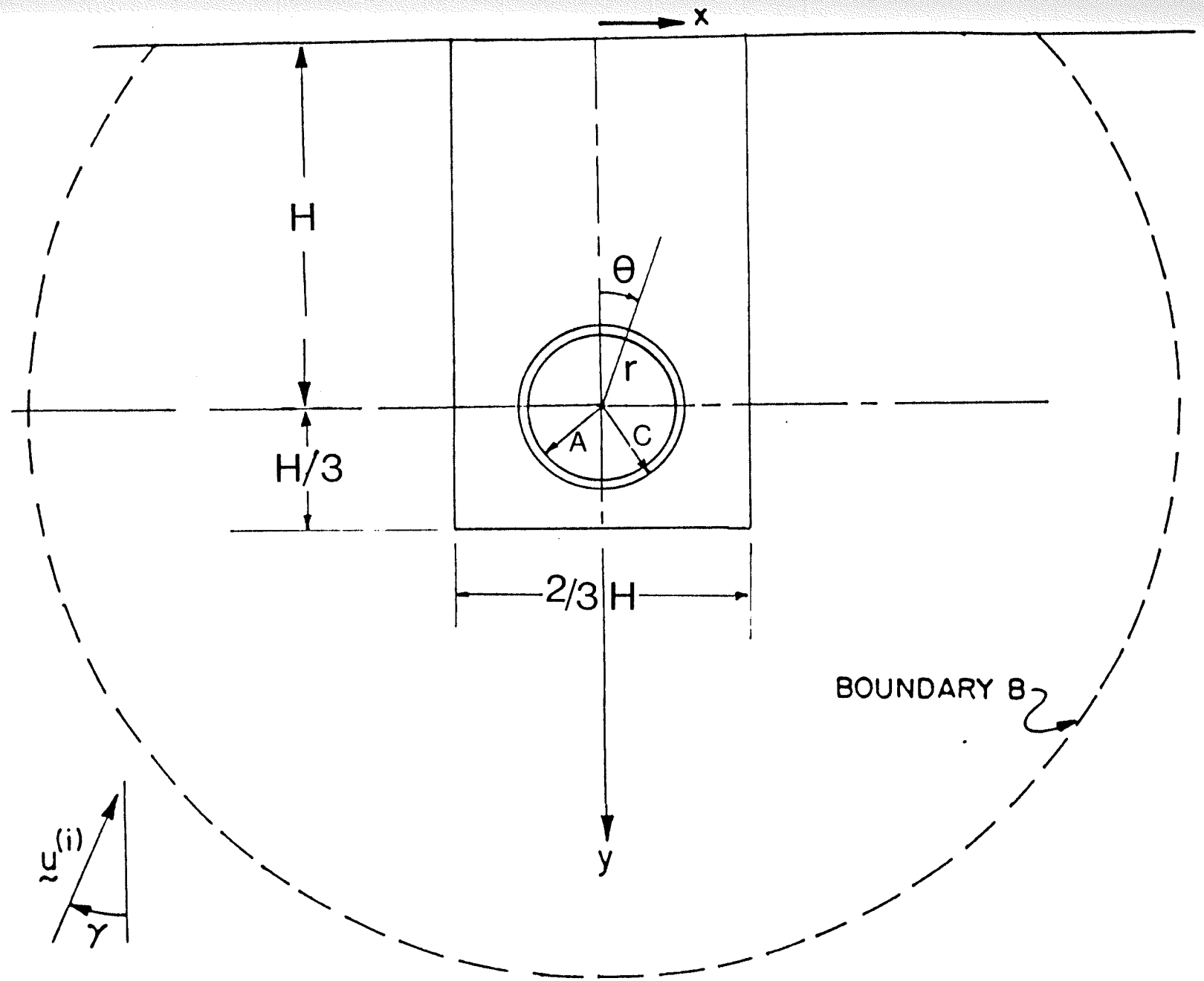

Fig.4.1 - Geometry of a Single Pipe In a Rectangular Trench

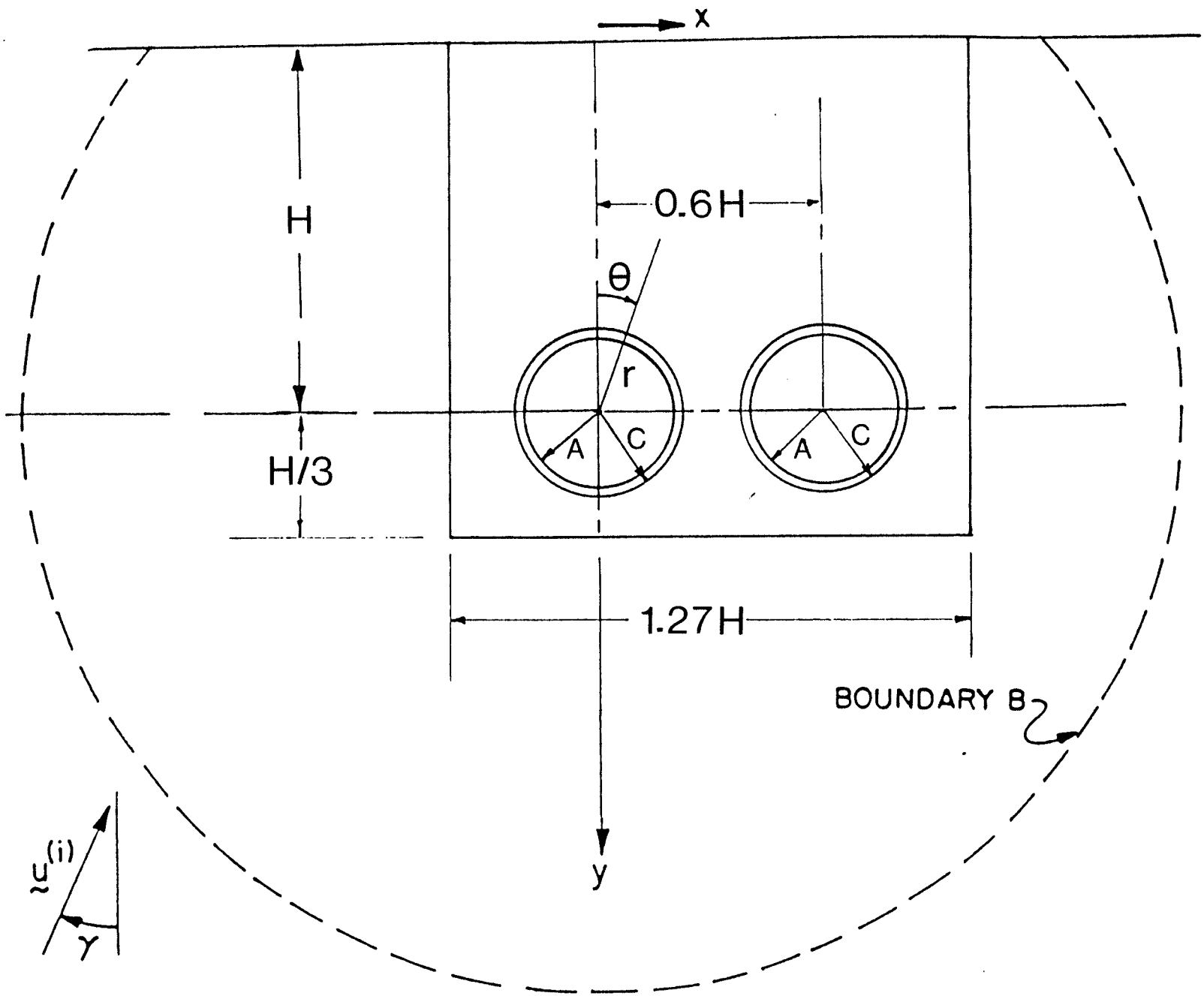

Fig.4.2 - Geometry of Two Pipes In a Rectangular Trench

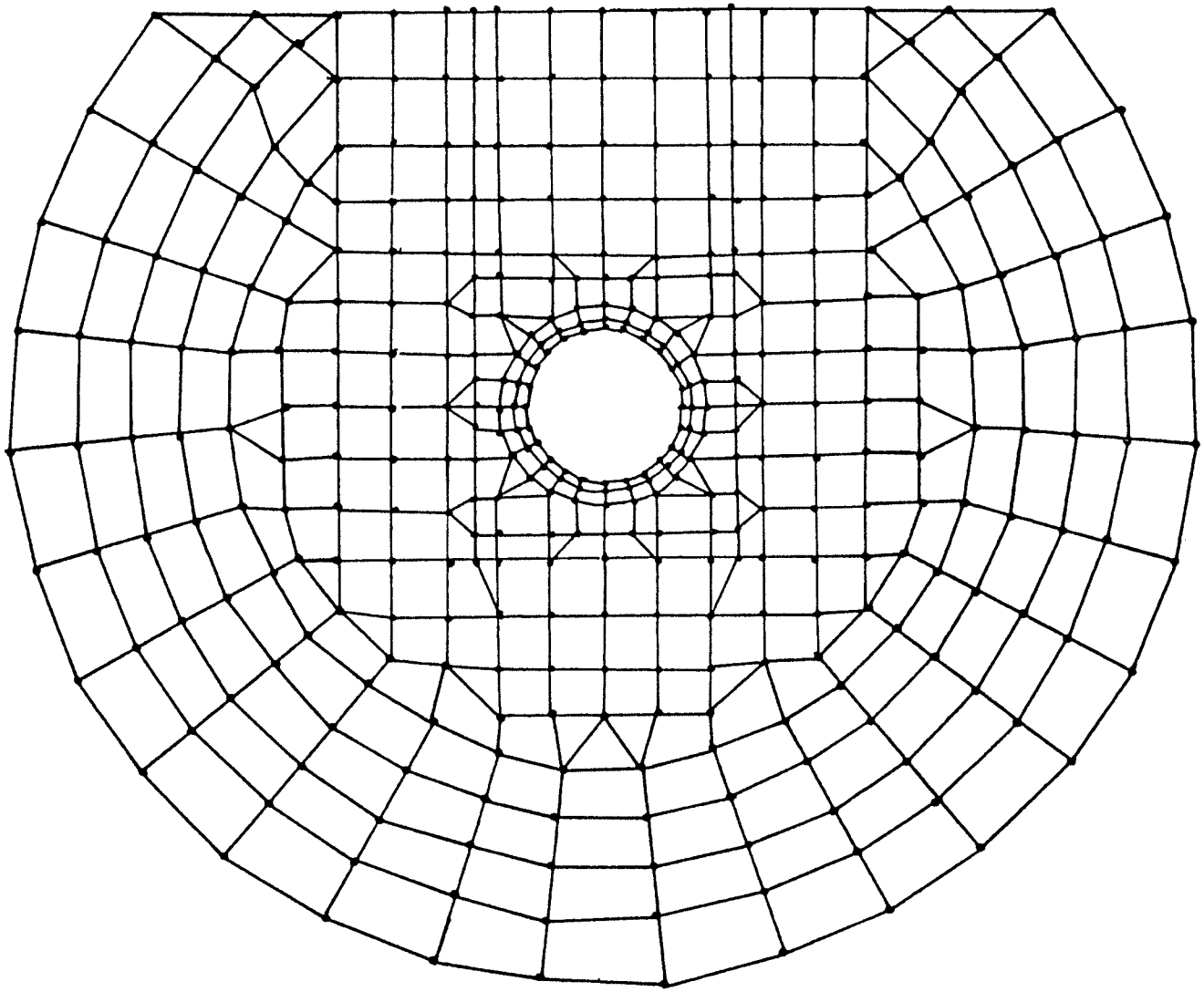

Fig.4.3 - Finite Element Mesh of a Single Pipe In a Rectangular Trench

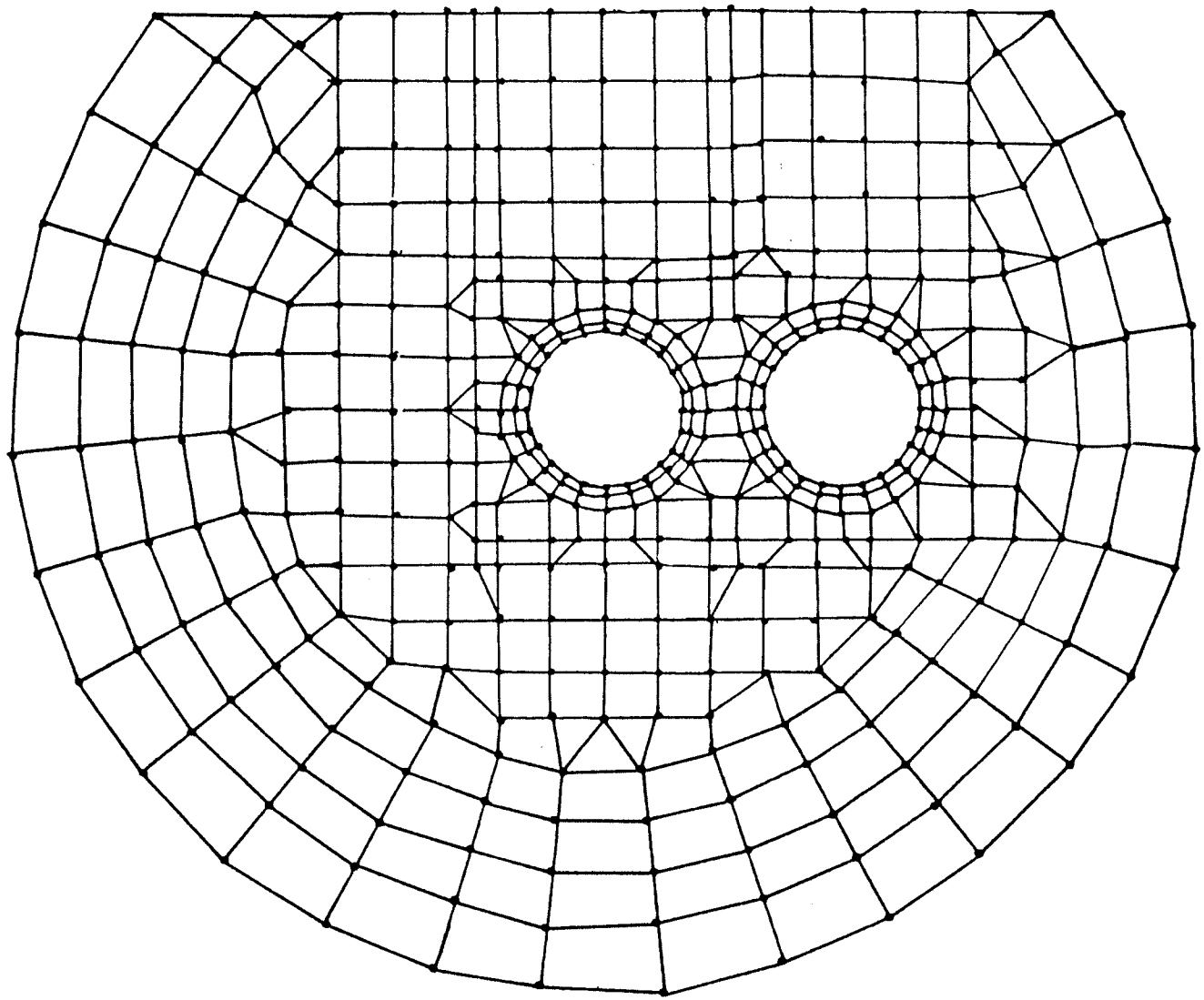

Fig.4.4 - Finite Element Mesh of Two Pipes In a Rectangular Trench

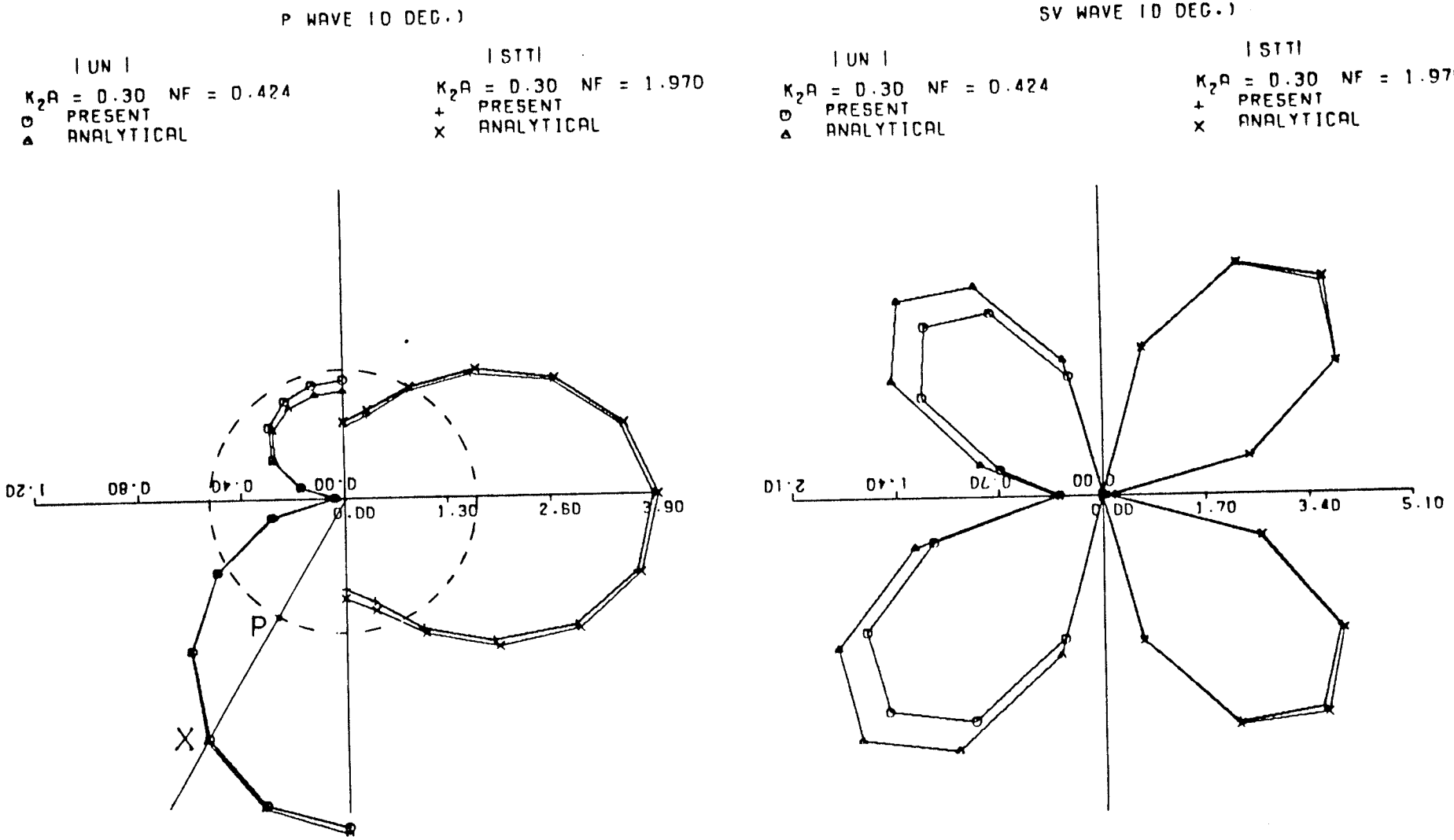

Fig.4.5 - Normalized Radial Displacement (UN) and Hoop Stress (STT) of Pipewall at r = C Calculated by FEEET and Analytically (a) P Wave at $\gamma = 0^{\circ}$ (b) SV Wave at $\gamma = 0^{\circ}$

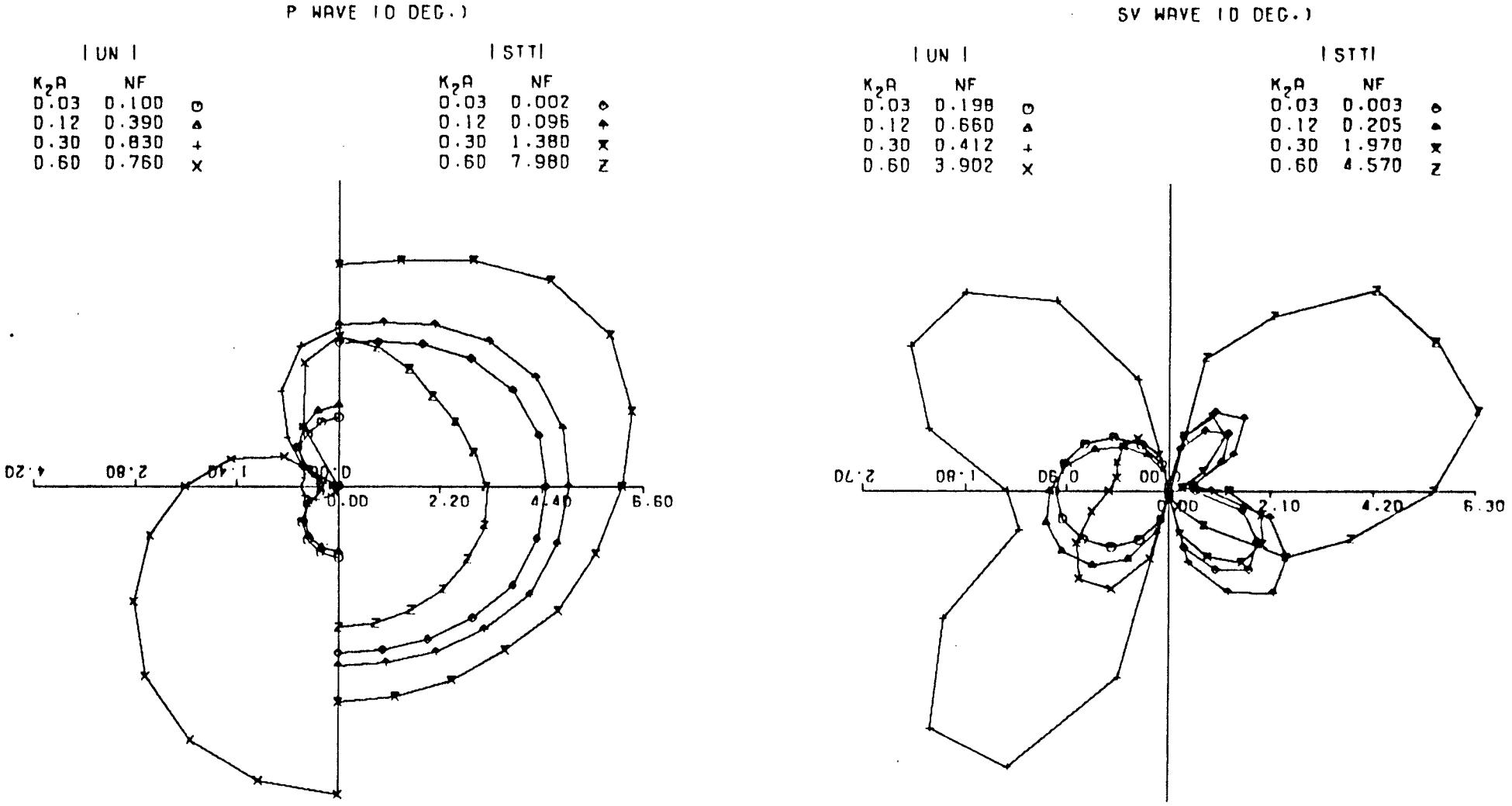

Fig.4.6 - Variation of Normalized Radial Displacement (UN) and Hoop Stress (STT) at r = C for 0° Angle of Incidence
(a) P Wave (b) SV Wave

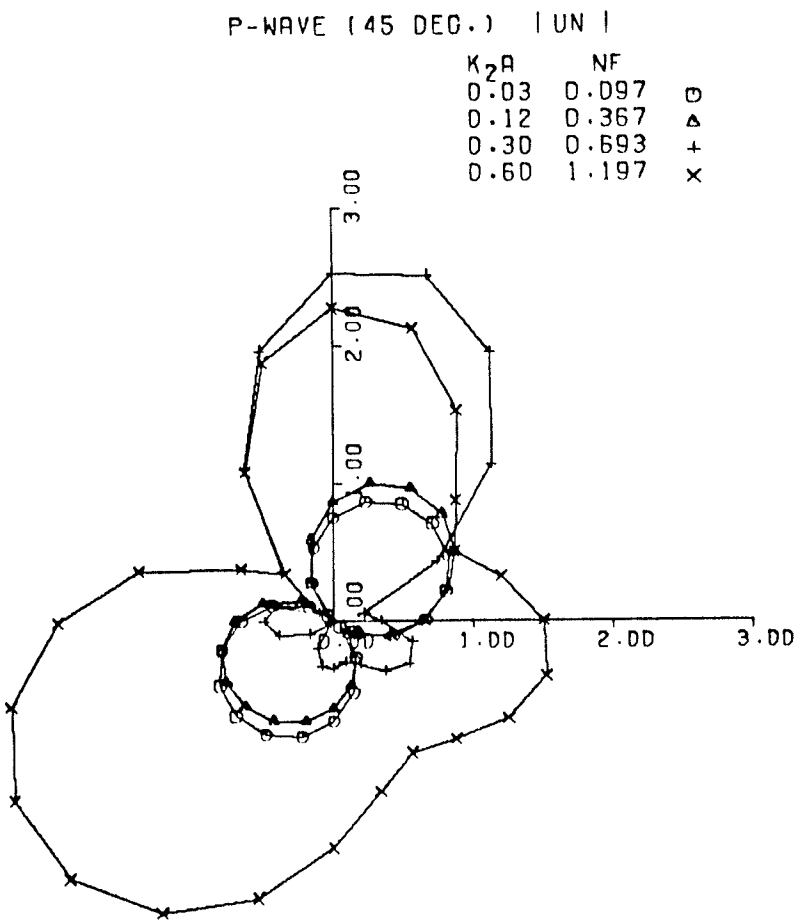

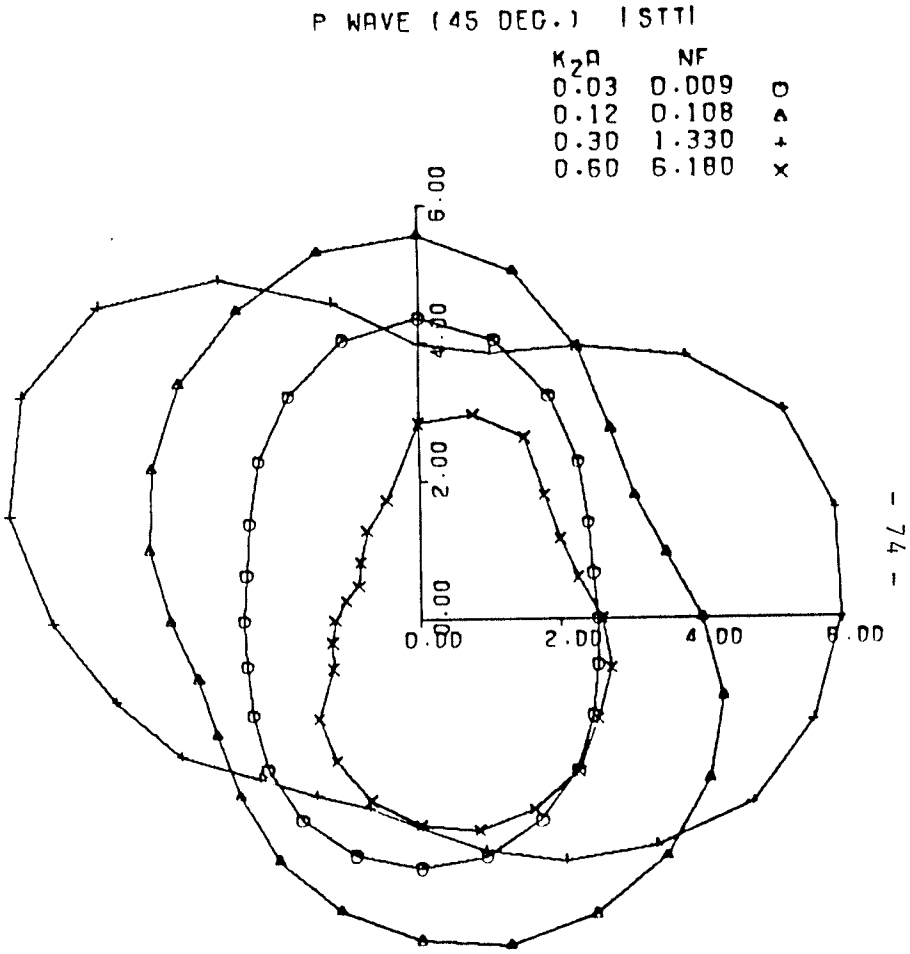

Fig.4.7 - UN and STT at r = C for P Wave at $\gamma = 45^{\circ}$

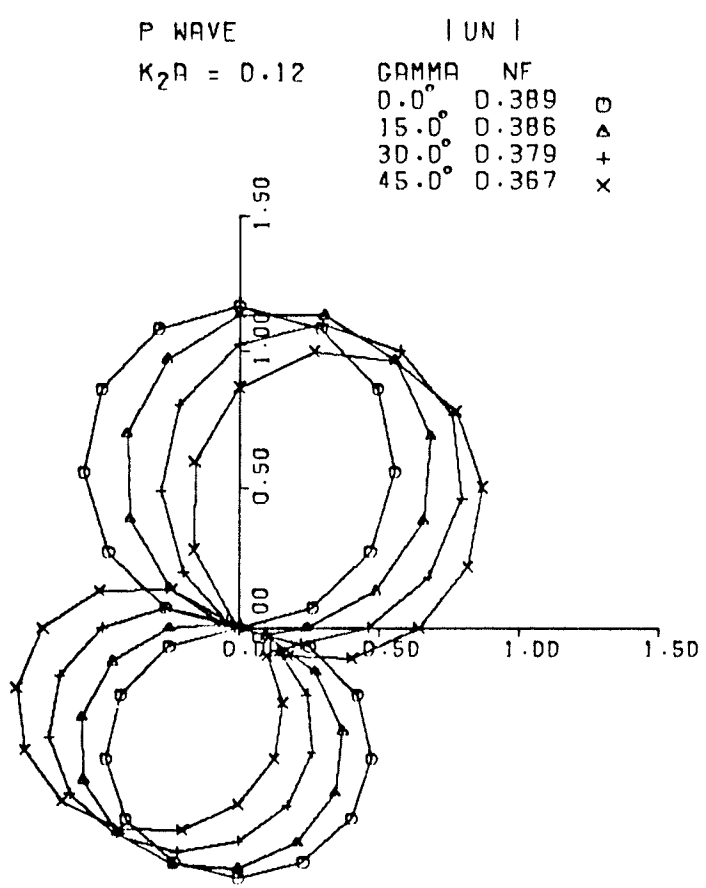

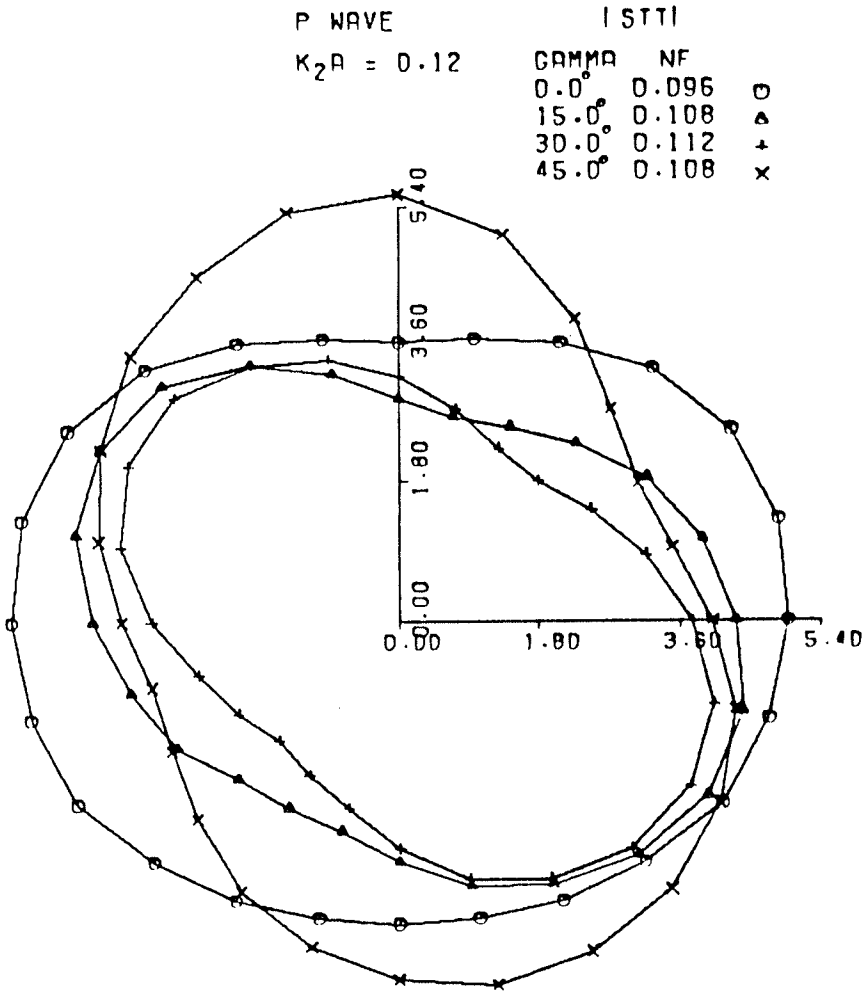

Fig.4.8 - UN and STT at r = C for P Wave at Different Angle of Incidence (γ) ; K_2A = 0.12

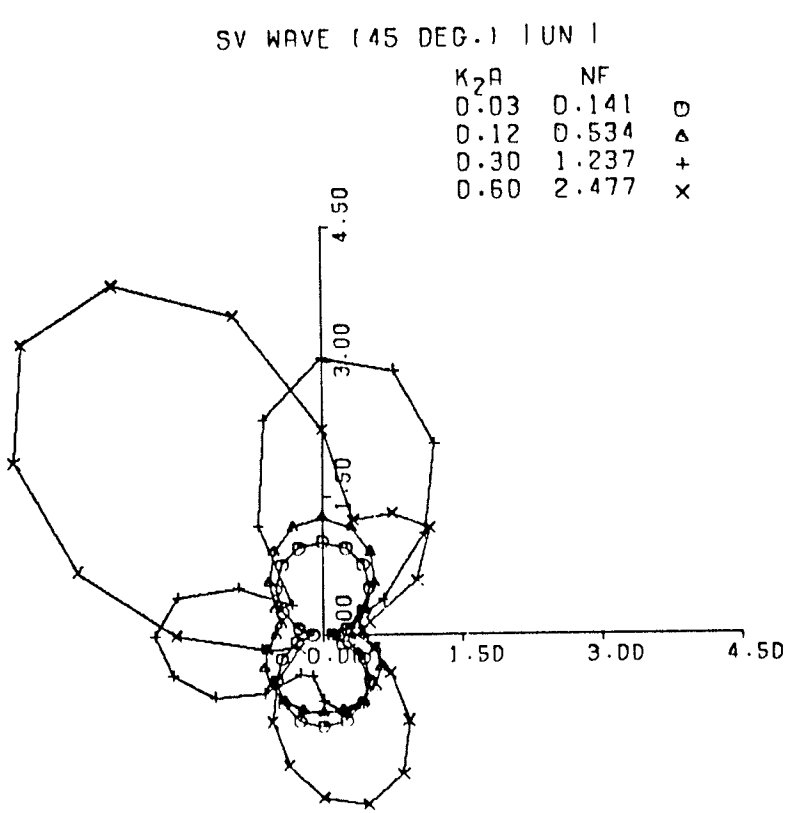

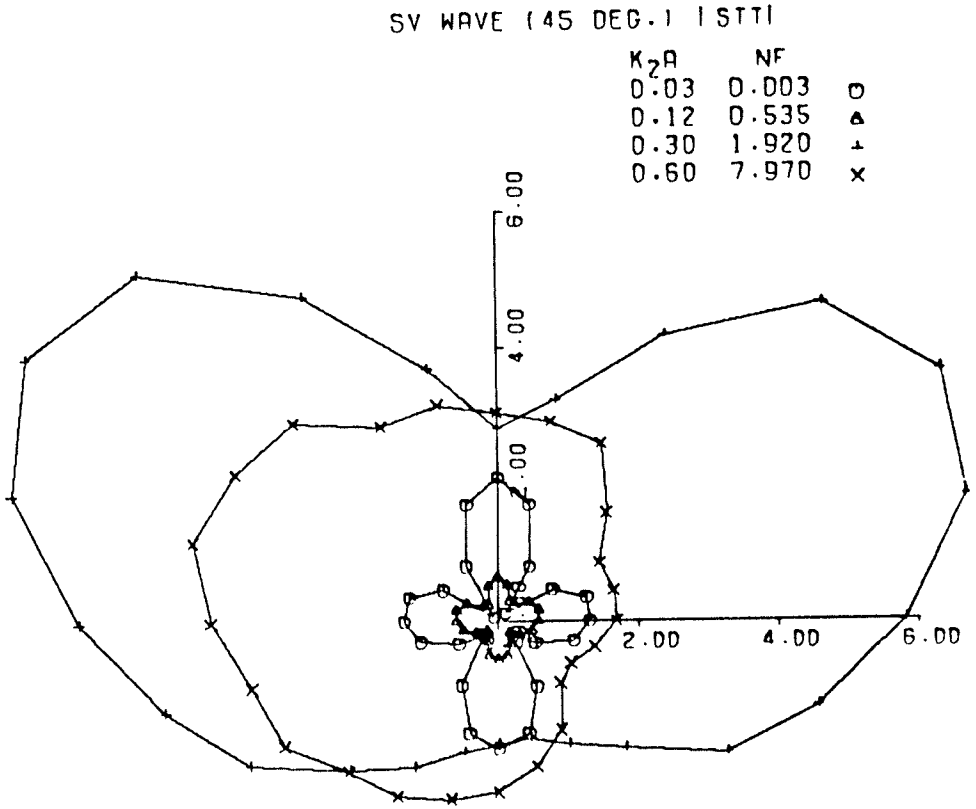

Fig.4.9 - UN and STT at r = C for SV Wave at $\gamma = 45^{\circ}$

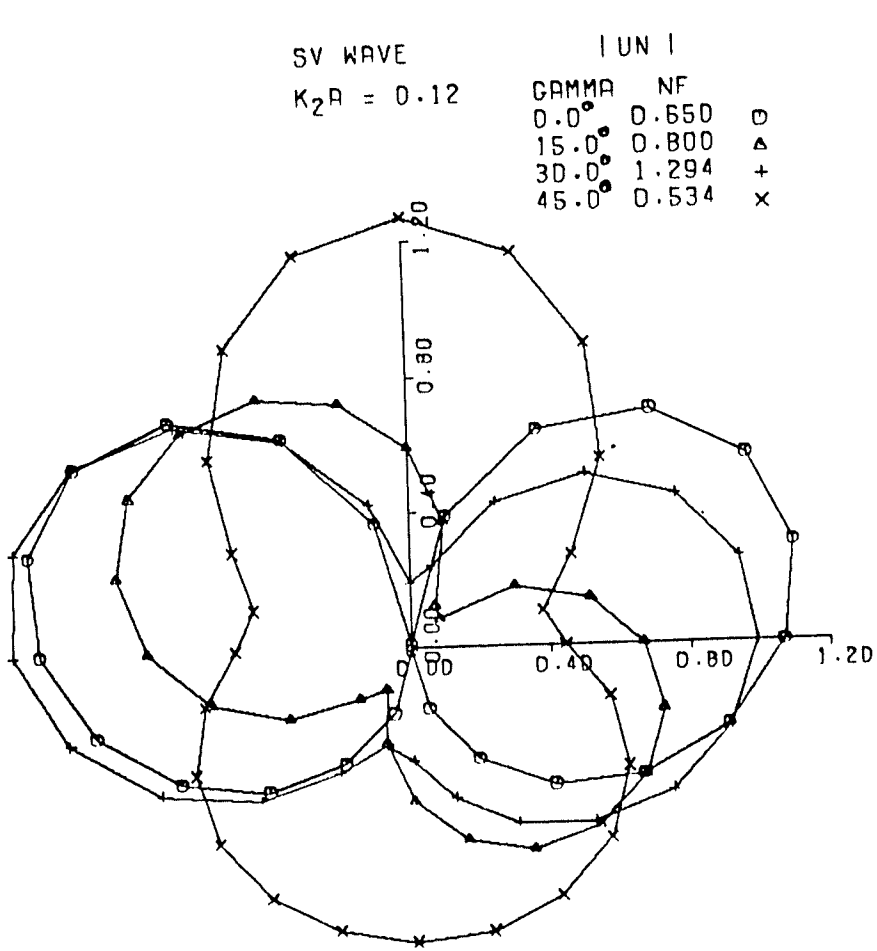

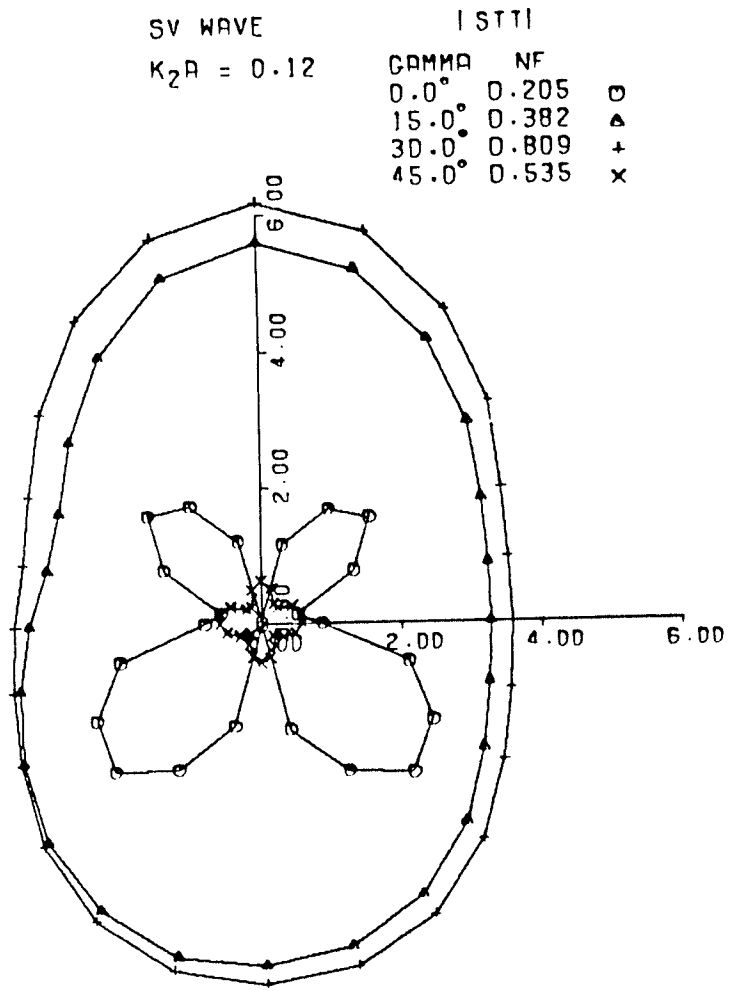

Fig.4.10 - UN and STT at r = C for SV Wave at Different γ ; K_2A = 0.12

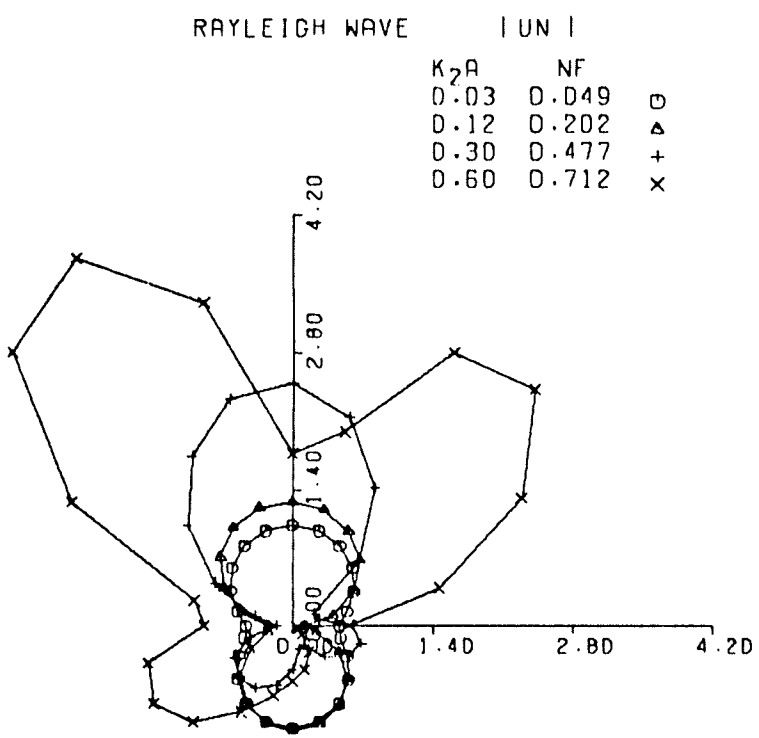

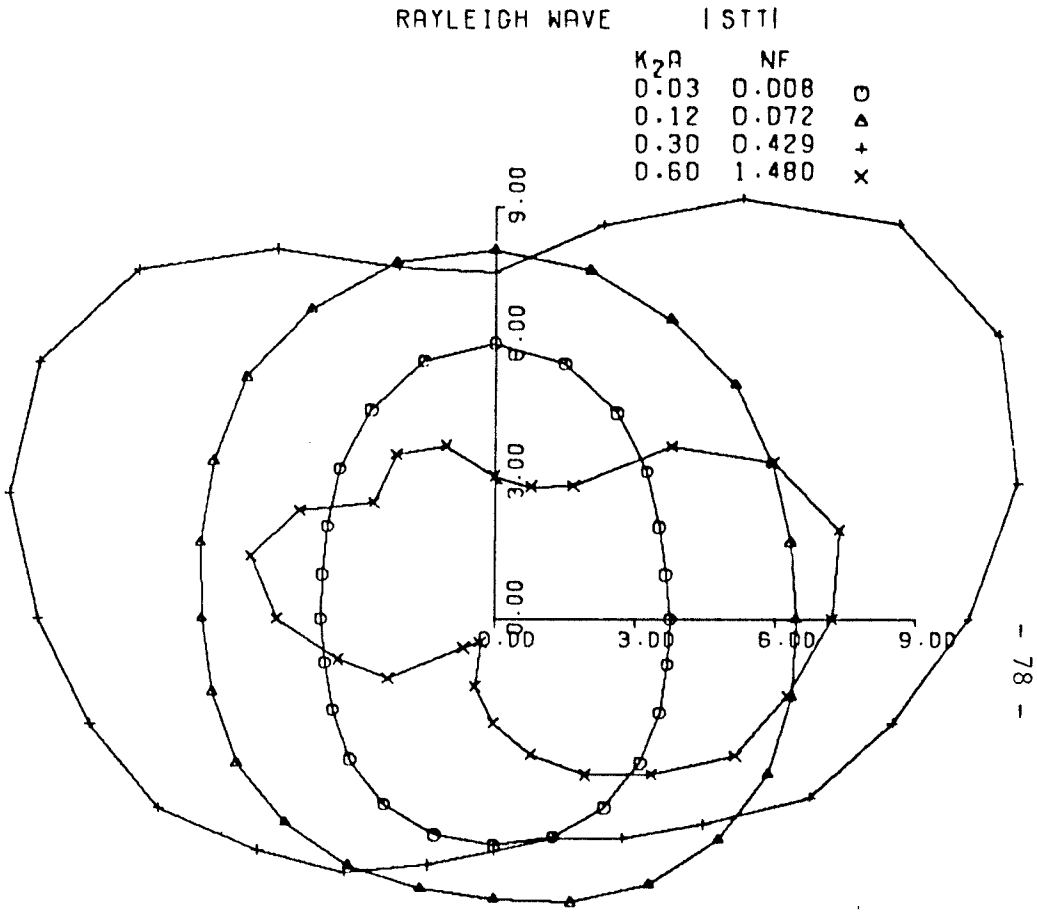

Fig.4.11 - UN and STT at r = C for Rayleigh Wave

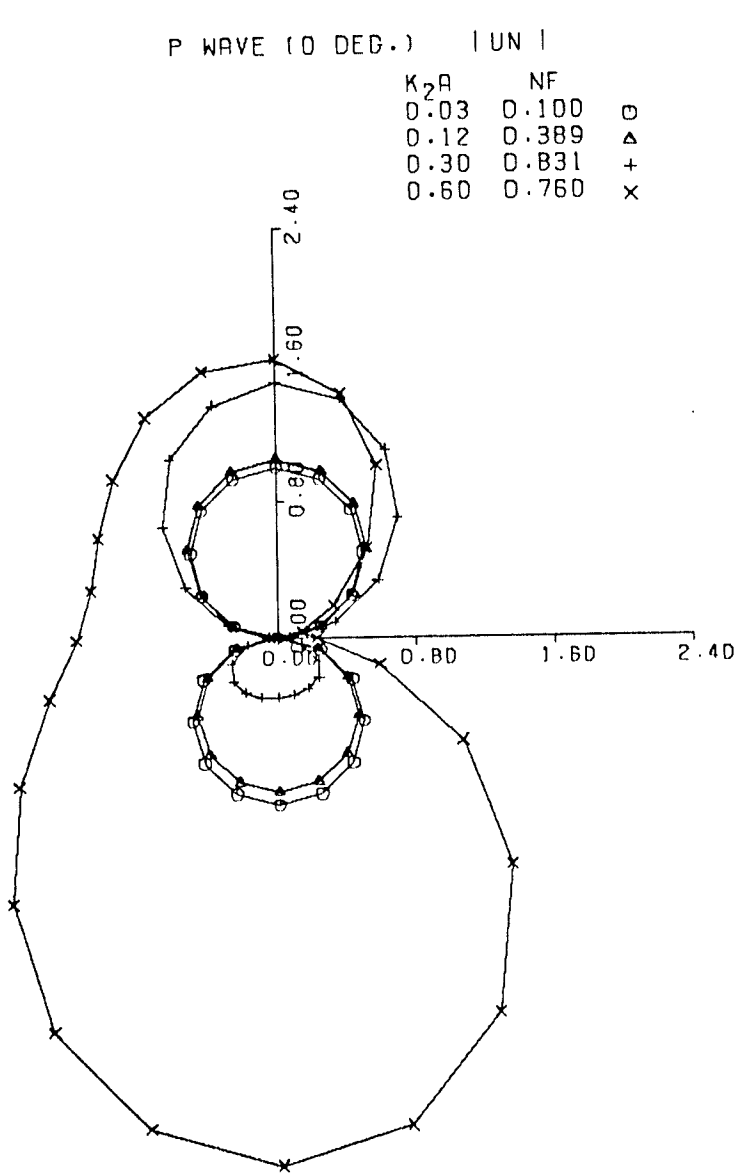

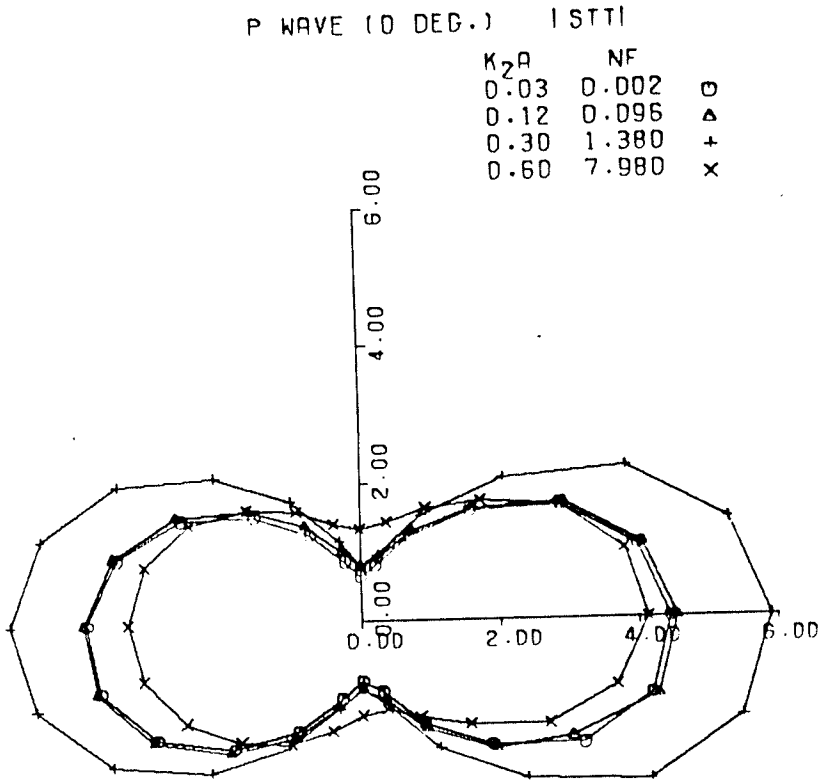

Fig.4.12 - UN and STT at r = C for P Wave at $\gamma = 0^{\circ}$ (Two Pipes)

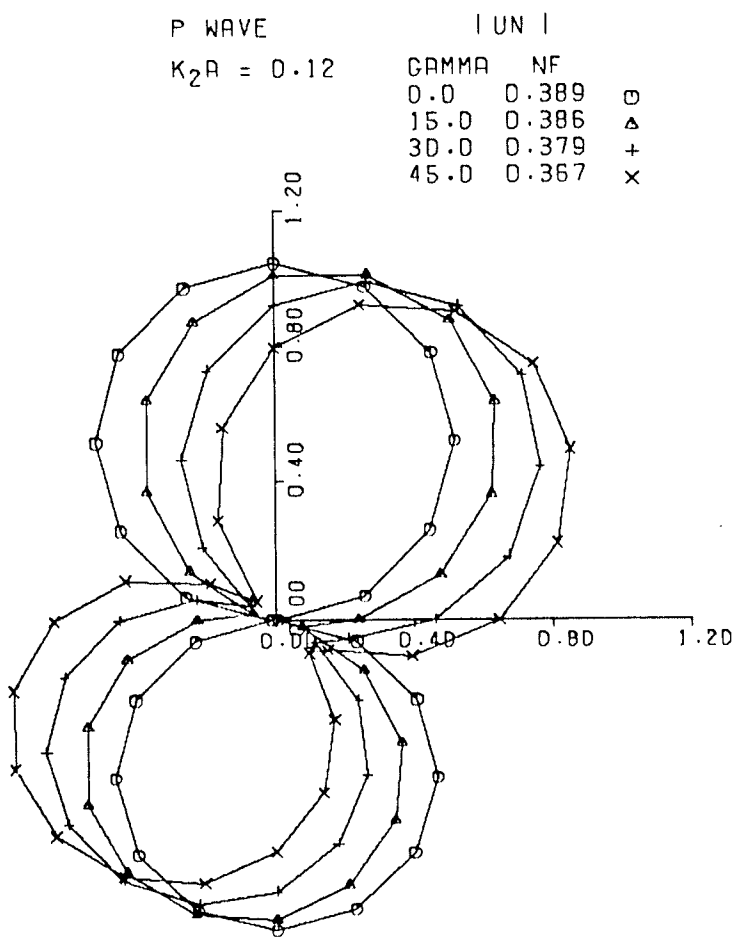

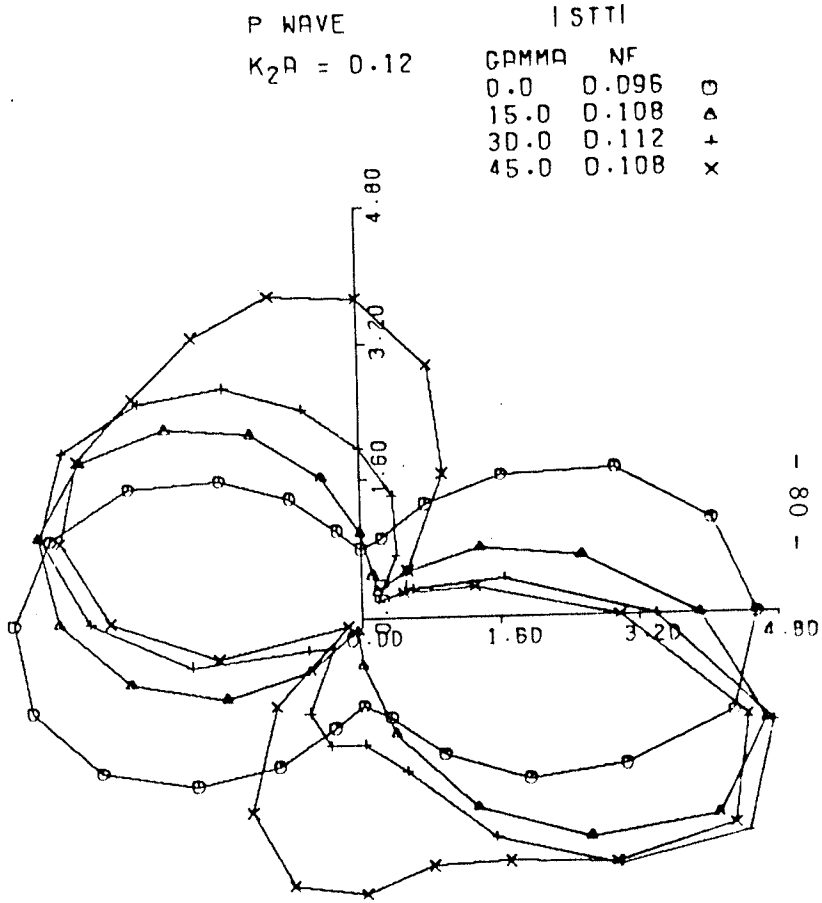

Fig.4.13 - UN and STT at r = C for P Wave at Different γ ; K_2A = 0.12 (Two Pipes)

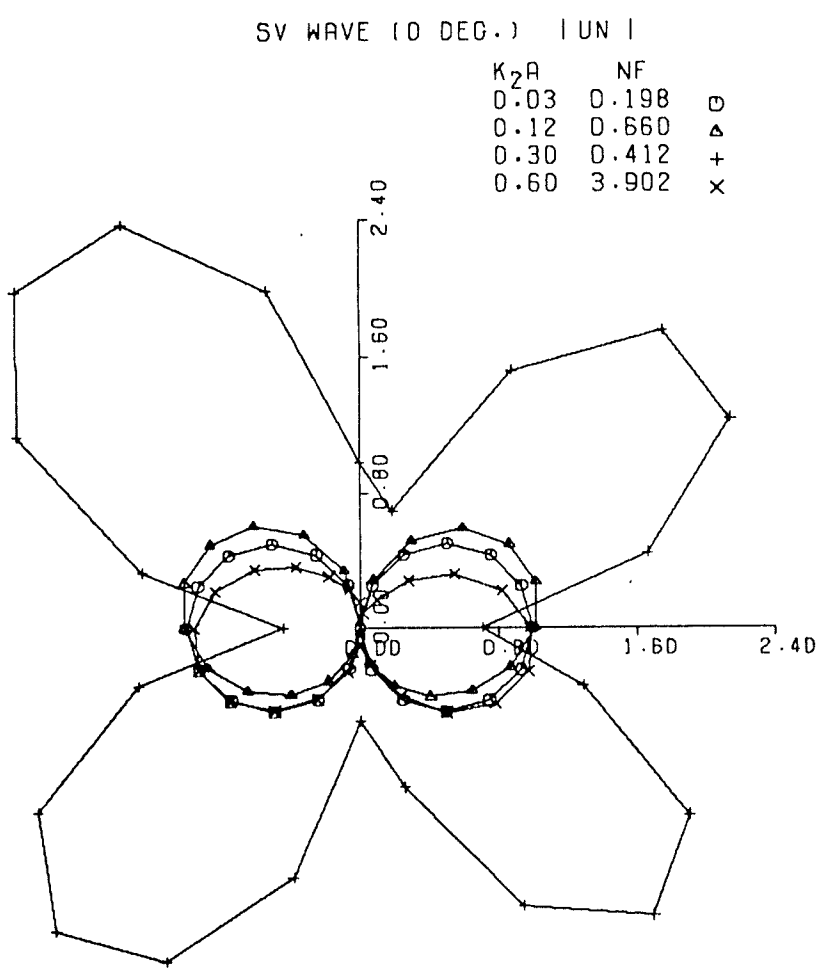

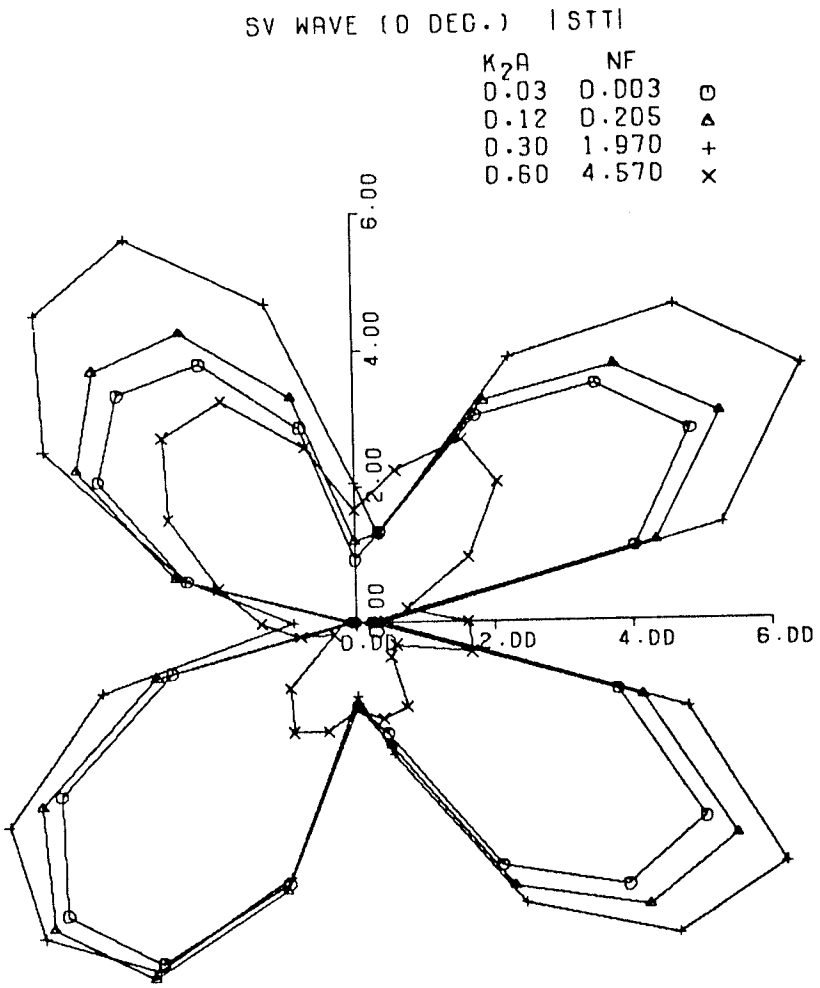

Fig.4.14 - UN and STT at r = C for SV Wave at $\gamma = 0^{\circ}$ (Two Pipes)

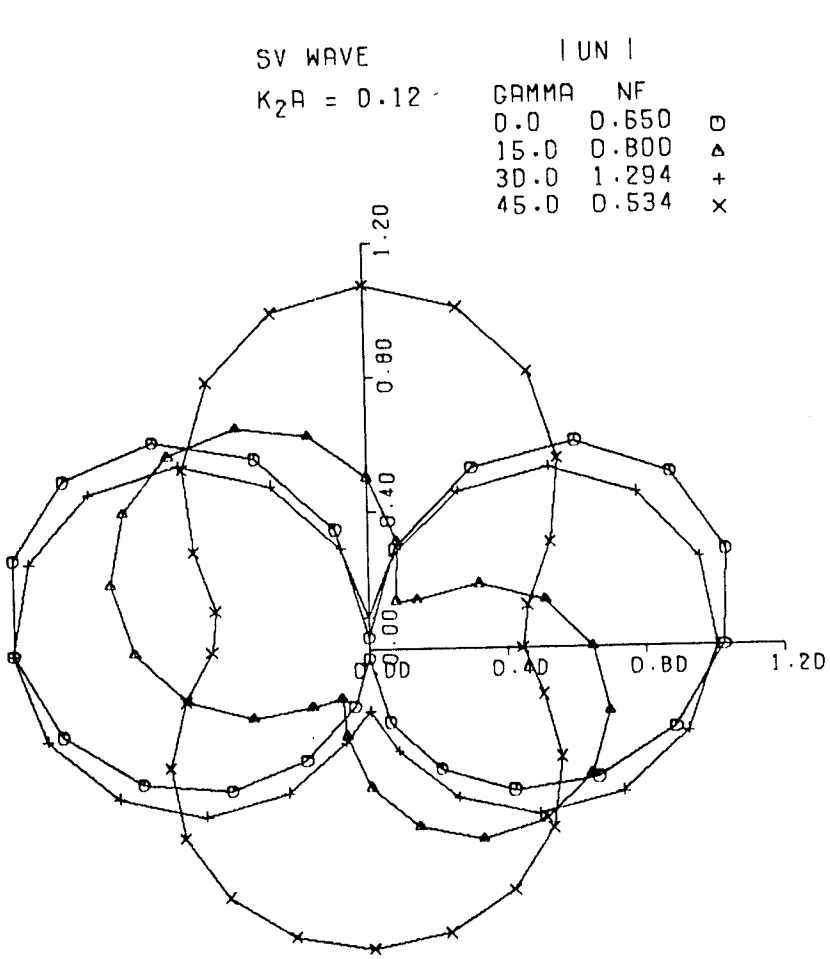

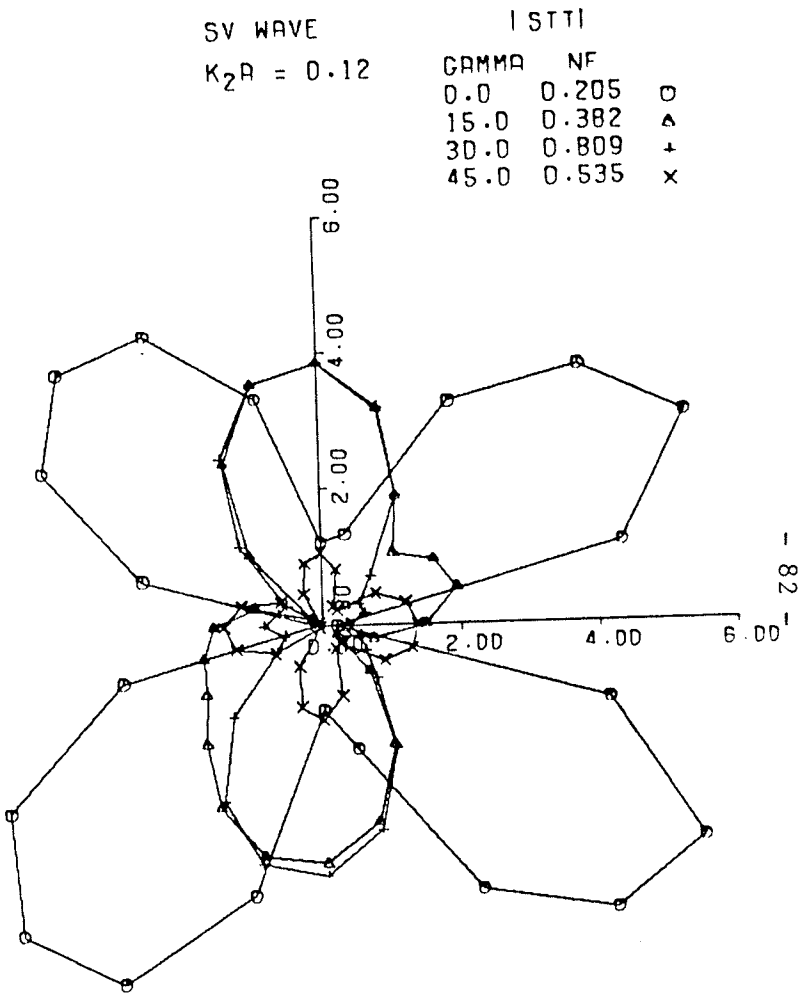

Fig.4.15 - UN and STT at r = C for SV Wave at Different γ ; K_2A = 0.12 (Two Pipes)

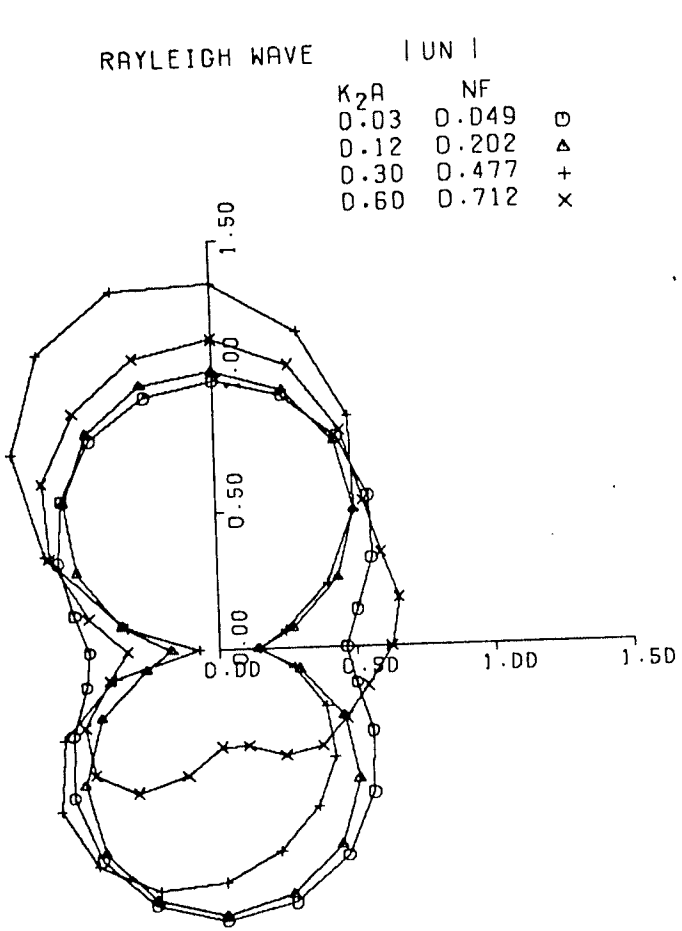

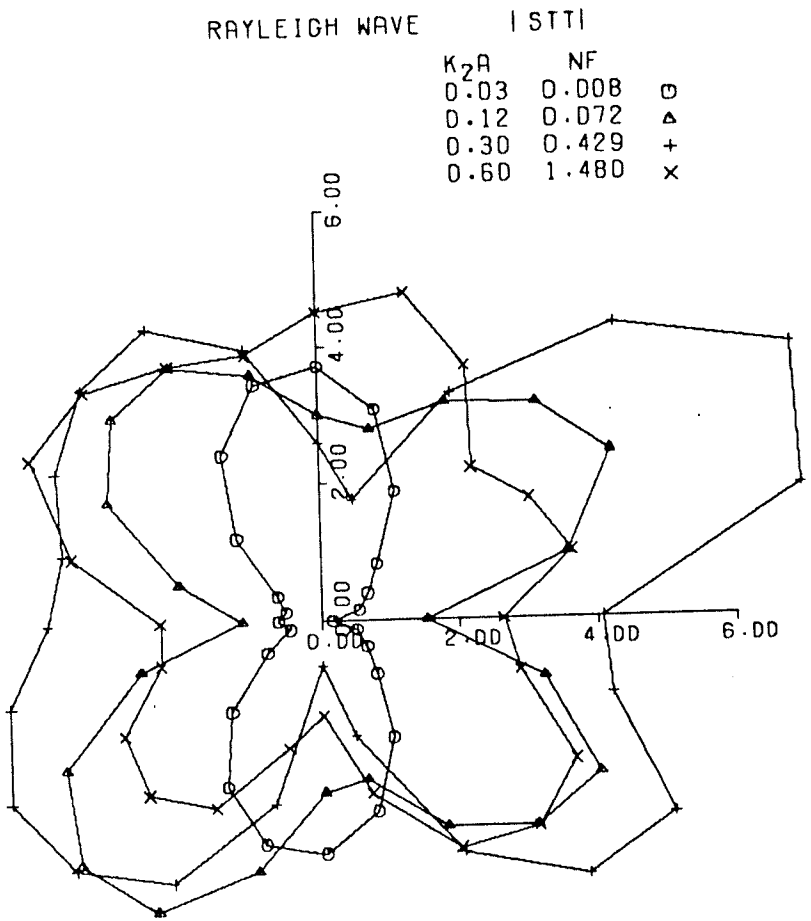

Fig.4.16 - UN and STT at r = C for Rayleigh Wave (Two Pipes)

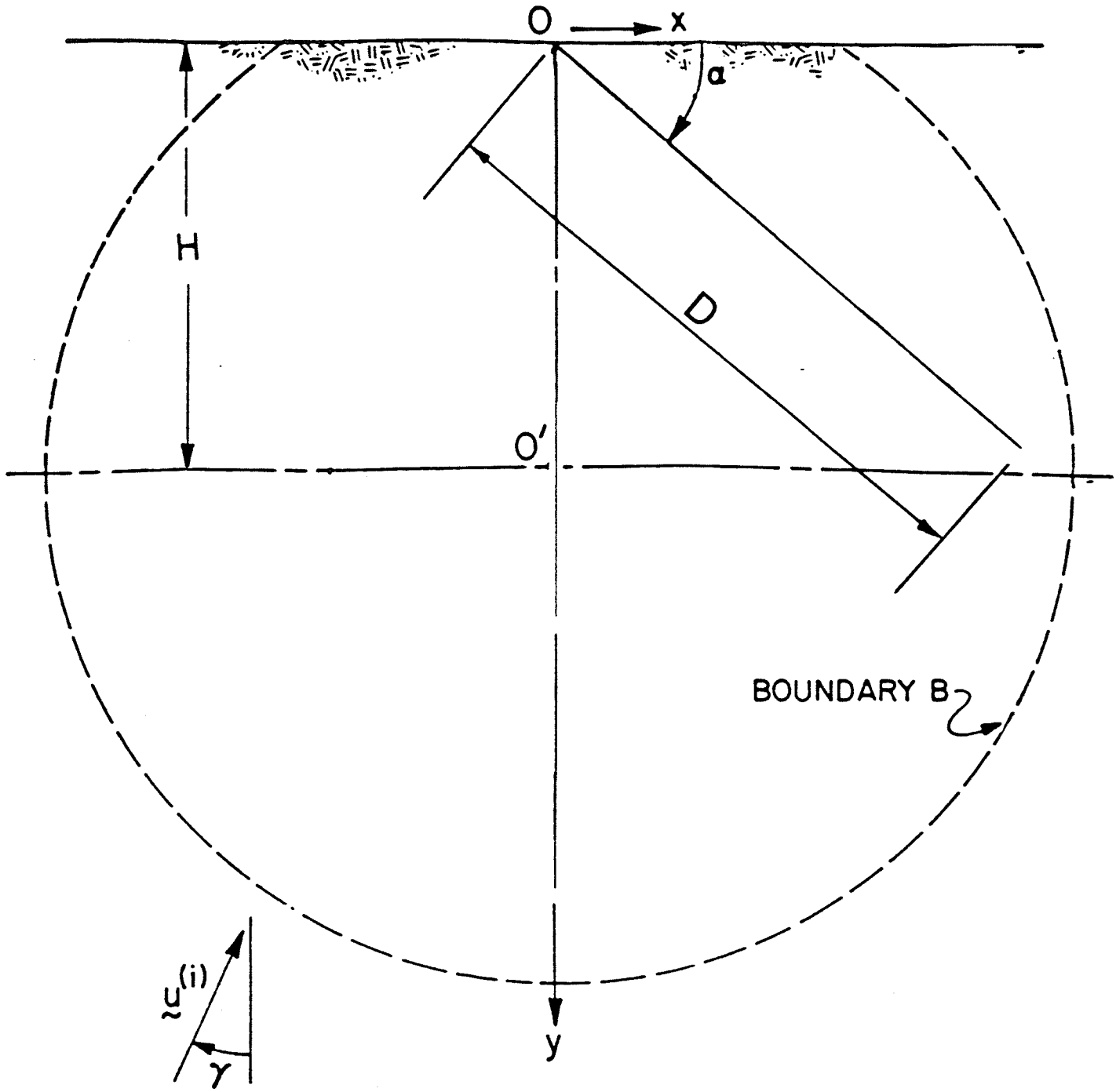

Fig. 5.1 - Geometry of Surface Breaking Straight Crack

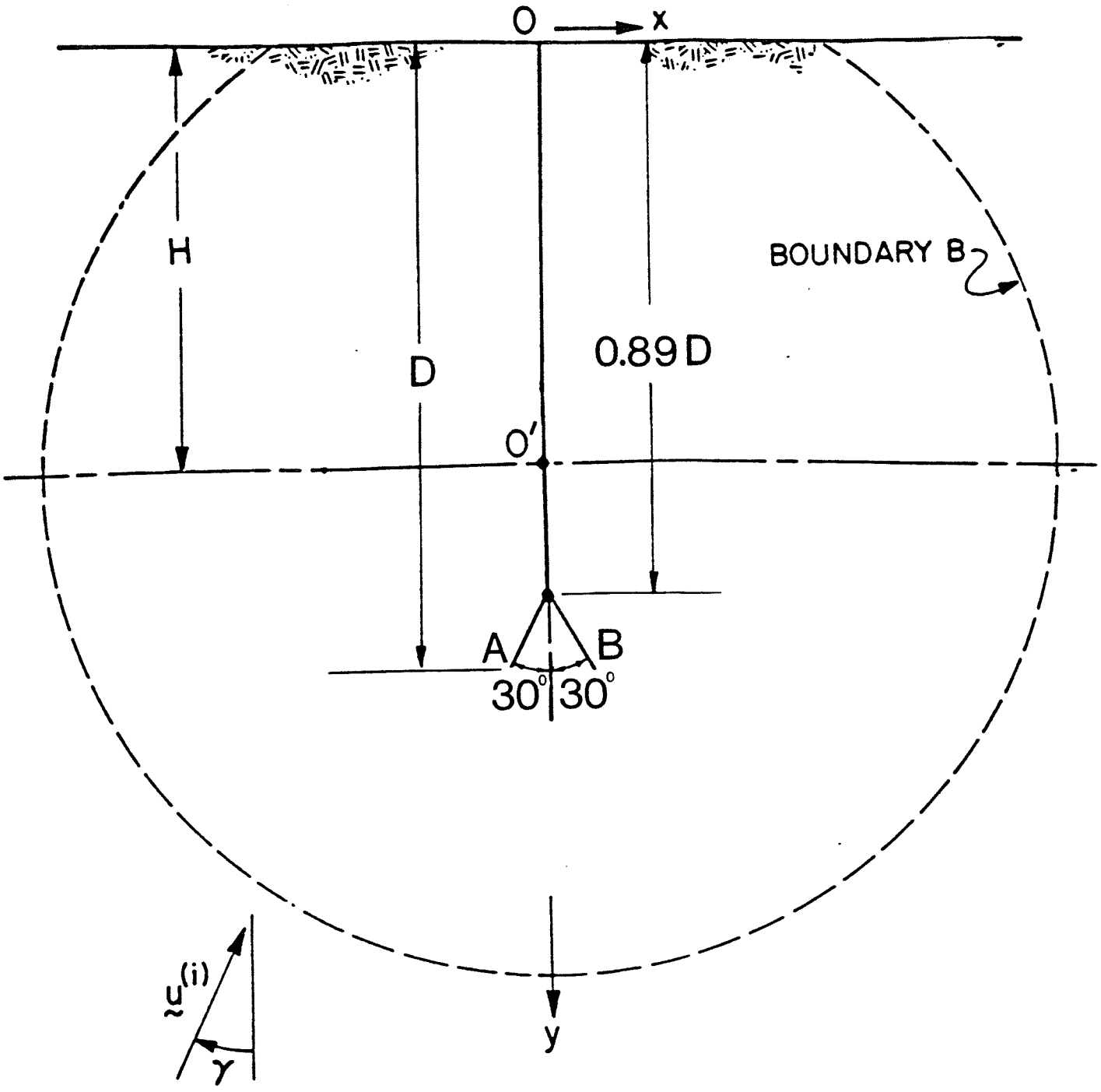

Fig. 5.2 - Geometry of Surface Breaking Y Crack

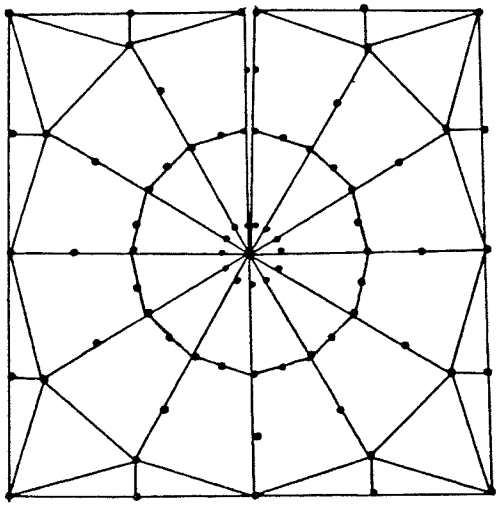

(a)

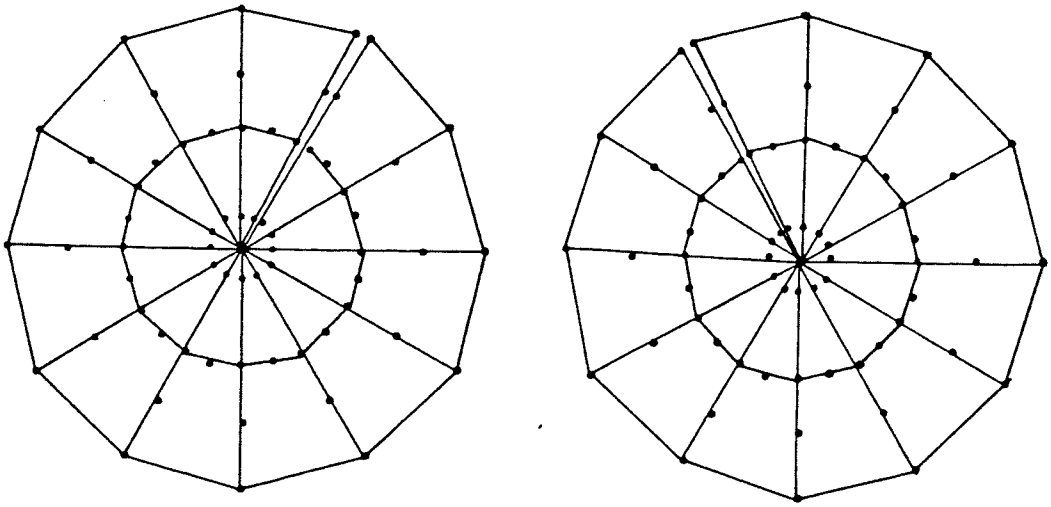

(b)

Fig. 5.3 - Crack Tip Elements of the Surface Breaking
(a) Vertical & 45° Inclinced Crack (b) Y Crack

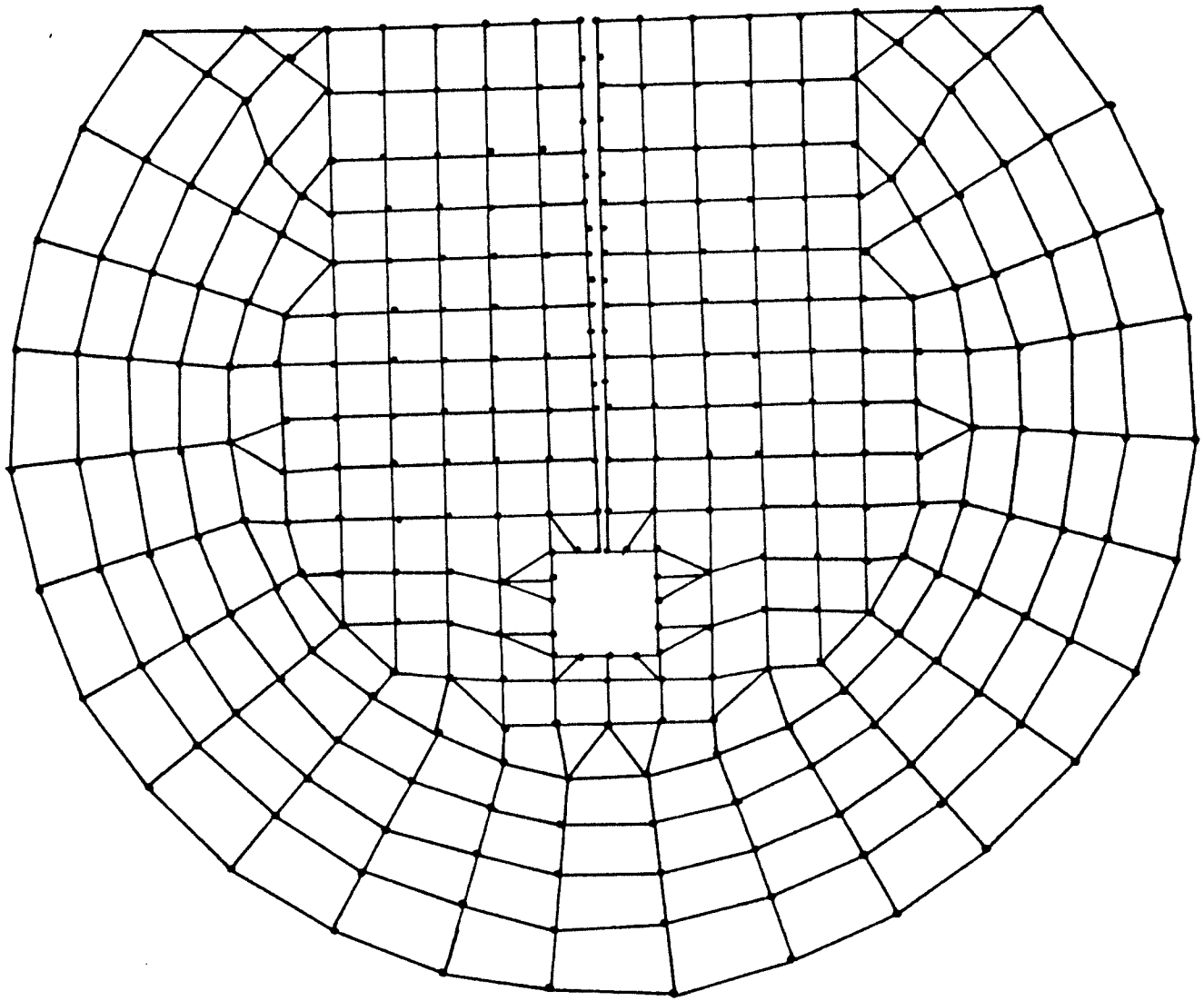

Fig. 5.4 - Finite Element Mesh of the Surface Breaking Vertical Crack

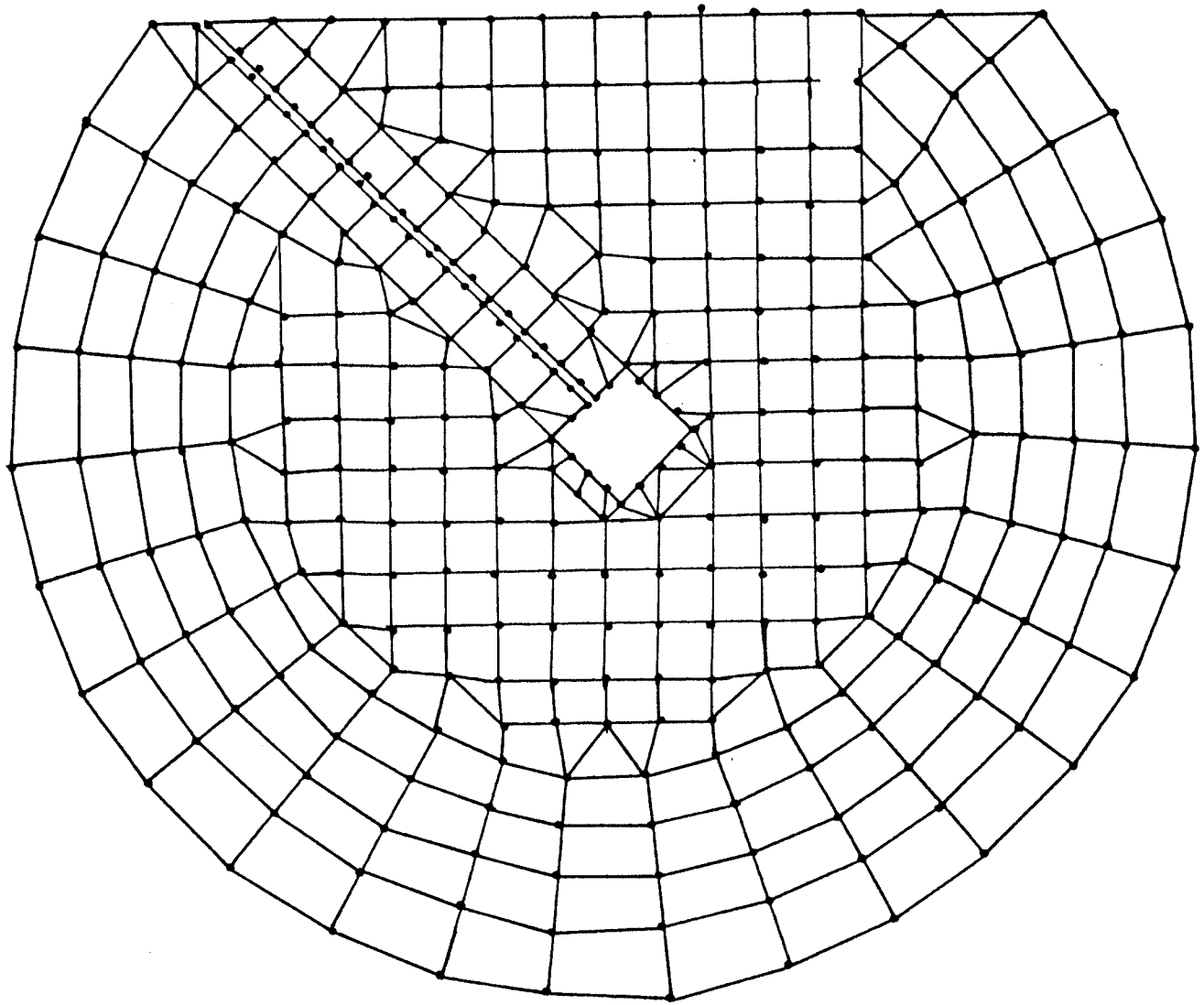

Fig. 5.5 - Finite Element Mesh of the Surface Breaking 45° Inclined Crack

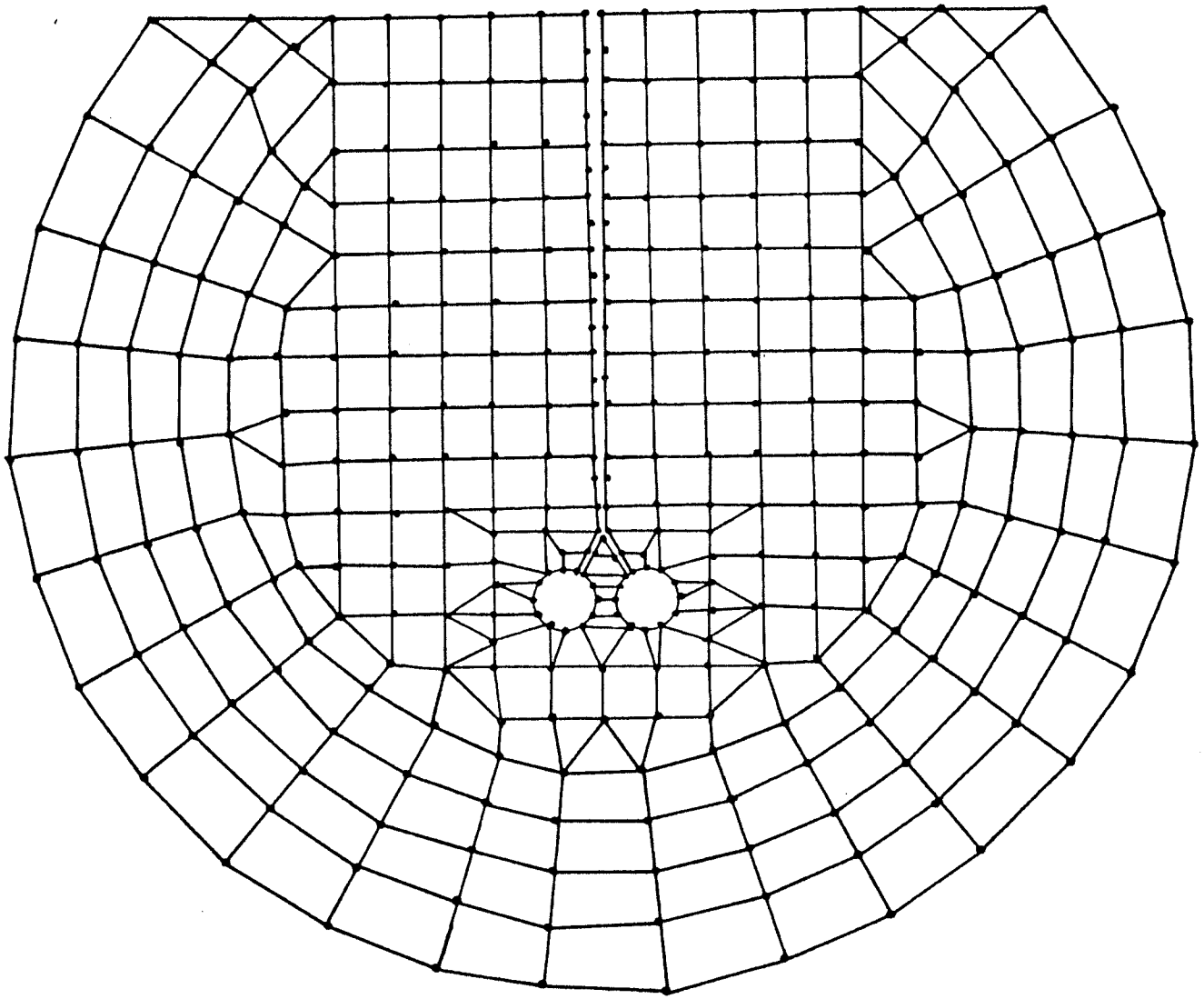

Fig. 5.6 - Finite Element Mesh of the Surface Breaking Y Crack

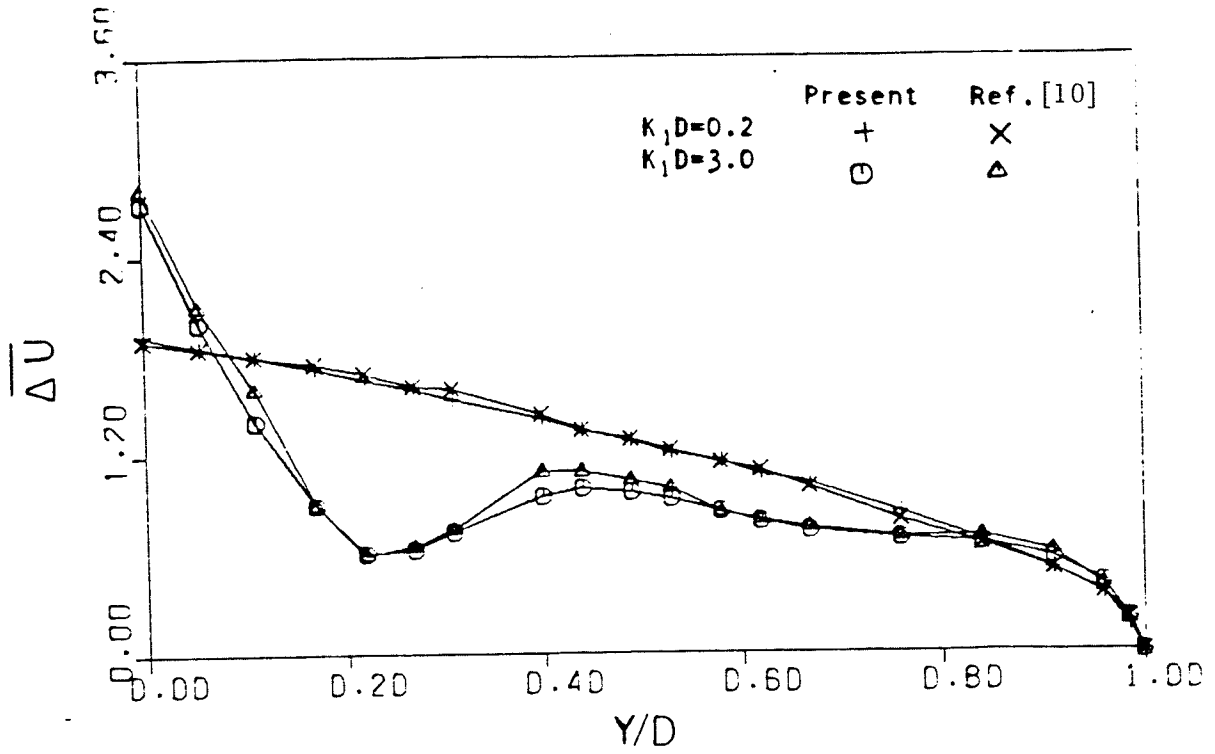

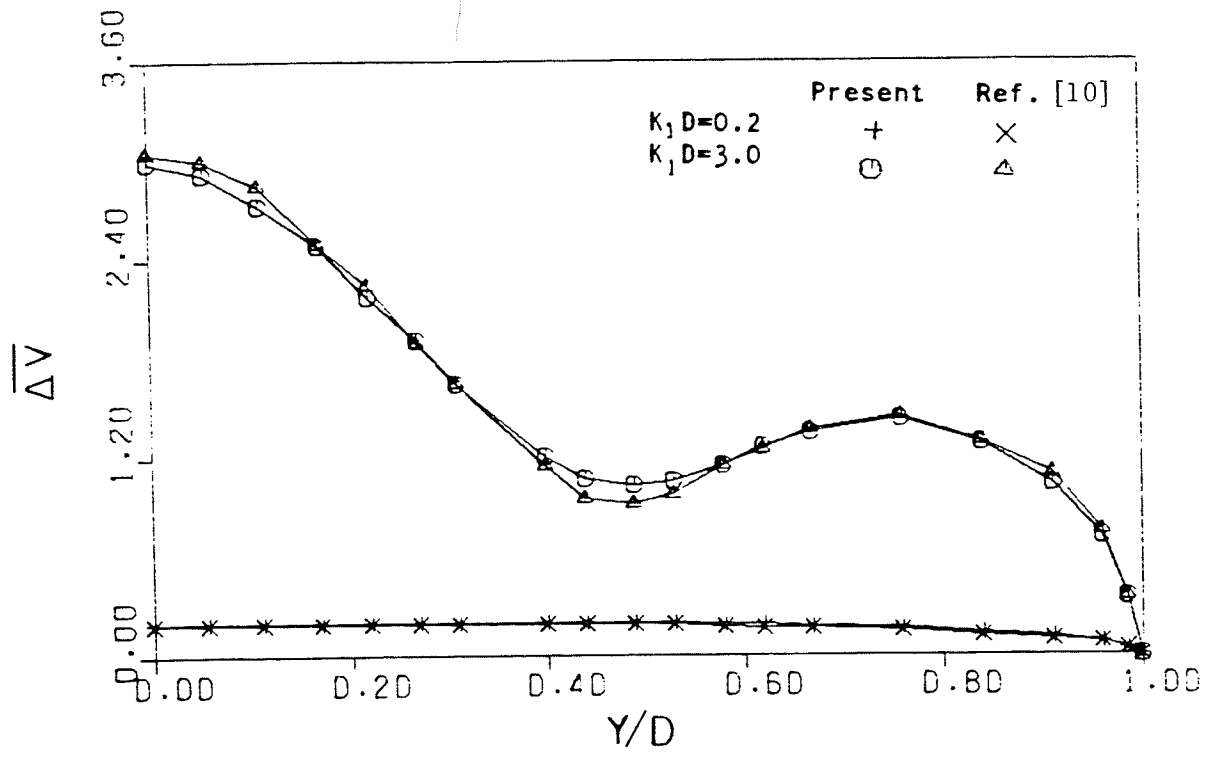

Fig. 5.7 - Comparision of normal ($\overline{\Delta U}$) and tangential ($\overline{\Delta V}$) crack opening displacements with those of Ref. [10].

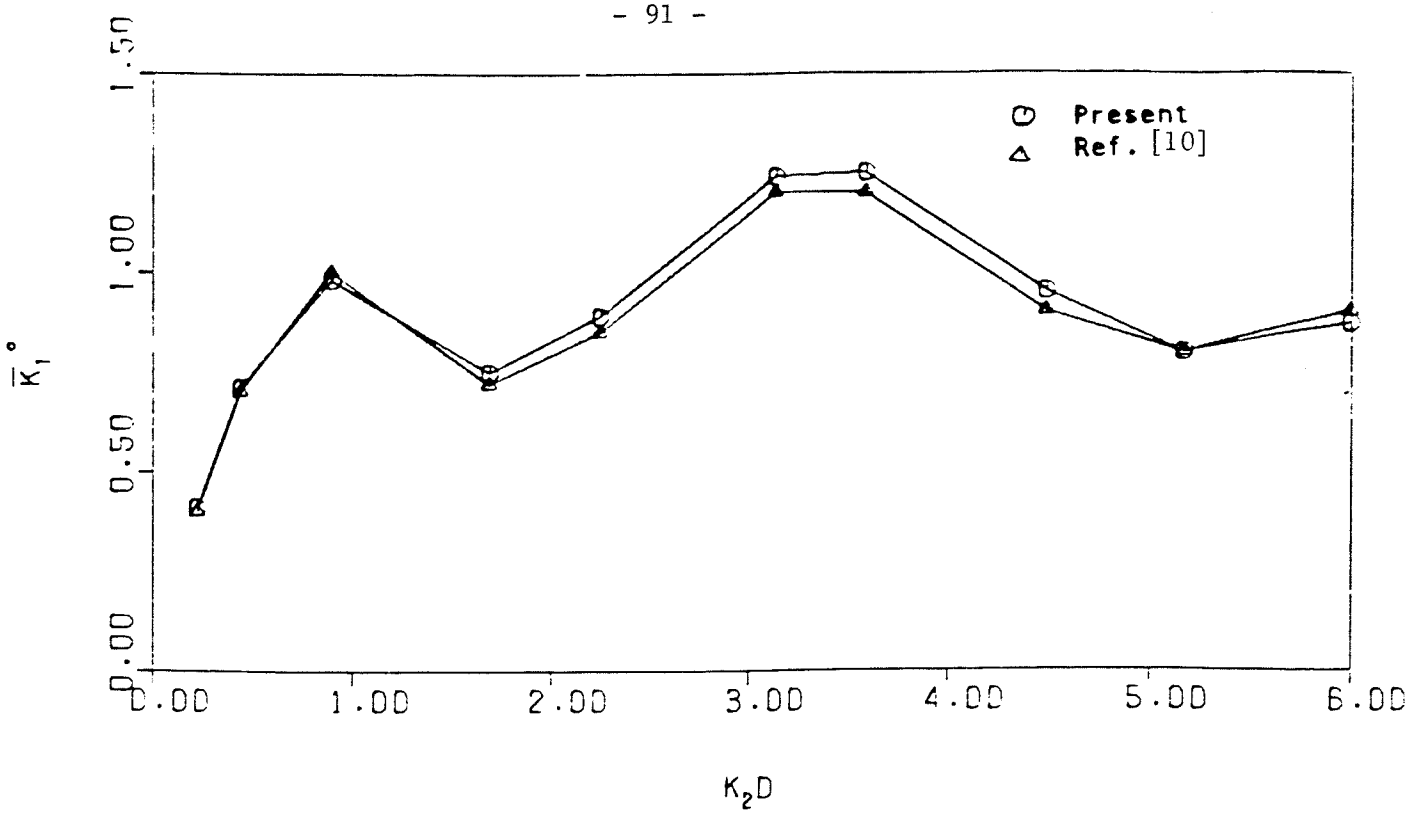

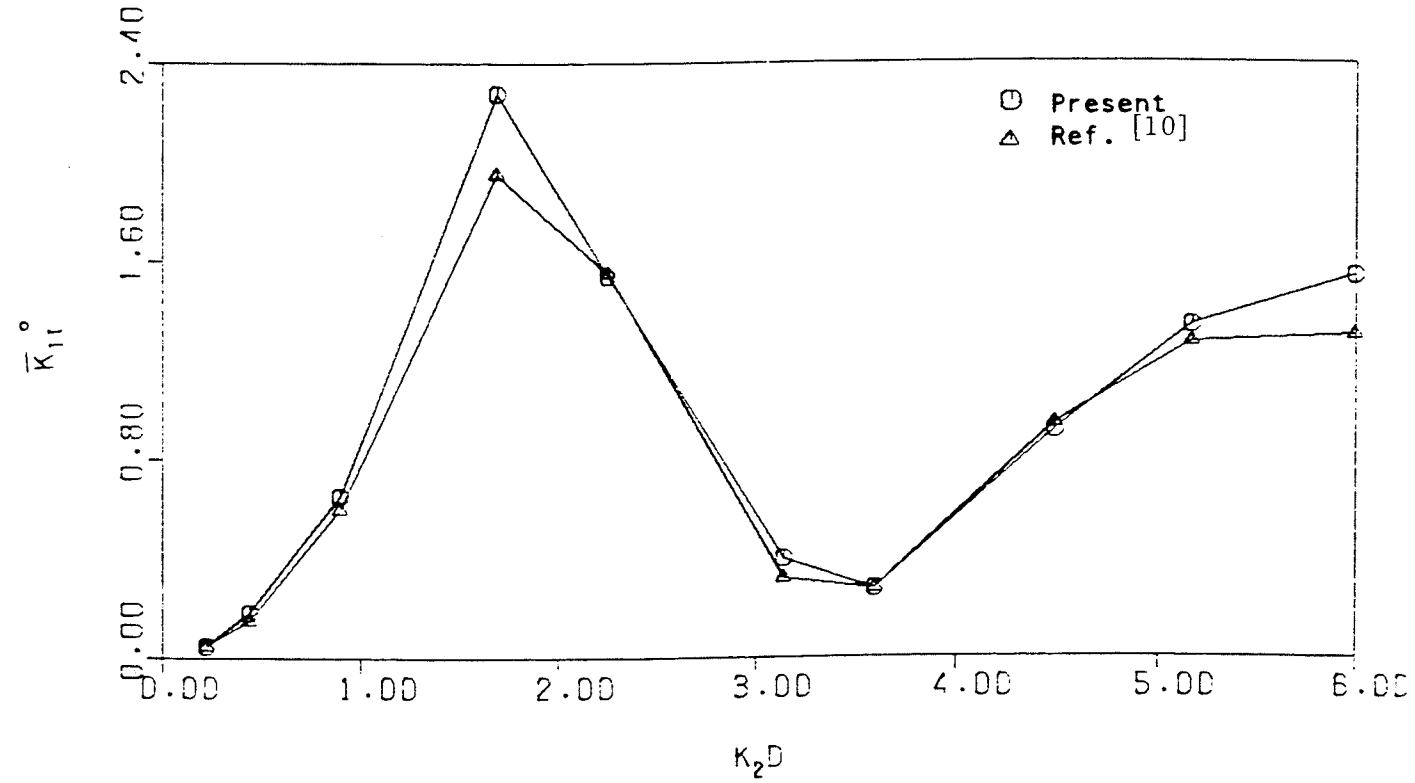

Fig. 5.8 - Comparision of Mode I (K_I°) and Mode Ii (K_{II}°) stress intensity factors with those of Ref. [10].

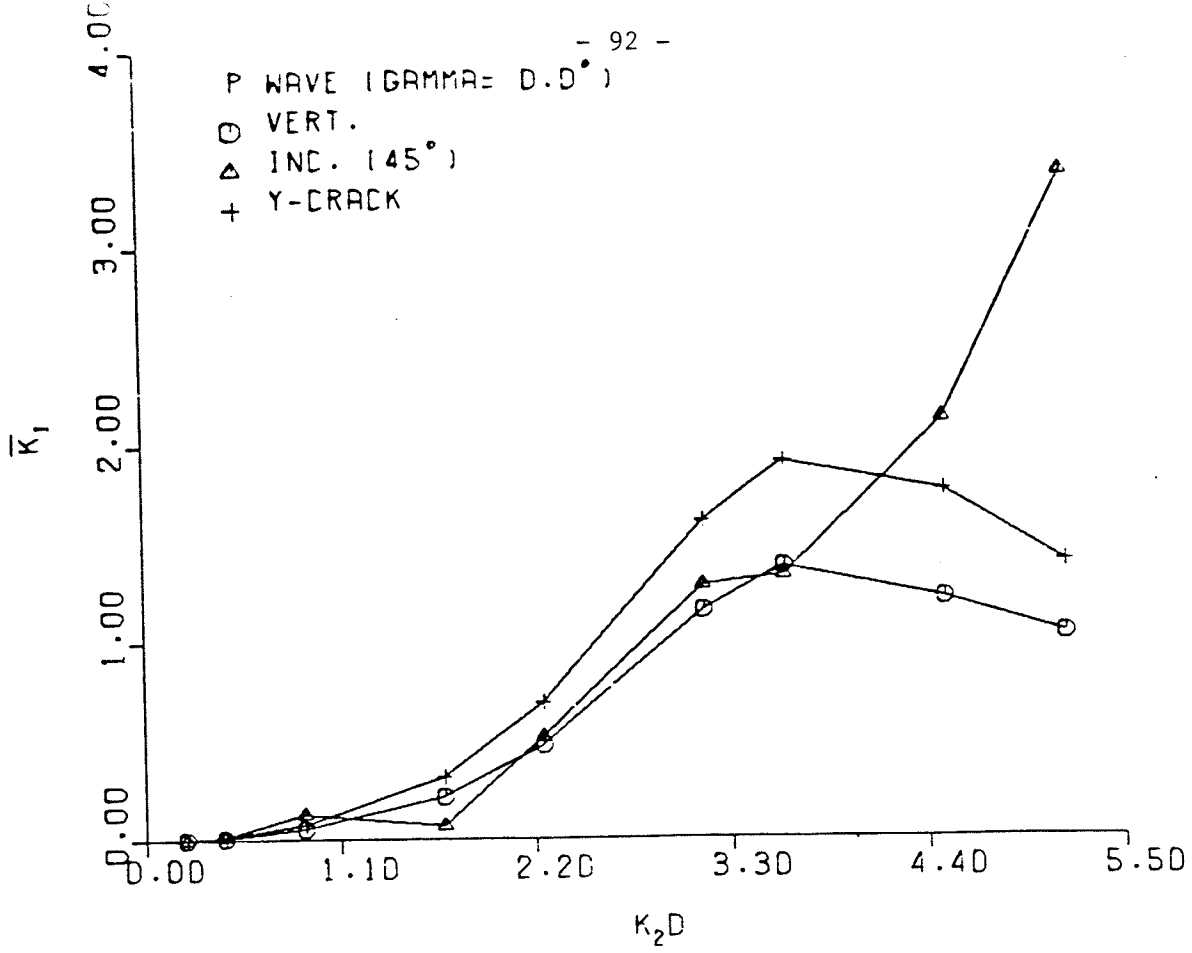

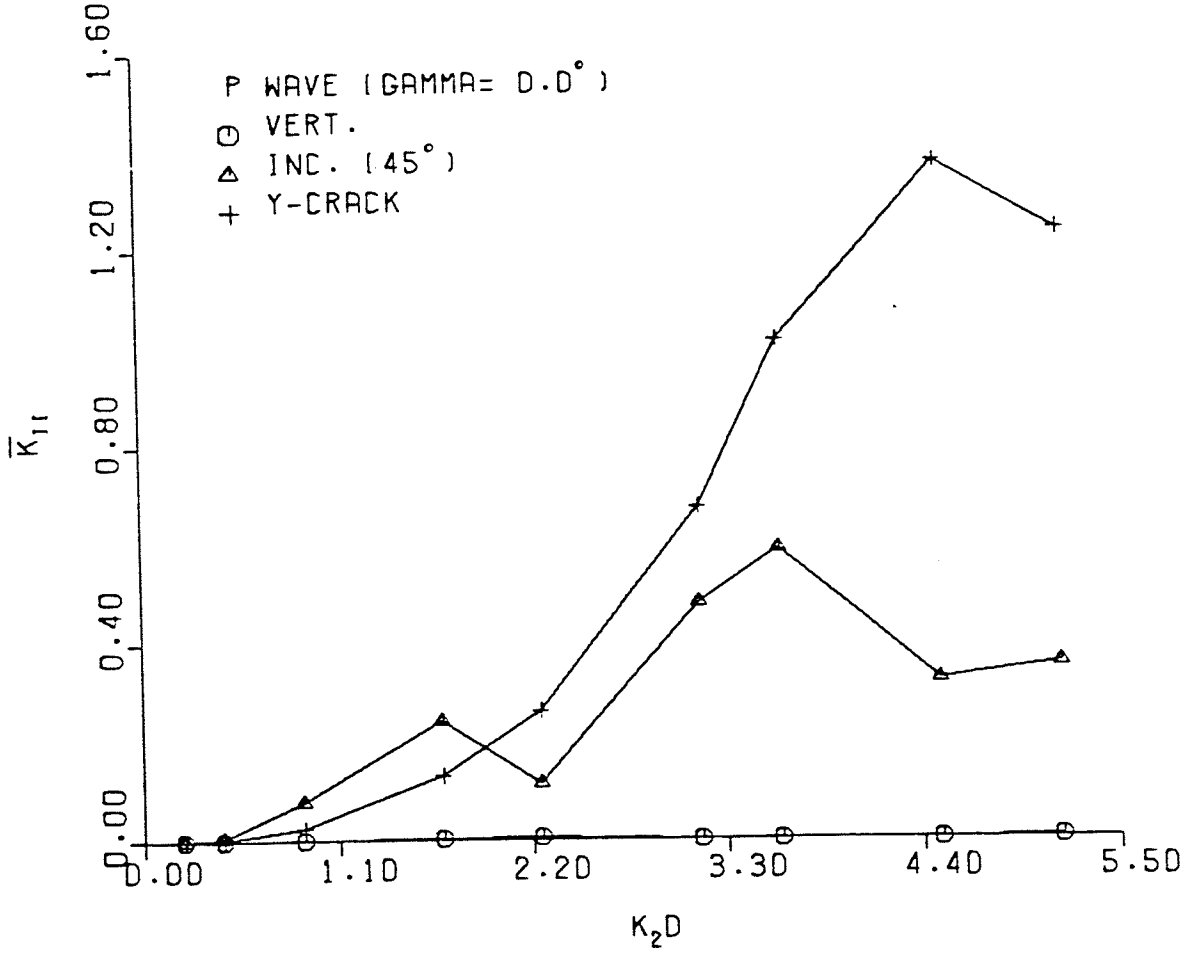

Fig. 5.9 - Mode I and Mode II stress intensity factors at crack tips of different cracks for an incident P wave

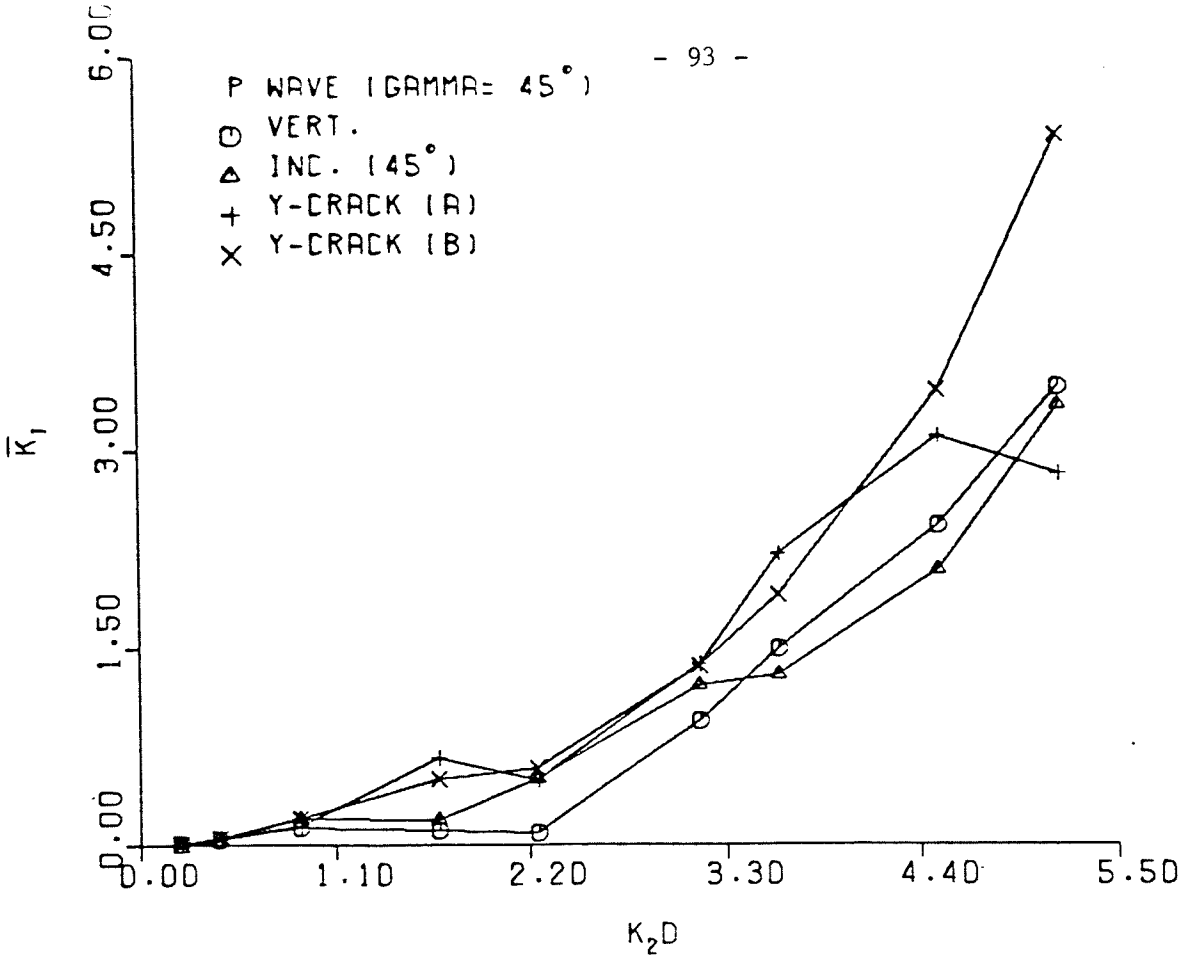

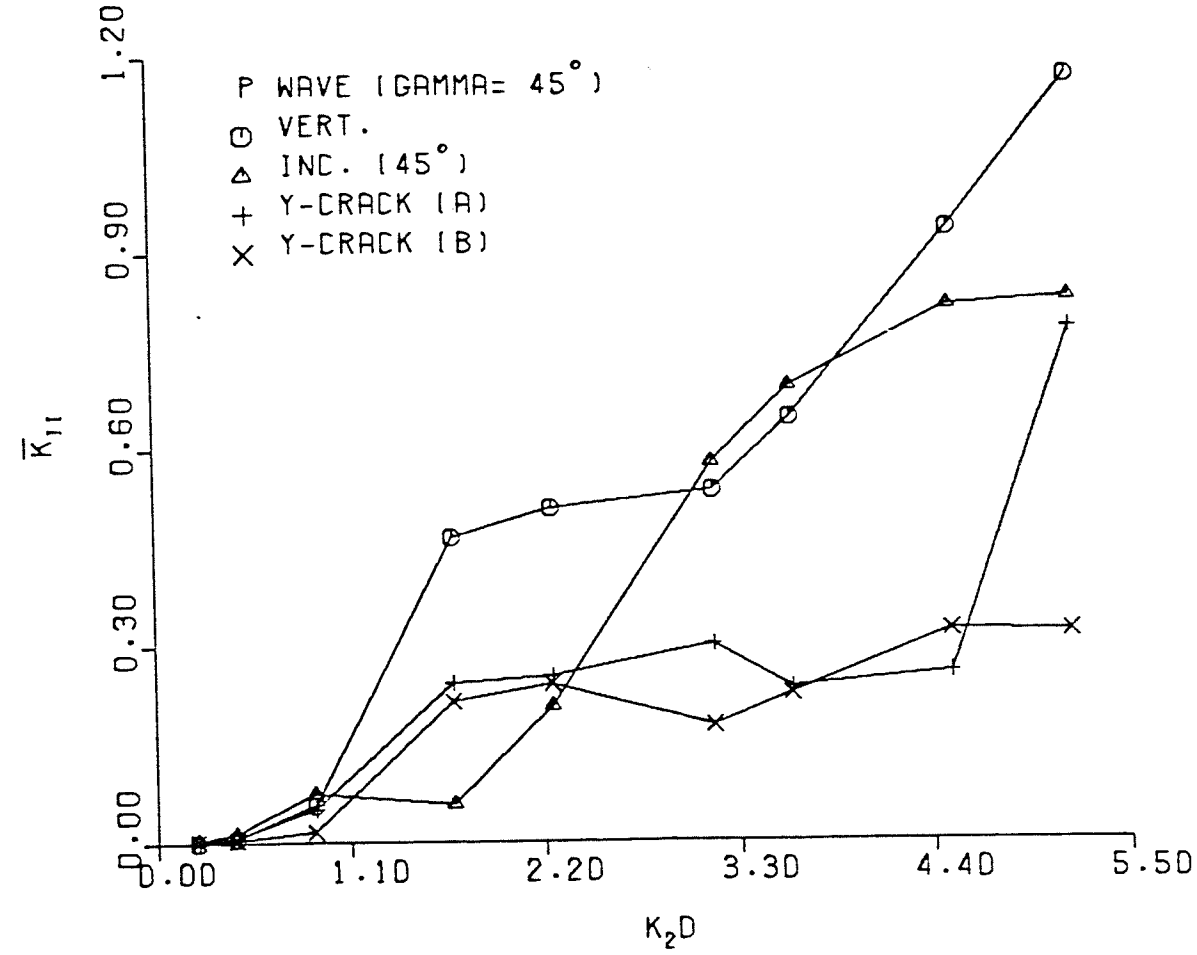

Fig. 5.10 - Mode I and Mode II stress intensity factors at crack tips of different cracks for an incident P wave

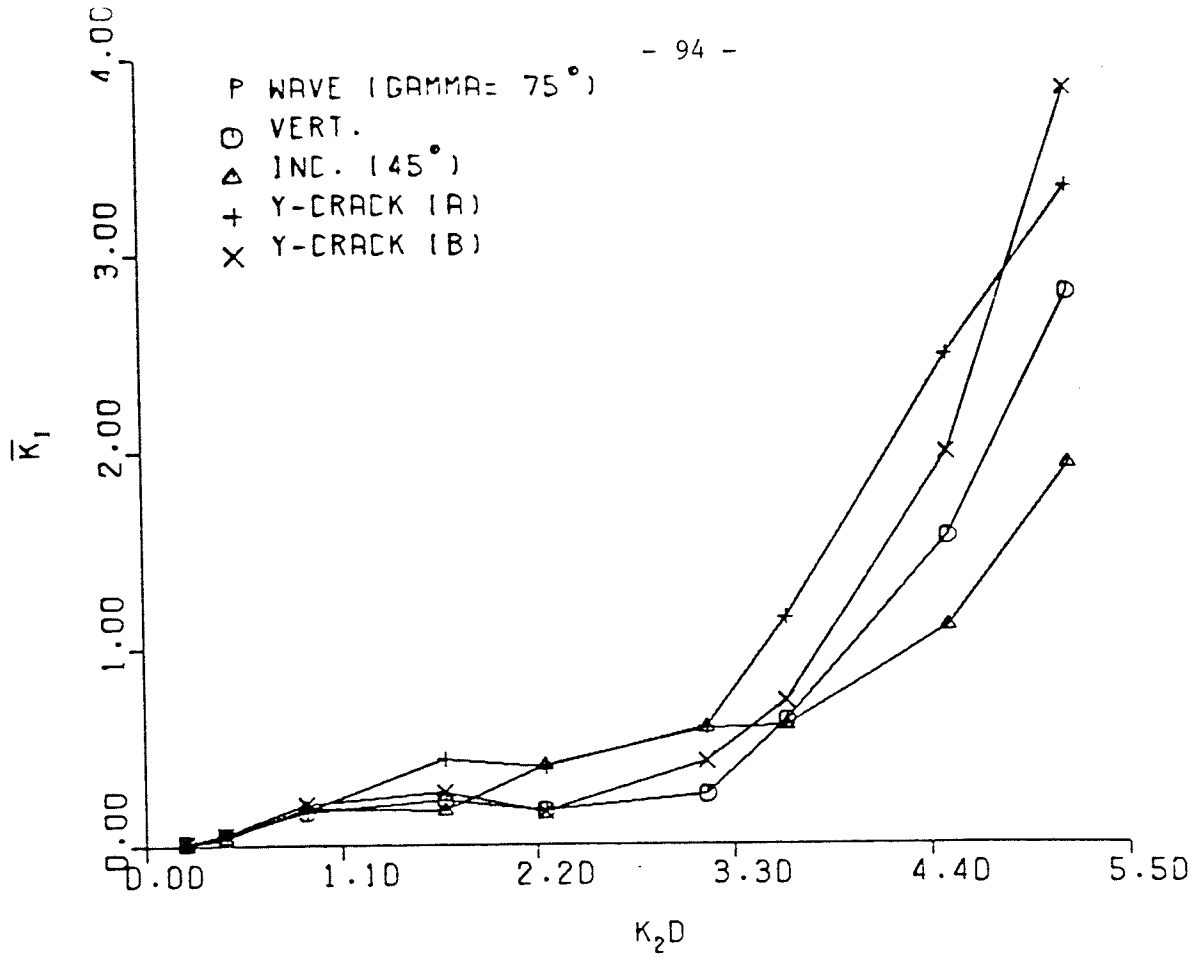

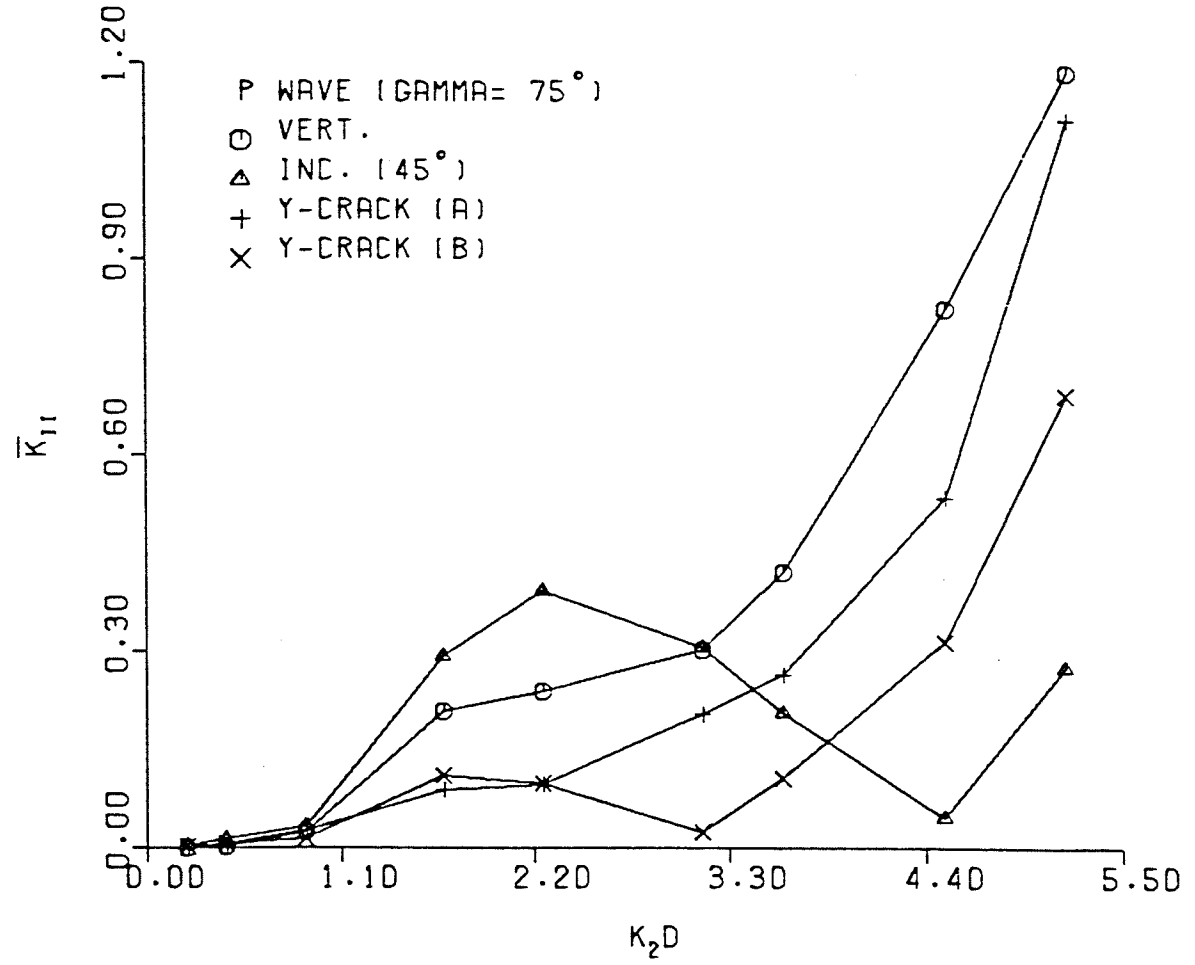

Fig. 5.11 - Mode I and Mode II stress intensity factors at crack tips of different cracks for an incident P wave

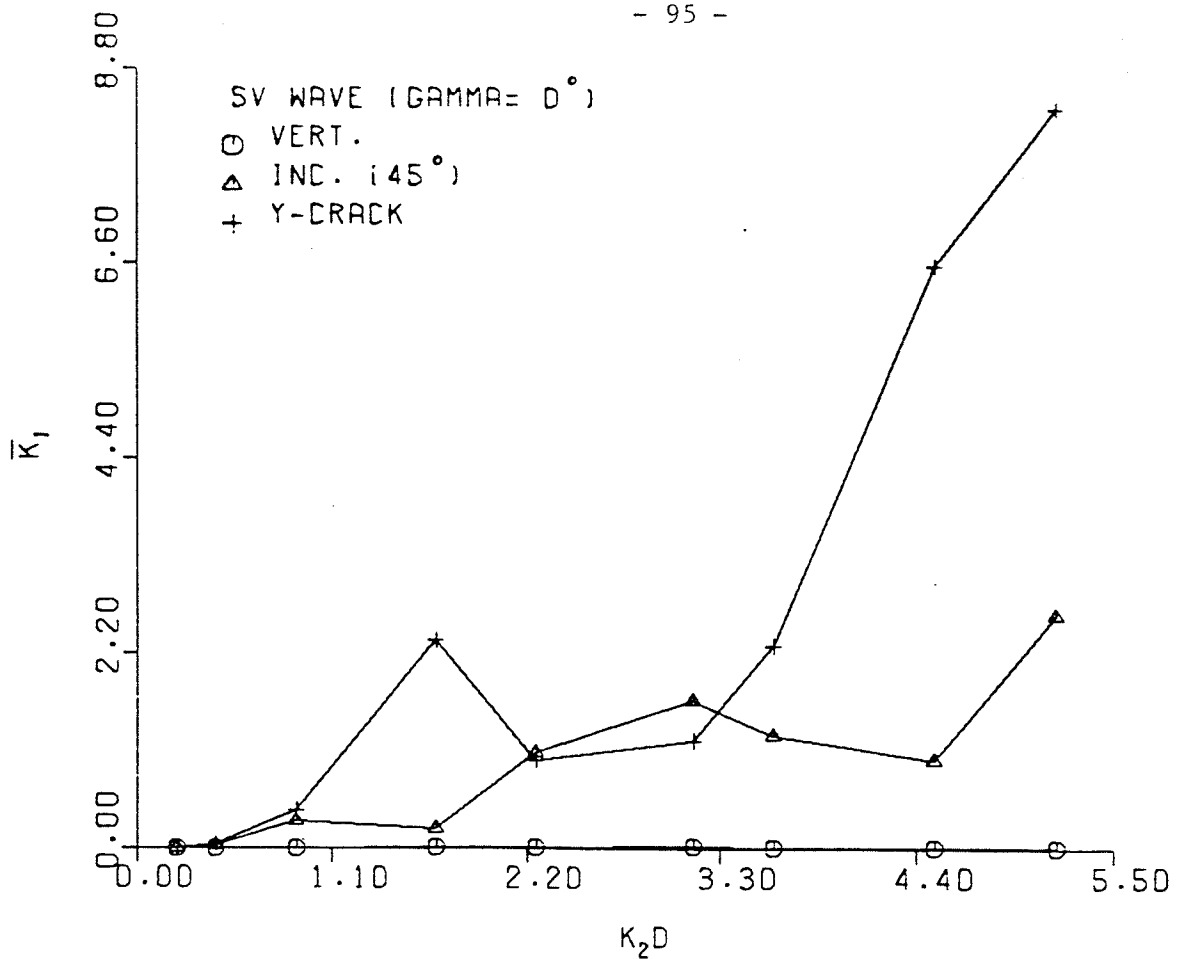

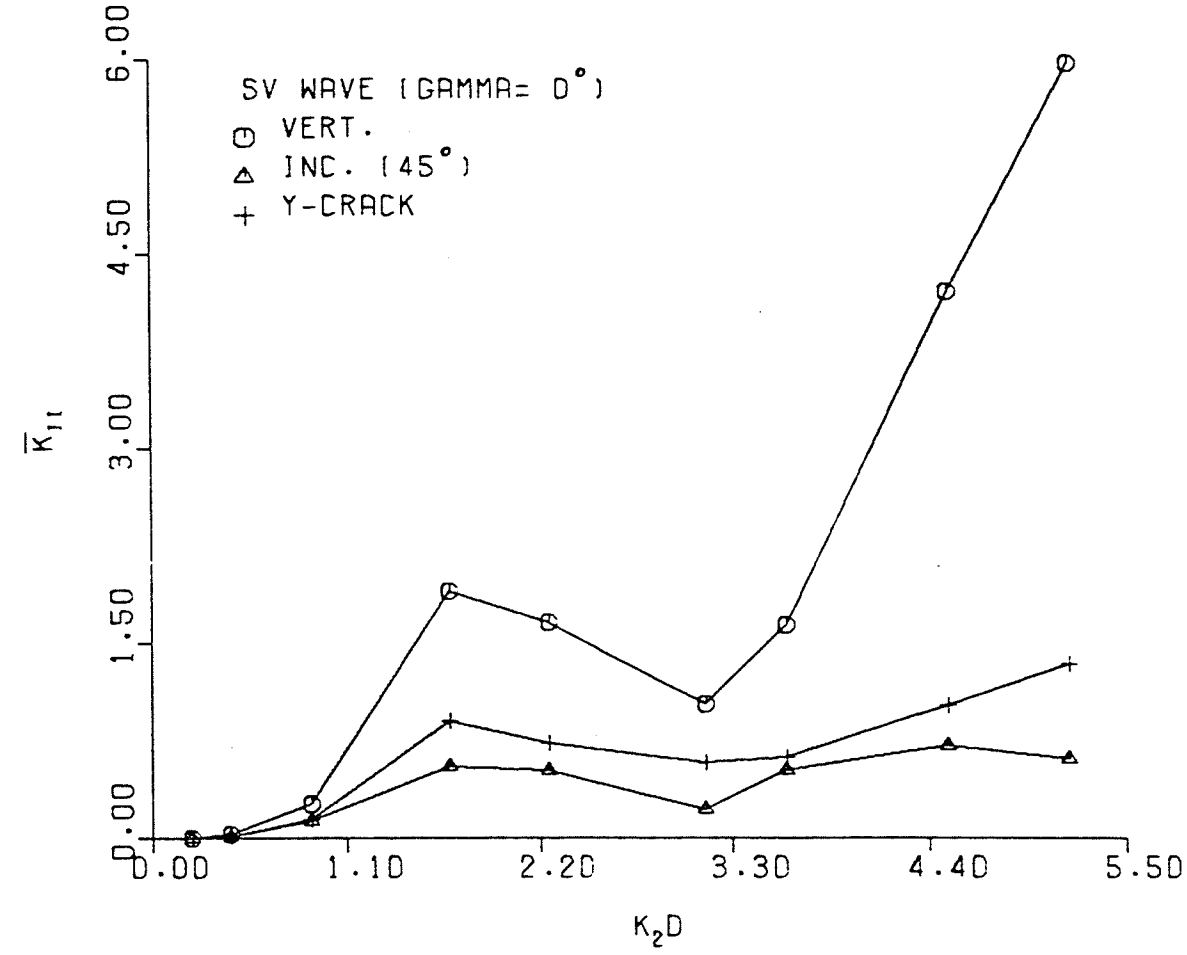

Fig. 5.12 - Mode I and Mode II stress intensity factors at crack tips of different cracks for an incident SV wave

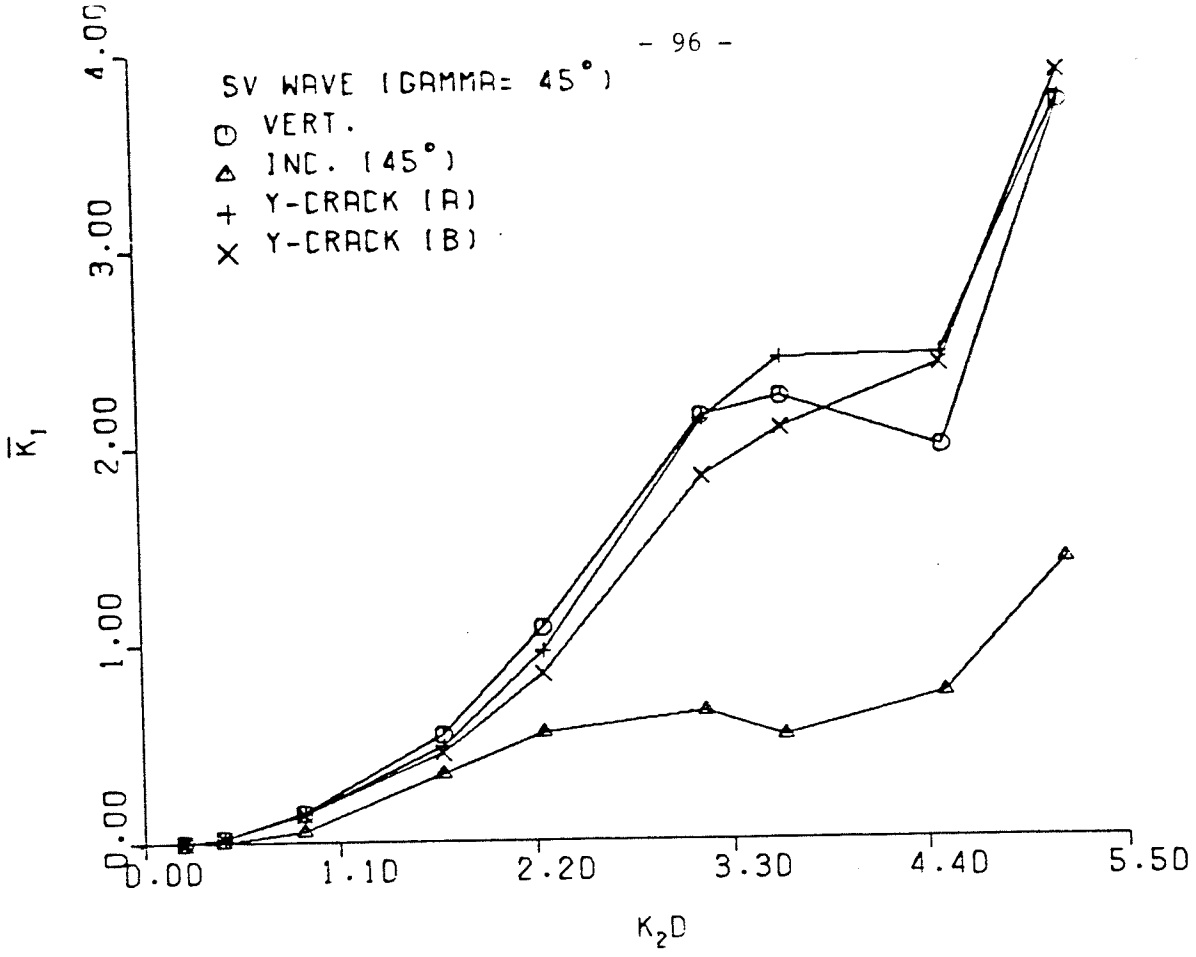

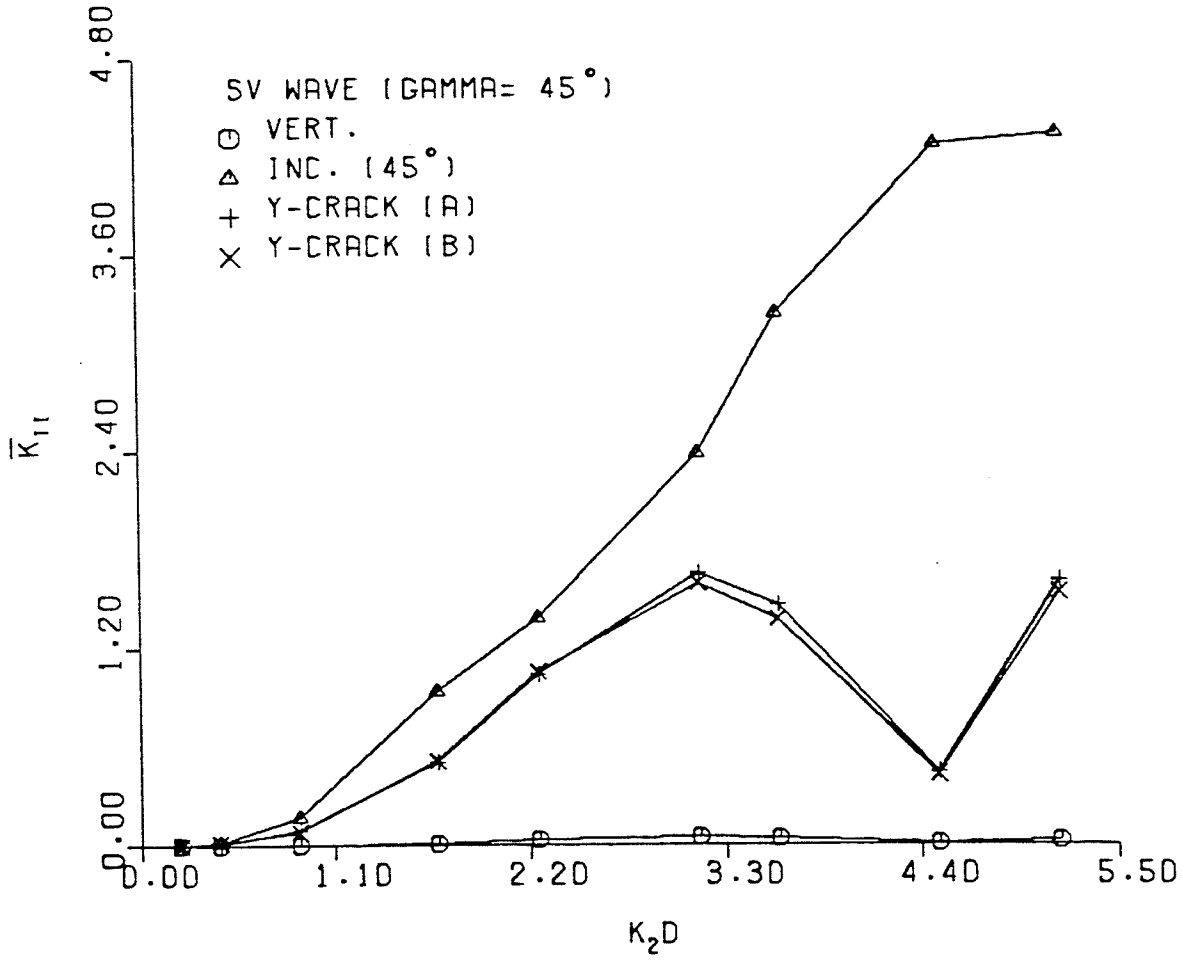

Fig. 5.13 - Mode I and Mode II stress intensity factors at crack tips of different cracks for an incident SV wave

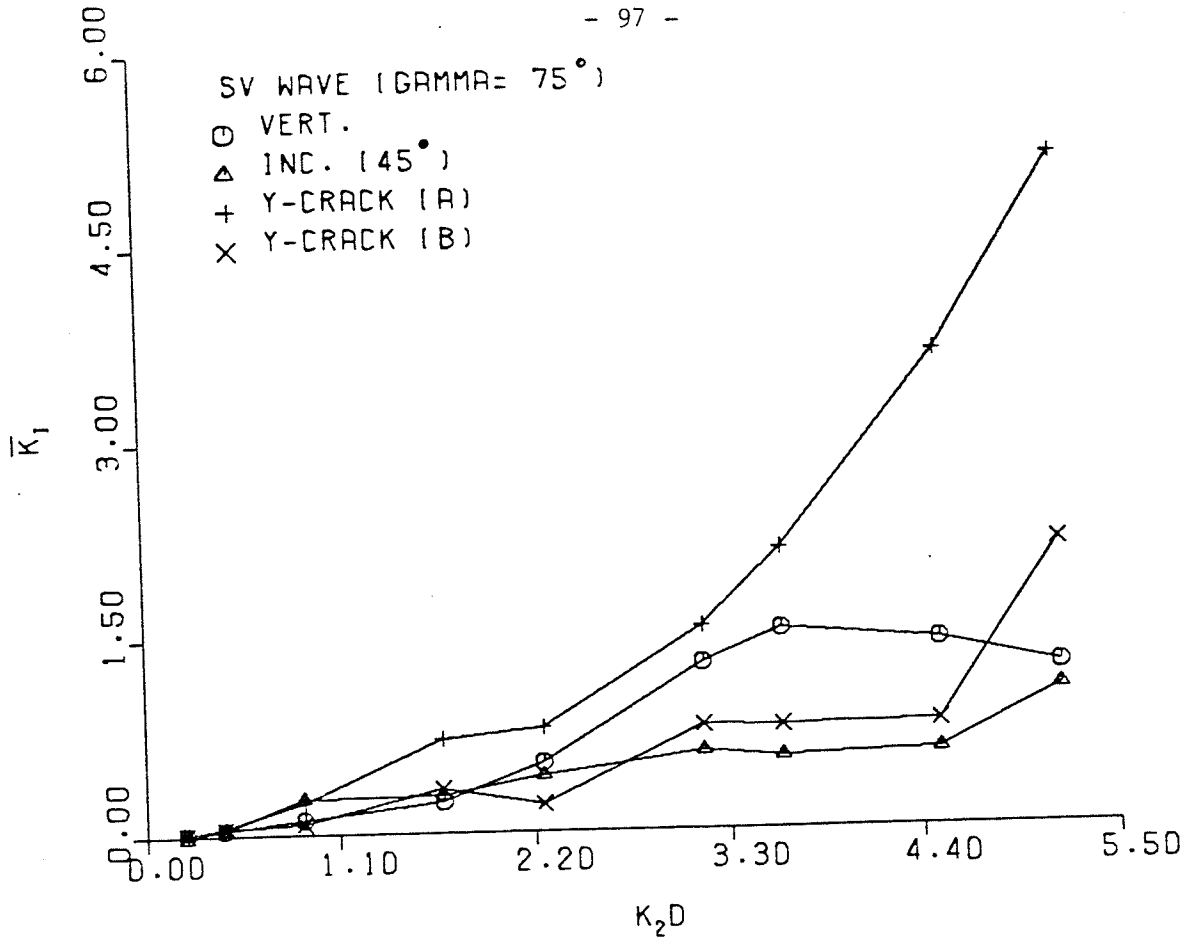

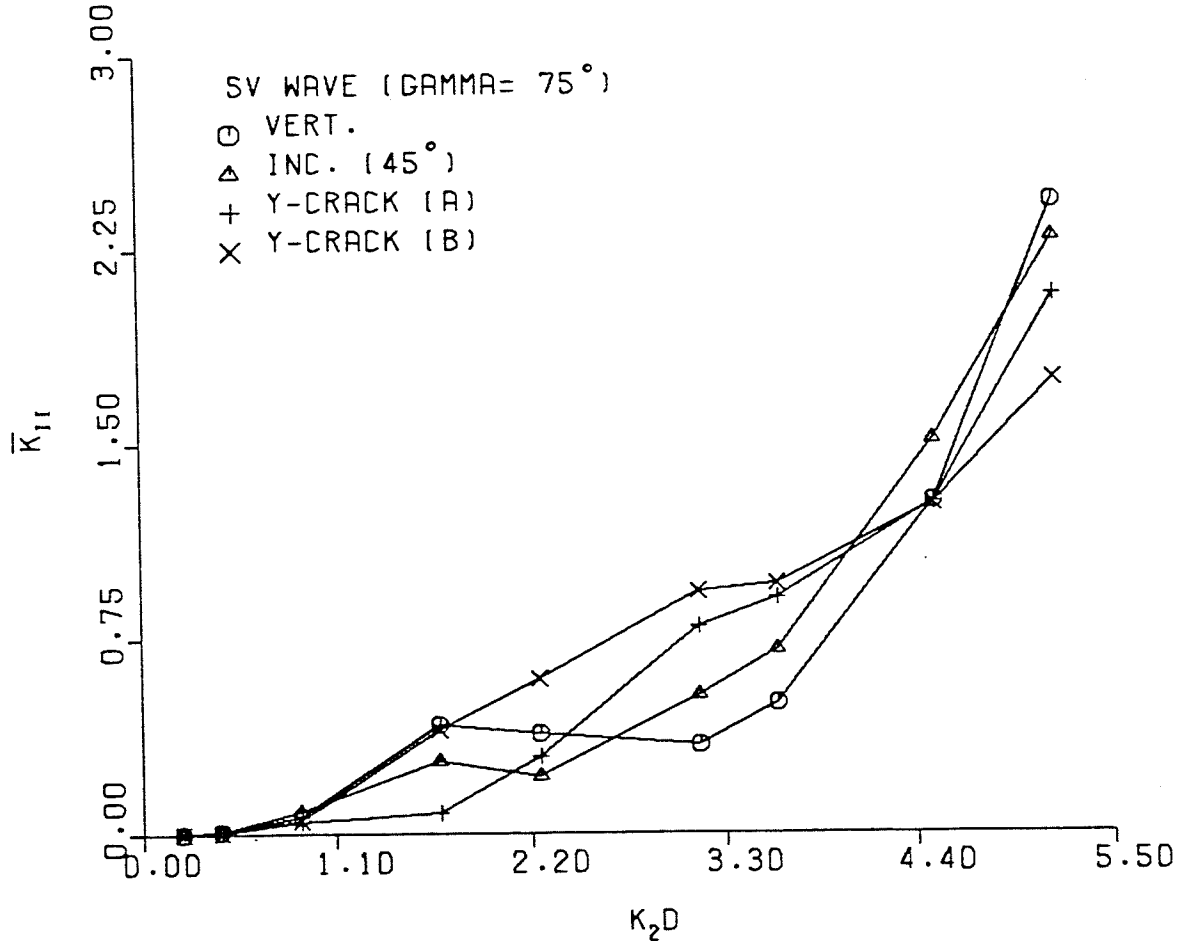

Fig. 5.14 - Mode I and Mode II stress intensity factors at crack tips of different cracks for an incident SV wave

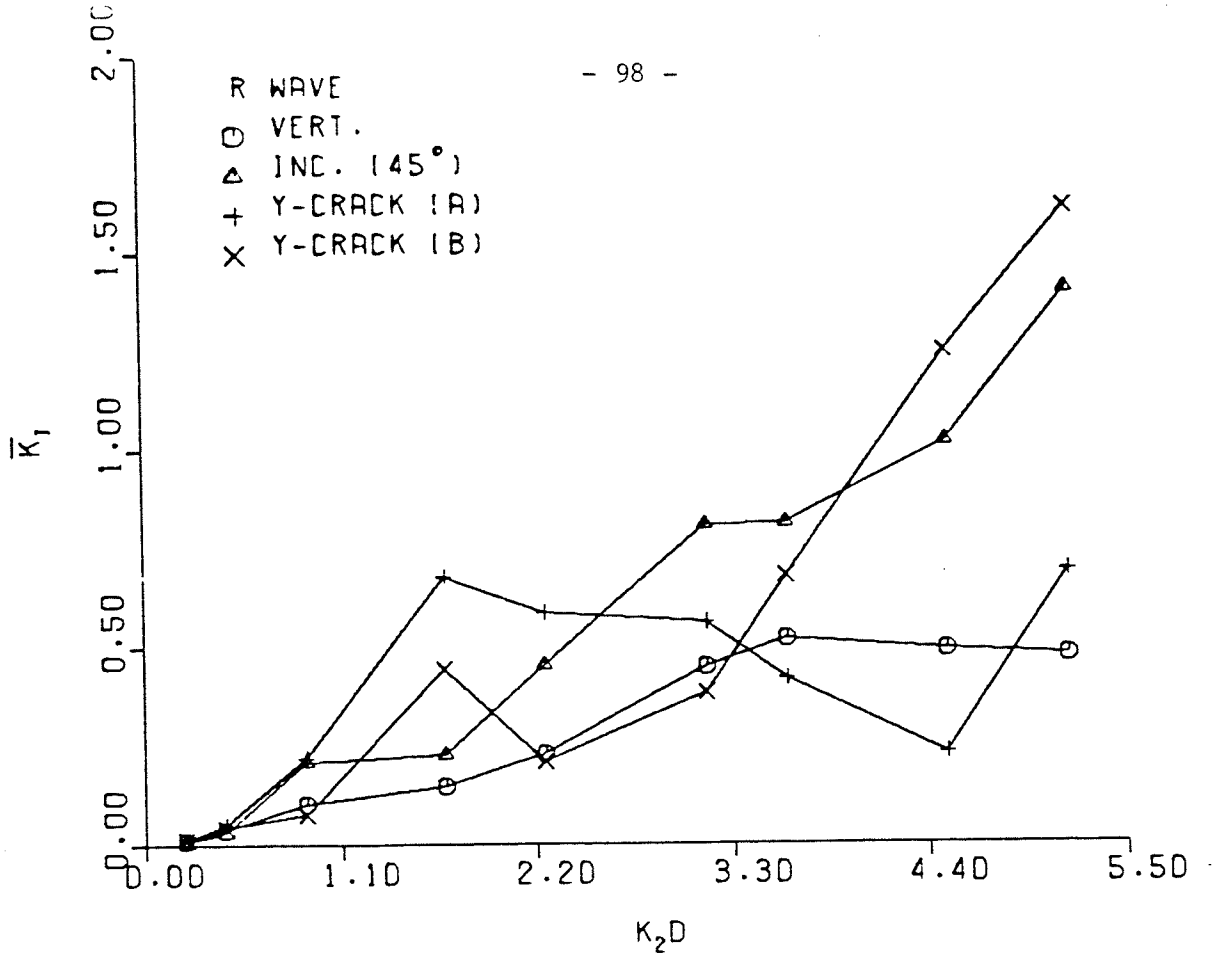

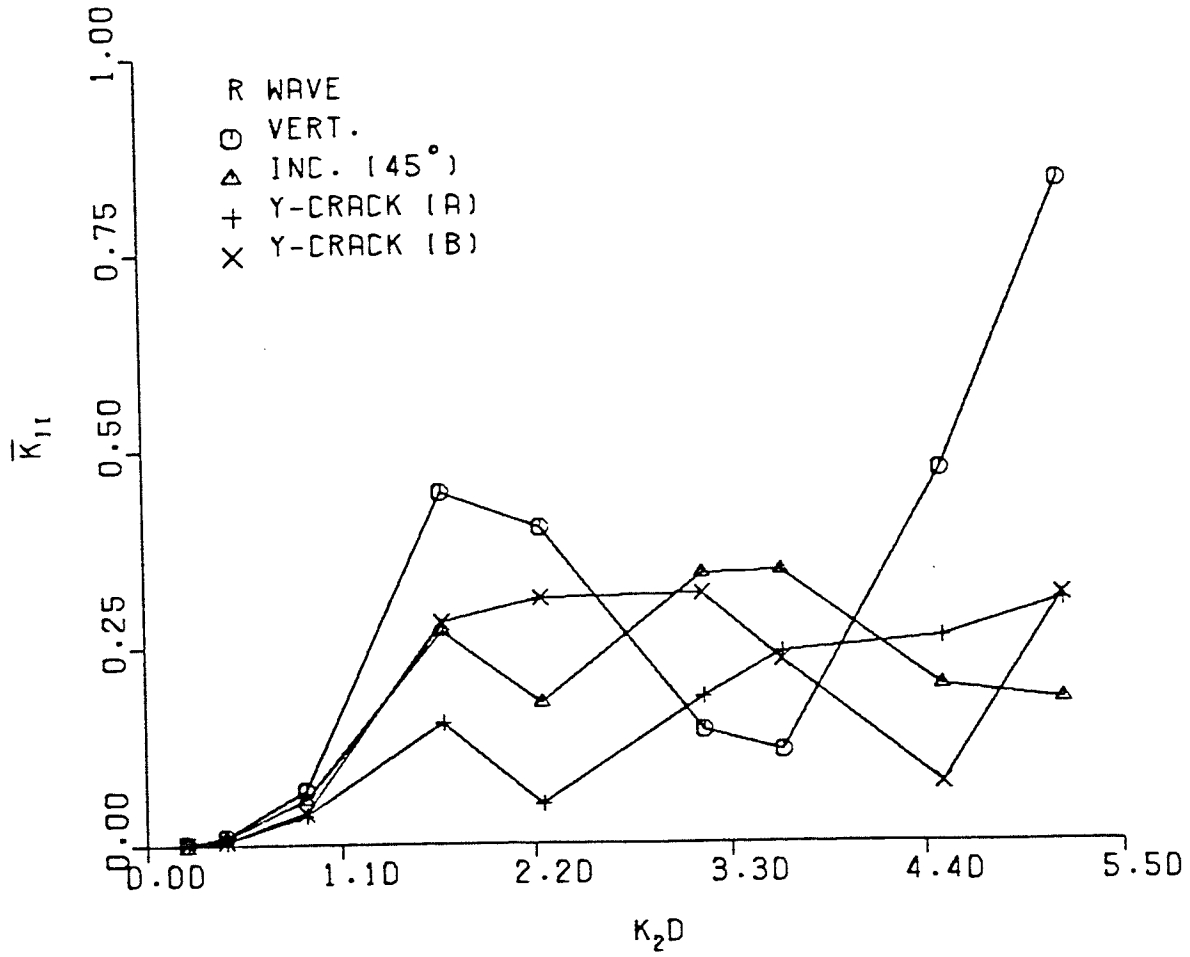

Fig. 5.15 - Mode I and Mode II stress intensity factors at crack tips of different cracks for an incident R wave

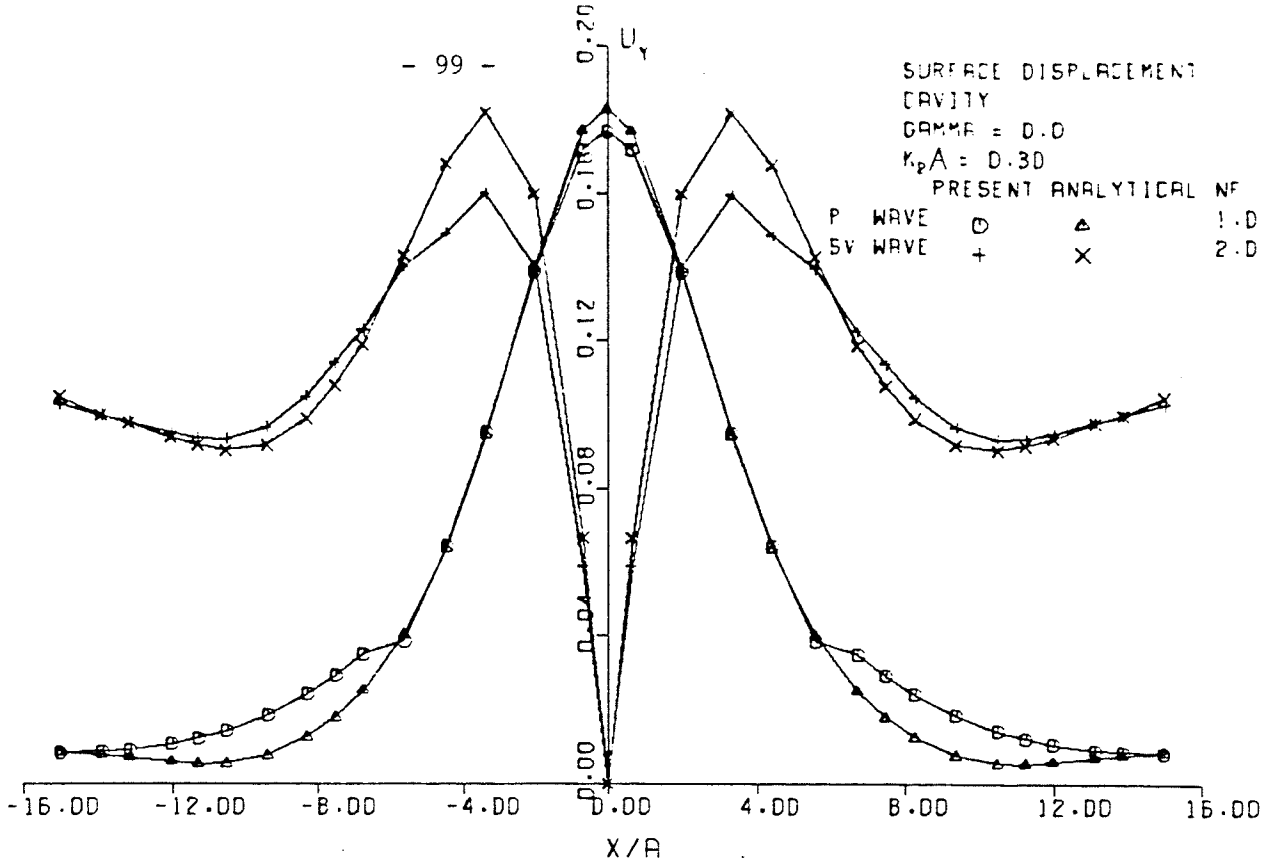

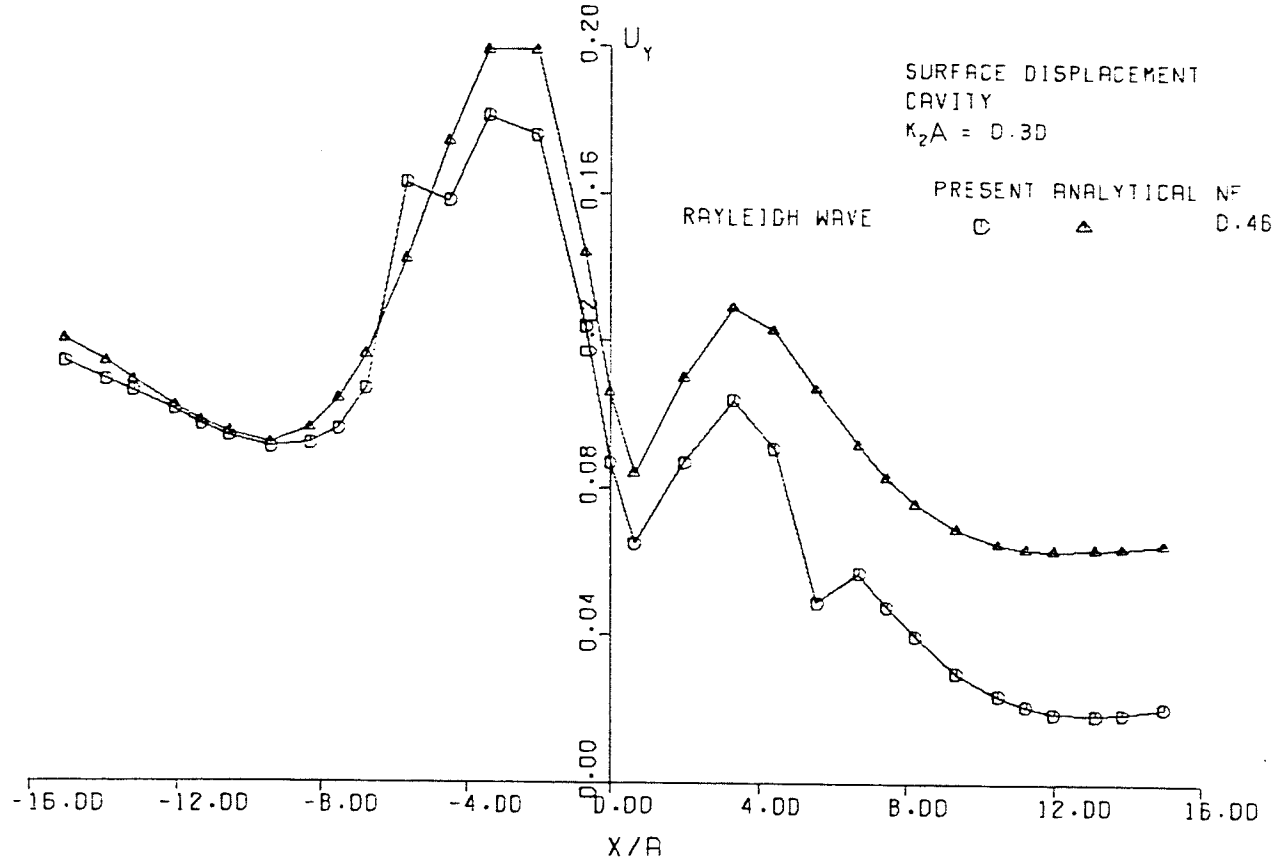

Fig. 5.16 - Comparision of Scattered Vertical Displacement With Those of Analytical Results.

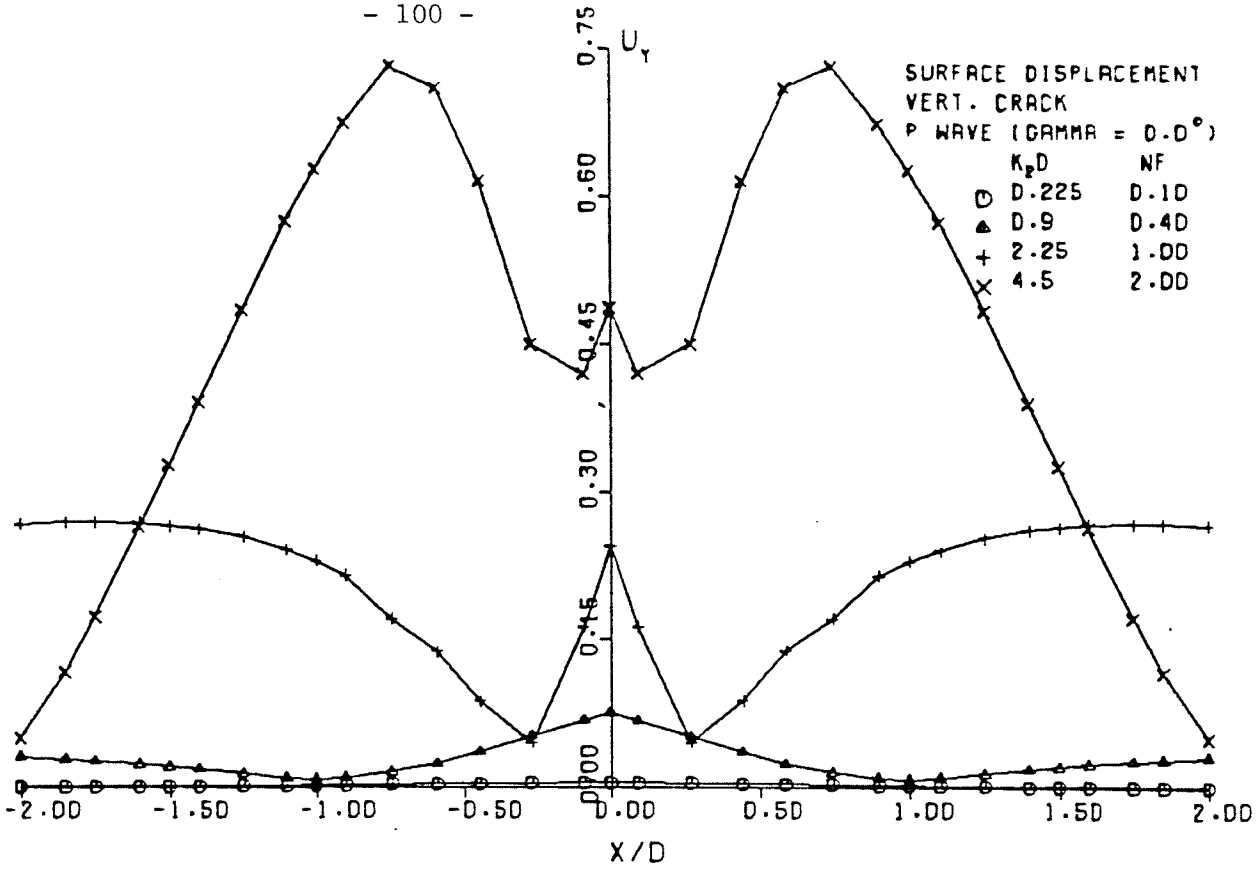

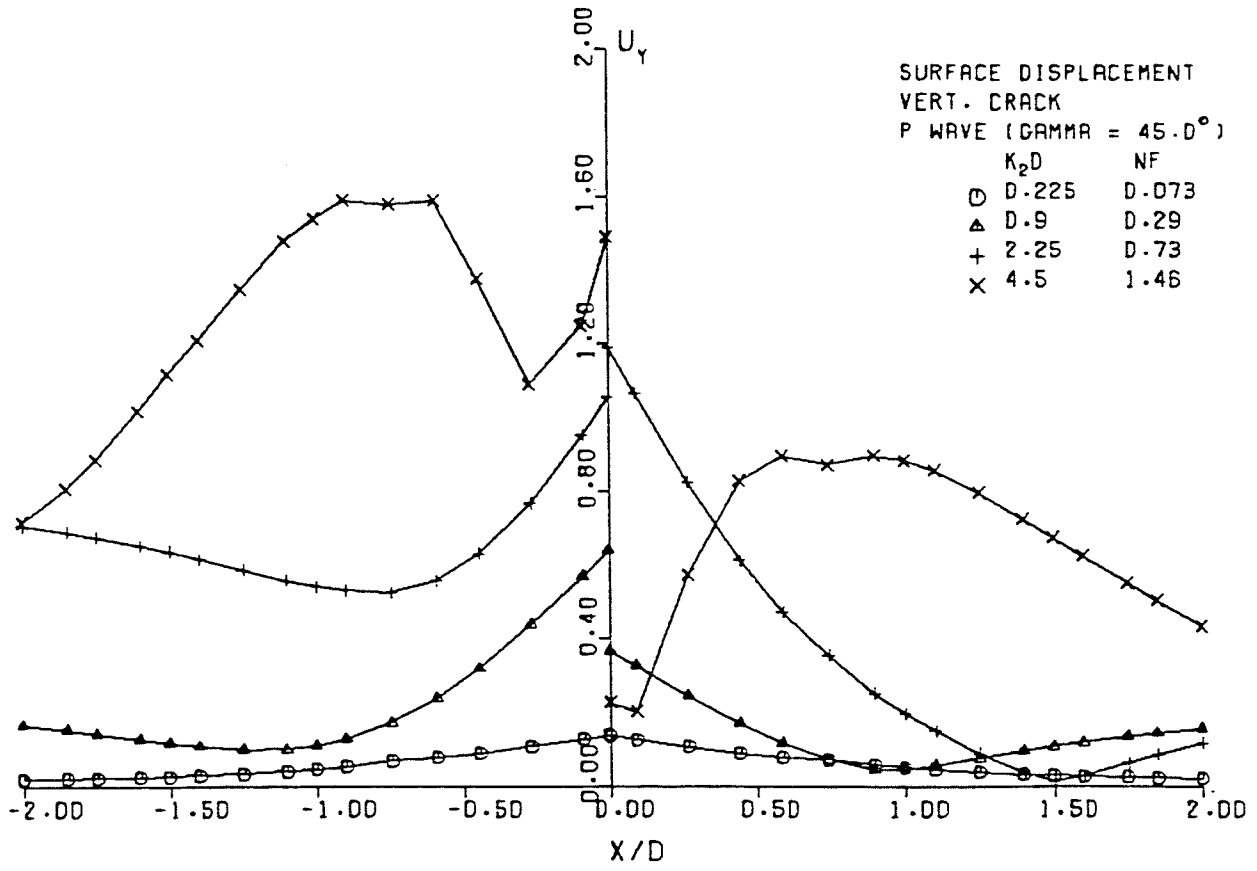

Fig. 5.17 - Scattered vertical surface displacement due to vertical crack for incident P waves.

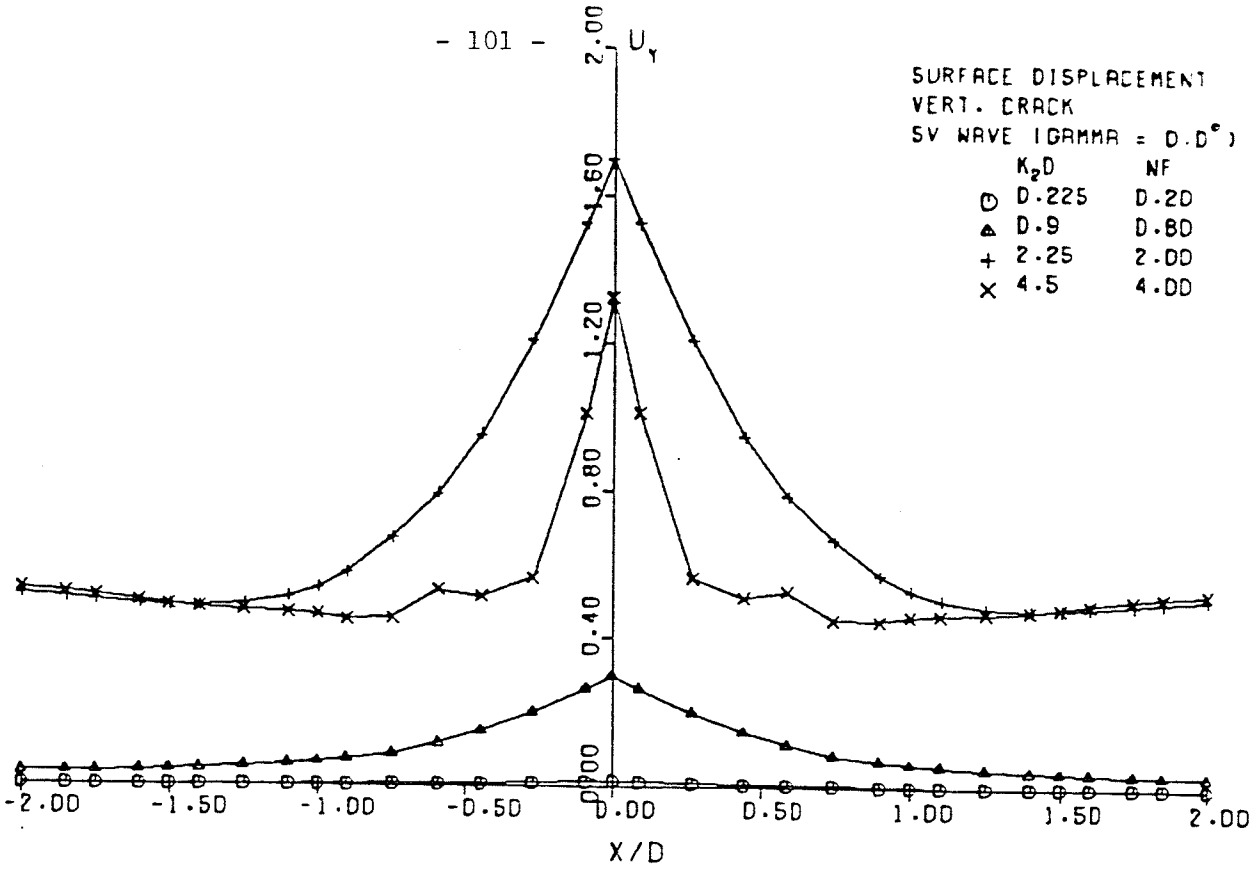

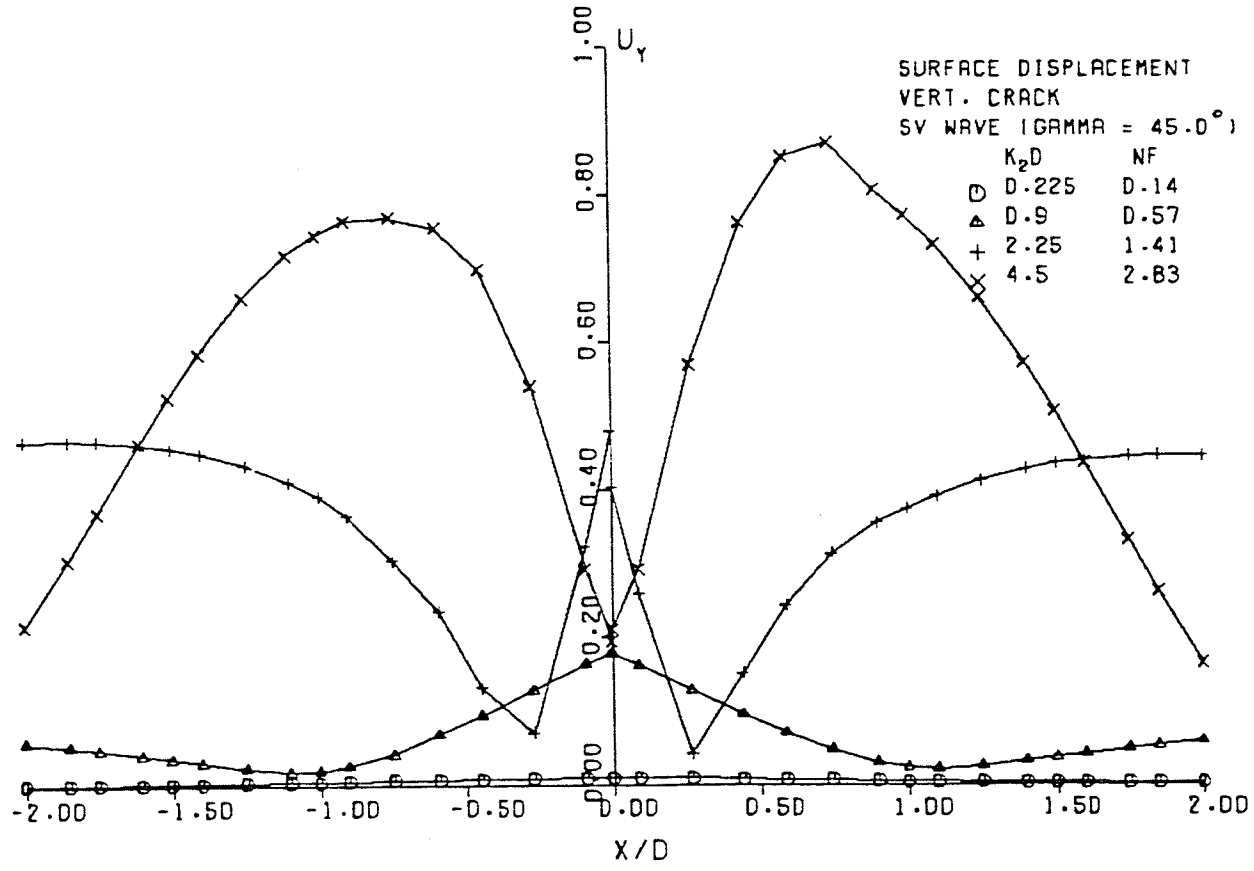

Fig. 5.18 - Scattered vertical surface displacement due to vertical crack for incident SV waves.

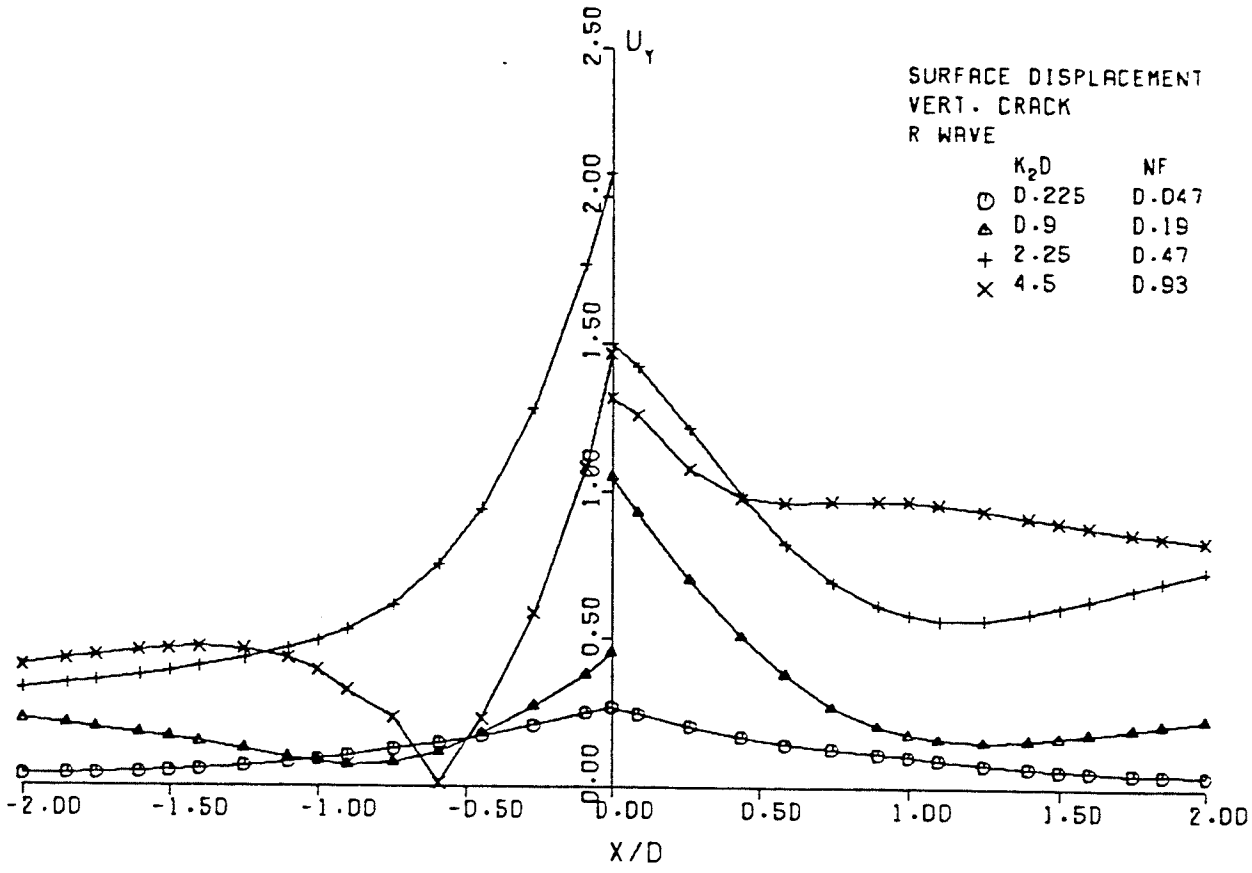

Fig. 5.19 - Scattered vertical surface displacement due to vertical crack for incident R wave.

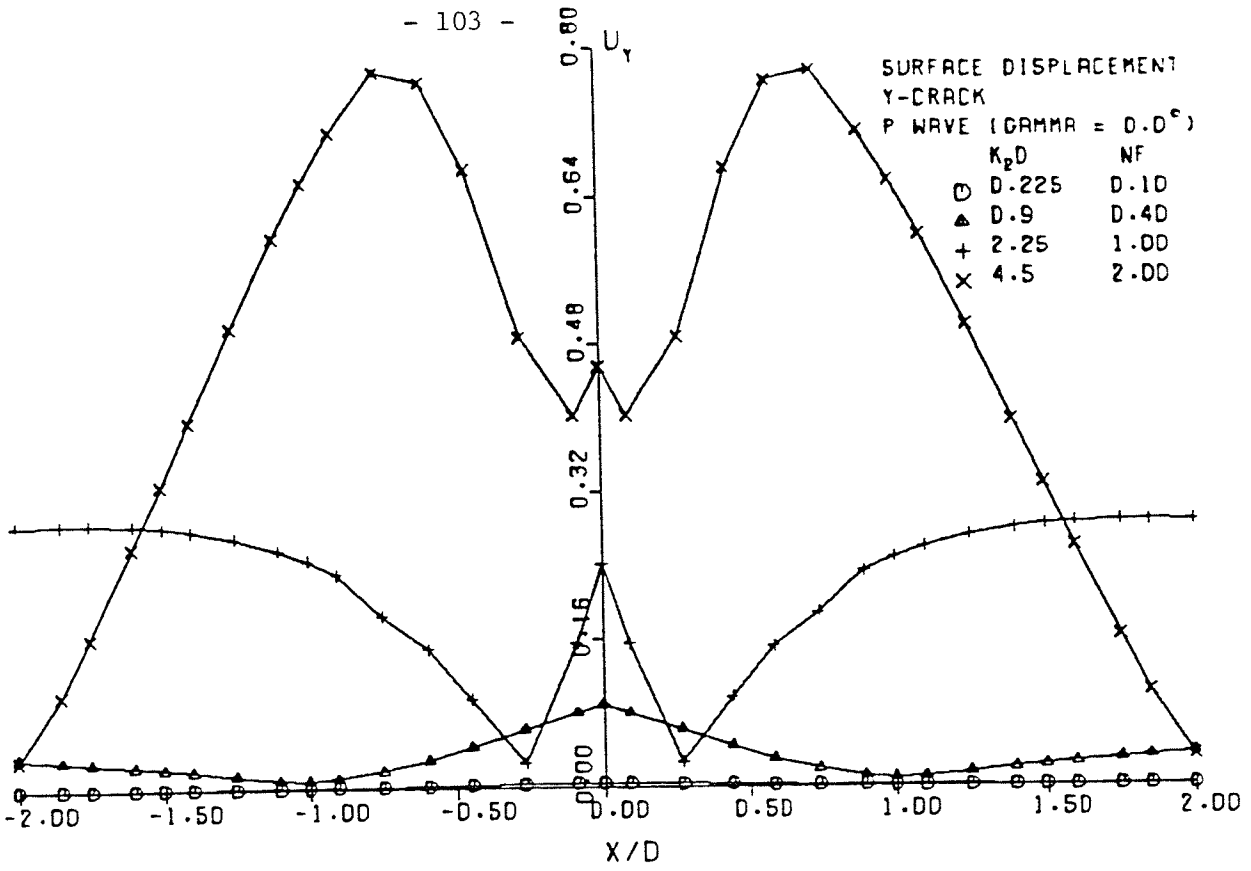

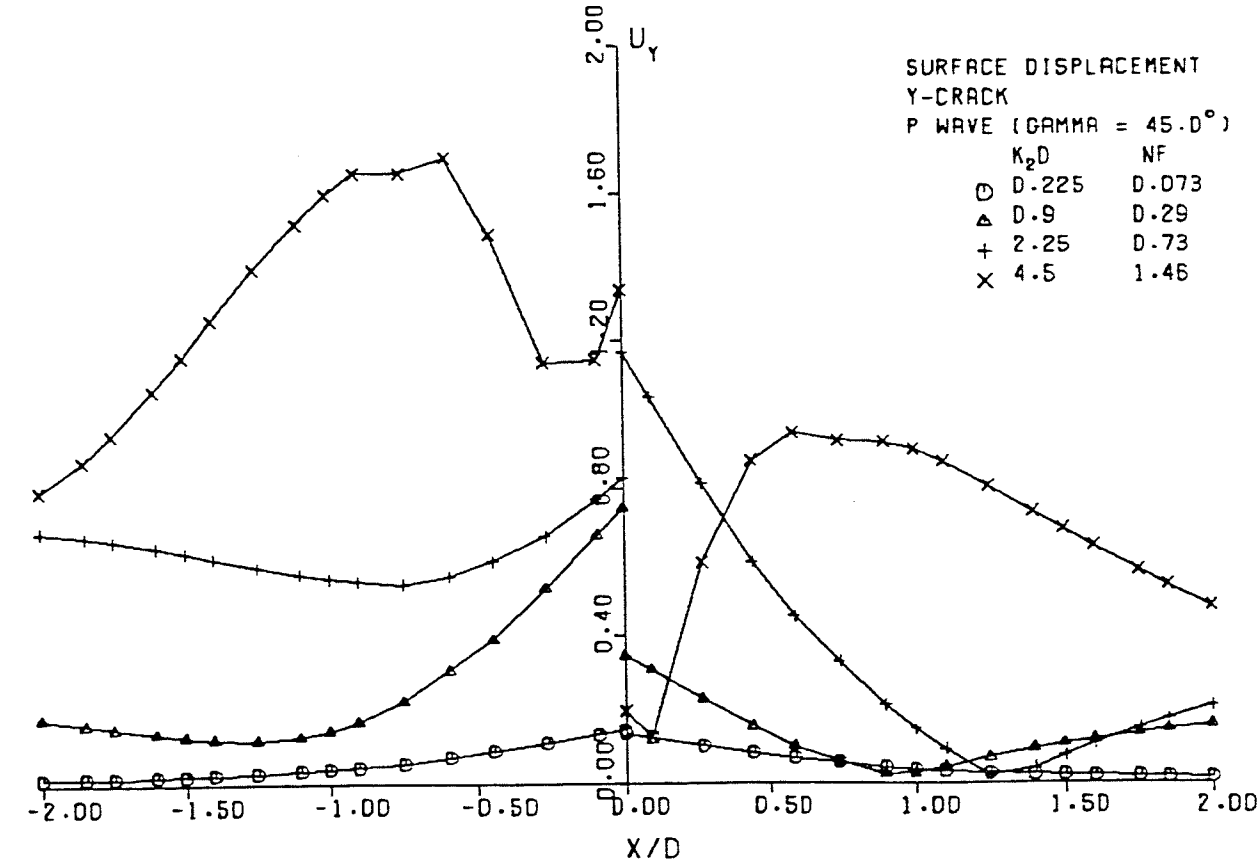

Fig. 5.20 - Scattered vertical surface displacement due to Y crack for incident P waves.

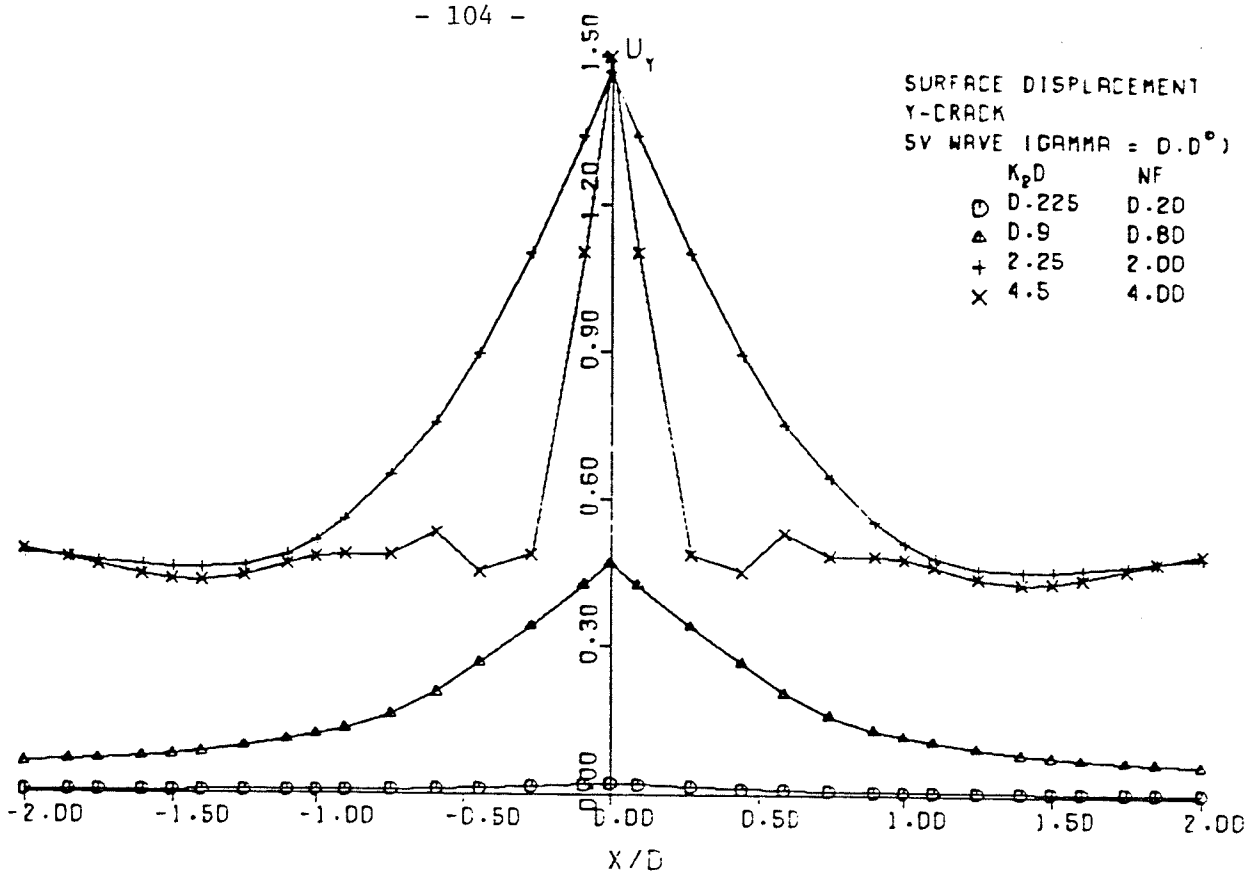

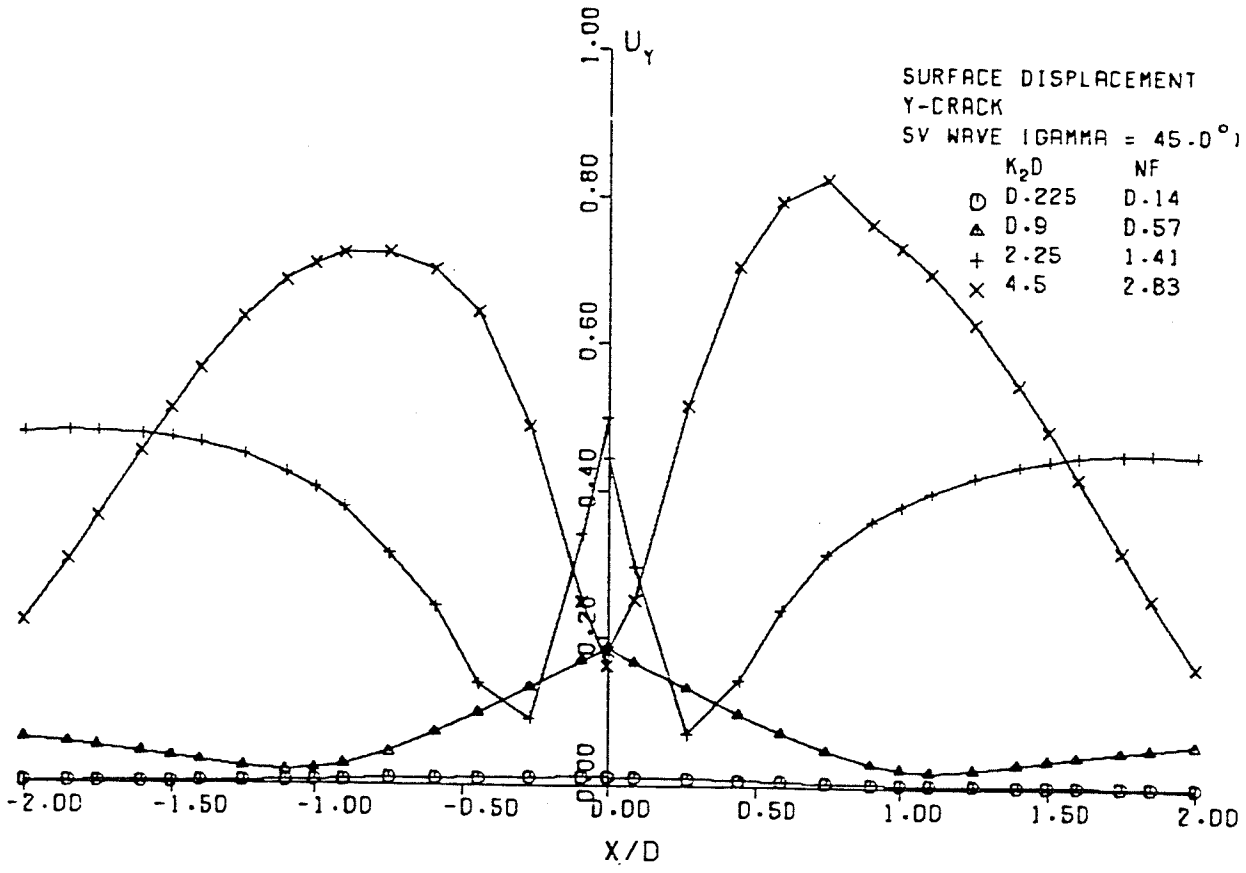

Fig. 5.21 - Scattered vertical surface displacement due to Y crack for incident SV waves.

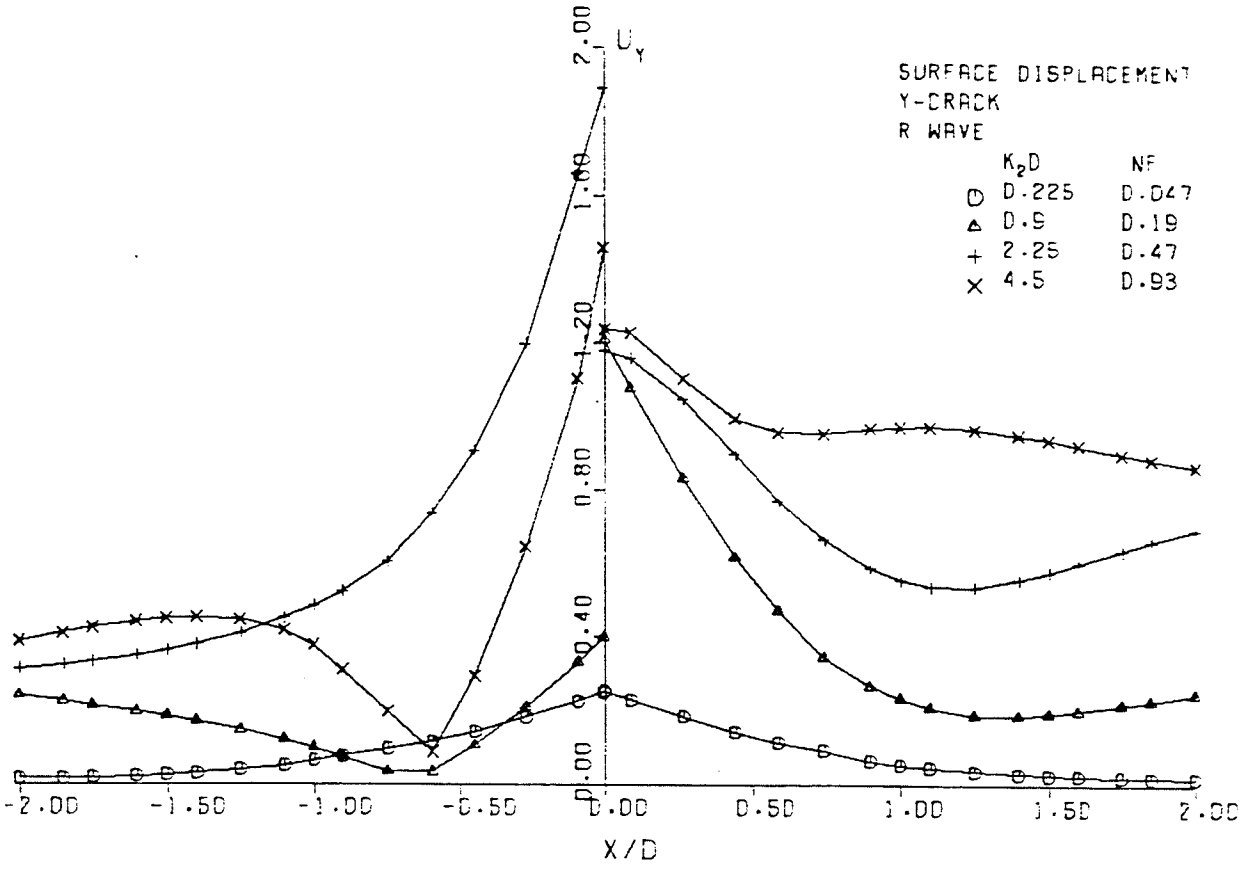

Fig. 5.22 - Scattered vertical surface displacement due to Y crack for incident R wave.

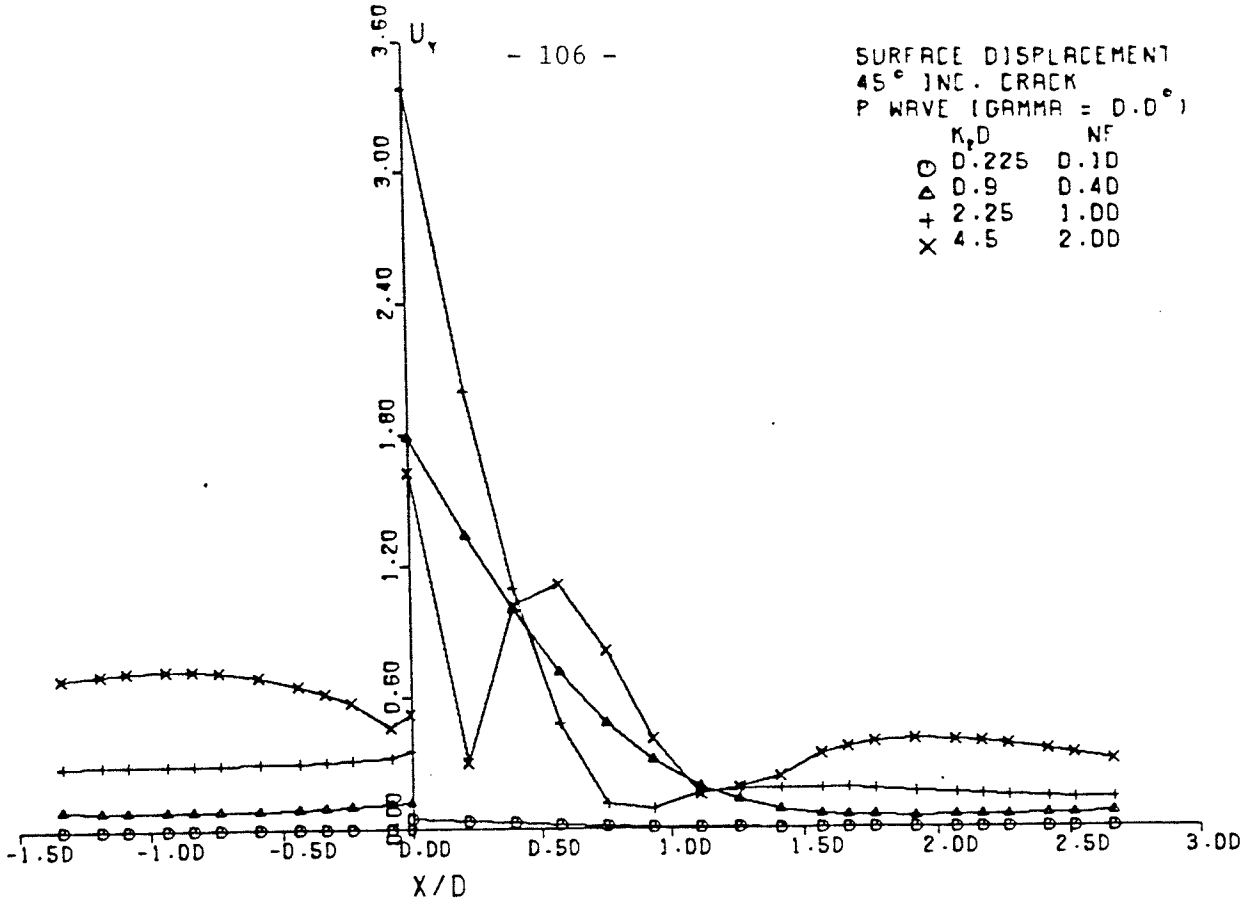

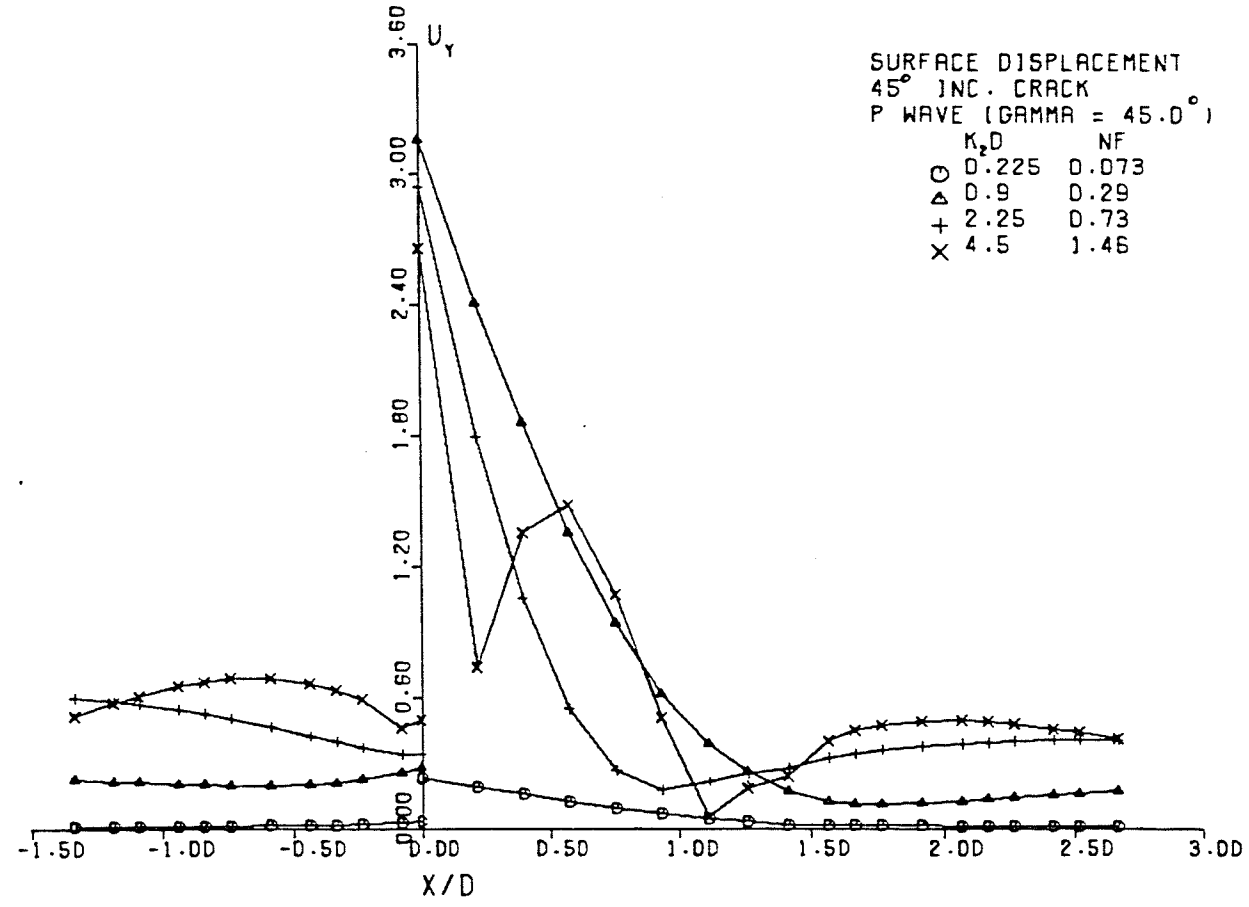

Fig. 5.23 - Scattered vertical surface displacement due to 45° inclined crack for incident P waves.

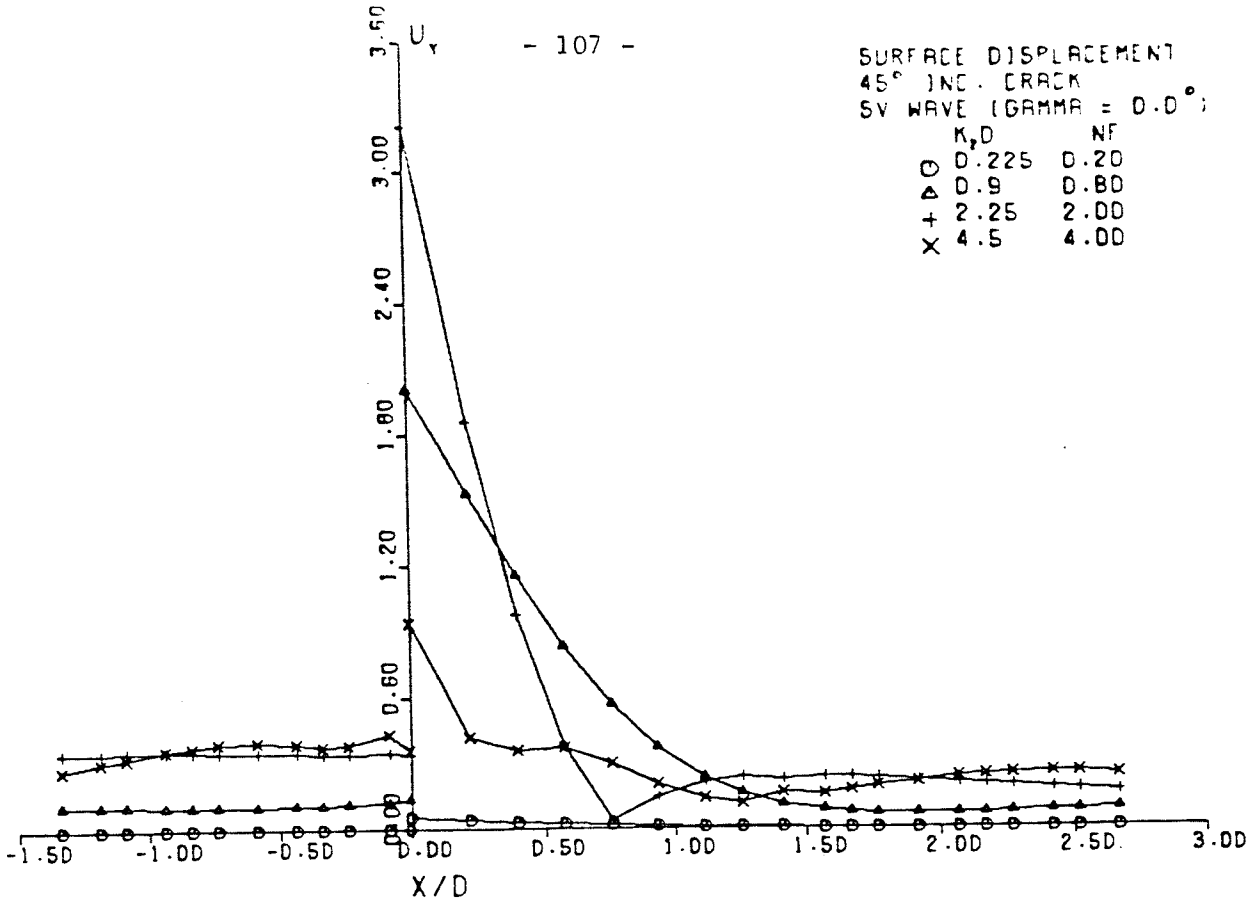

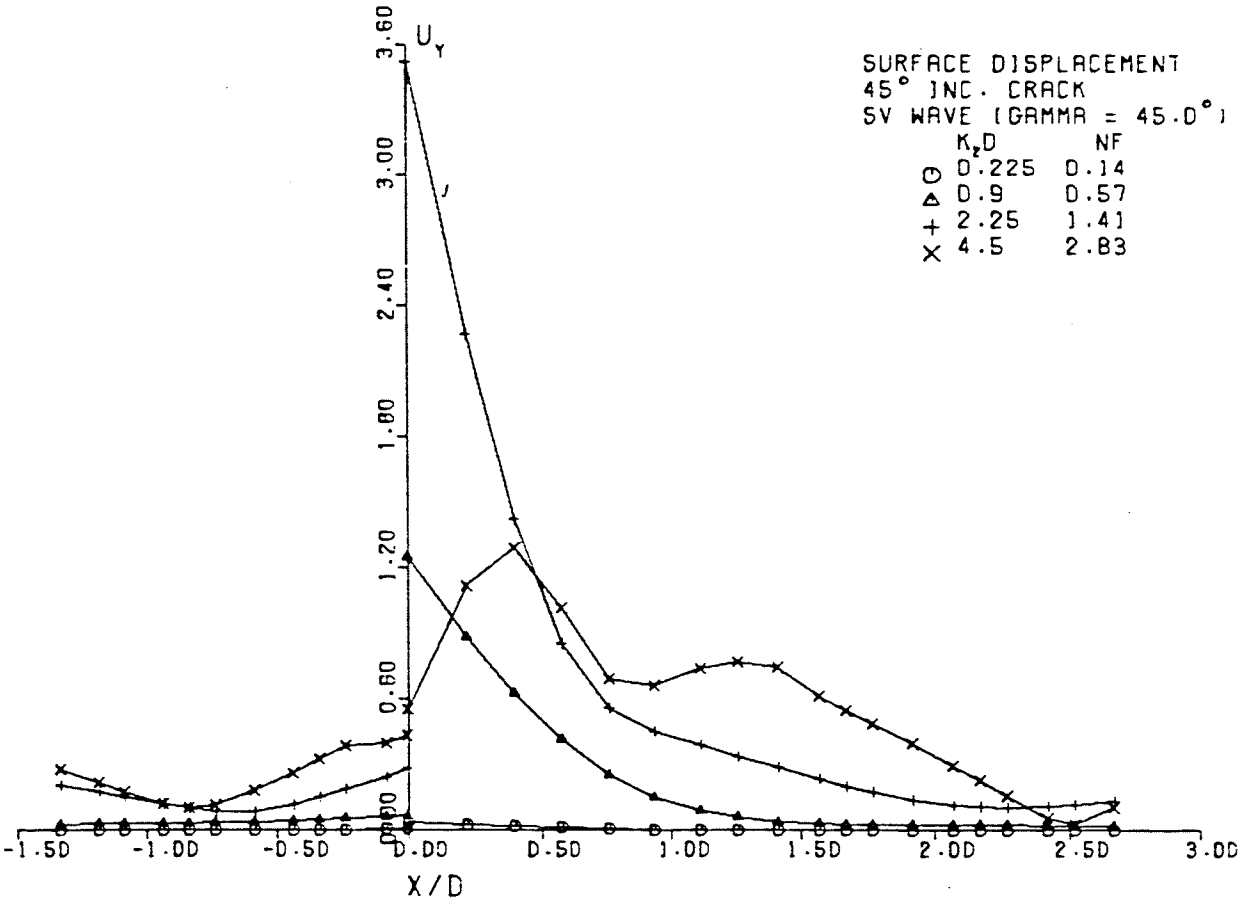

Fig. 5.24 - Scattered vertical surface displacement due to 45° inclined crack for incident SV waves.

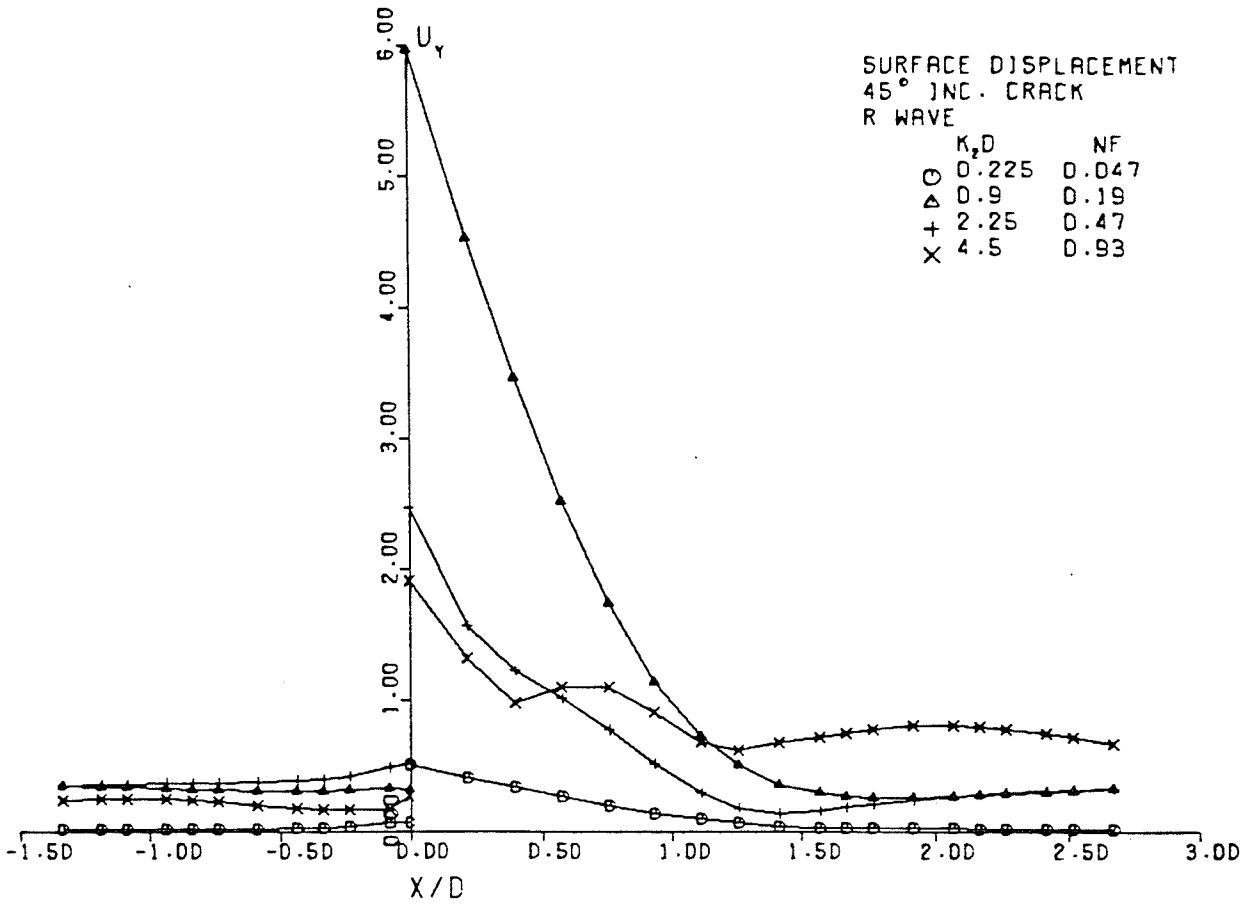

Fig. 5.25 - Scattered vertical surface displacement due to 45° inclined crack for incident R wave.